

POLITECNICO DI TORINO

Corso di laurea in Ingegneria Aerospaziale

Tesi di Laurea Magistrale

**Microscale Analysis of Fiber Reinforced
Composite Materials**



Relatori

Prof. Erasmo Carrera

Prof. Marco Petrolo

Candidato

Aurelio De Simone

Supervisore esterno

University of Massachusetts Lowell

Prof. Marianna Maiarù

Marzo 2018

*Alla mia famiglia e a Cecilia
per l'indispensabile sostegno...*

Contents

1	Composite materials: introduction and application	1
1.1	Composite materials constituents	2
1.2	Different matrices' natures	4
1.2.1	Polymer matrices	4
1.2.2	Metal matrices	6
1.2.3	Ceramic matrices	6
1.3	Reinforcement phase	7
1.3.1	Fiber reinforcement	7
1.3.2	Principal types of fibers	8
1.4	Composites for aerospace applications	10
1.5	The repeating unit cell	13
1.5.1	Periodic boundary conditions	14
1.5.2	RUCs realizations	15
2	Theoretical background: Finite Elements Method and Unified For-	
	mulation	17
2.1	Introduction to the Unified Formulation	18
2.2	FEM and Theory of structures approximations	19
2.3	Derivation of the Fundamental Nucleus	20
2.4	Assembly technique	21

2.5	Weak Form of the Solid Model	22
2.6	The Taylor expansion class	24
2.6.1	Unified formulation of expansion	25
2.6.2	Higher-order Taylor expansion class	25
2.7	The Lagrange expansion class	26
2.7.1	Normalized coordinates and Lagrange polynomials	27
2.7.2	Displacement field with a Lagrange elements	29
2.7.3	Locally refined cross-sections	30
3	CUF application: assessment of referred structures	33
3.1	Static analysis of a cantilever beam	34
3.1.1	Analysis via Taylor-like expansion	35
3.1.2	Analysis via Lagrange polynomials	40
3.2	Static analysis of a hollow square cross-section	42
3.2.1	One punctual load	43
3.2.2	Two punctual loads	43
3.3	Static analysis of a C-shaped cross-section beam	44
3.3.1	Flexural-torsional load	45
3.4	Static analysis of a open hollow square cross-section beam	47
3.5	Static analysis with solid-like geometrical BCs	48
3.5.1	Compact rectangular beam	48
3.5.2	Compact rectangular curved beam	49
3.5.3	C-shaped cross-section beam	51
3.6	Static analysis of a symmetric laminated beam	52
3.7	Static analysis of a eight-layer composite beam	54
3.8	Single and double cell static analysis	56

3.9	Static Analysis of a cross-ply beam with different models	59
3.10	Modal analysis of a cantilever beam	60
3.10.1	Cantilevered compact section	61
3.10.2	Cantilevered thin-walled structure	63
3.11	Micromechanical analysis	64
3.11.1	Fiber reinforced composites	64
3.11.2	Void filled composite	65
4	Statistical analysis of the RUCs: description of fibers' arrangement and degree of randomness	68
4.1	Nearest neighbor distribution	69
4.2	Second-order intensity function	71
4.3	Radial distribution function	74
4.4	Analysis of the repeating unit cells	76
4.4.1	Five-fibers RUCs	76
4.4.2	Ten-fibers RUCs	85
4.4.3	Thirty-fibers RUCs	93
5	Failure Analysis of the RUCs: conclusions	101
5.1	Failure Analysis	101
5.2	Results on five fibers RUCs	102
A	Record of the Statistical Analysis on the repeating unit cells	106
	Bibliography	121

Chapter 1

Composite materials: introduction and application

Most of the modern technologies requires the use of high performance materials, able to offer, with declining weight, a set of properties that cannot be found together in traditional materials. The possibility to combine different properties, characterizing different materials, in a single strong element was realized to meet the needs of companies and researchers and it is in a continuous improvement.

With the term composite materials are usually indicated materials obtained through the union of at least two constituents: every material corresponds to a phase and for this reason the composite is defined by a inhomogeneous structure. Usually the constituents constituting the composite material are divided by a clear interface with null thickness and each one of them is provided of different chemical and physical properties at the macroscopic and structural level capable to make them insoluble and separated from the others. What was said allow us to distinguish composite materials from metal alloys because, being a combination of different materials in shape and composition, every constituent keeps its own identity in the final compound without fusing completely in the other one. Examples of this typology of material are found in nature. In particular, it is possible to characterize as composites

- *wood*, made by cellulose fibers in a resinous matrix (lignin)

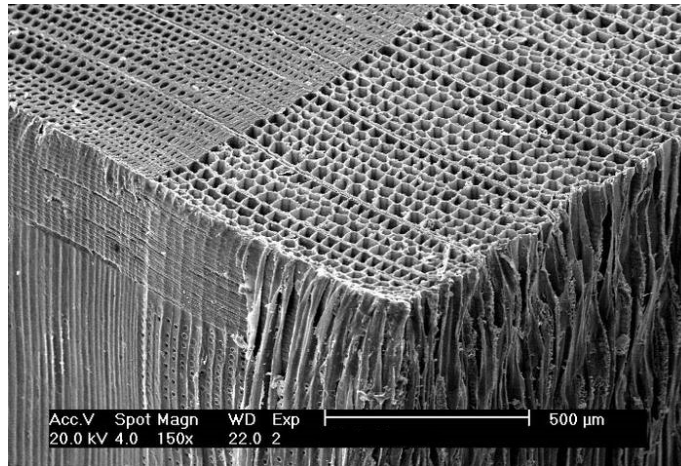


Figure 1.1: Abies alba

- *bone*, made by calcium crystals immersed in a cartilage matrix

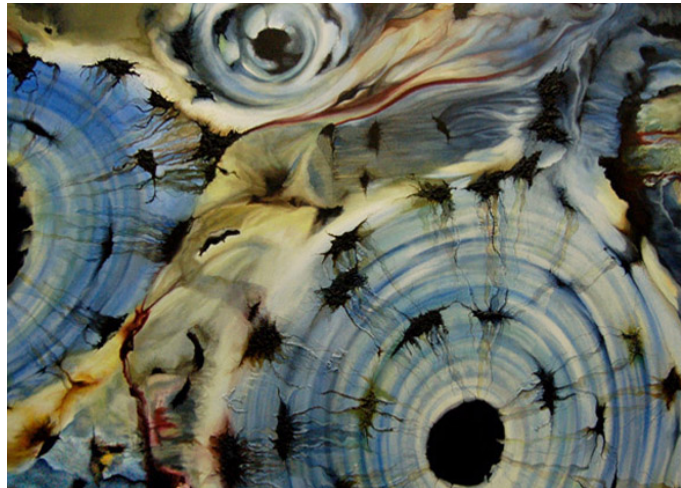


Figure 1.2: Bone tissue

1.1 Composite materials constituents

Every single material which make the final composite is, as we said before, a *constituent* and, on the basis of its role, can be called *matrix* or *reinforcement*. The matrix is a continuous homogeneous phase which has the task of keeping together the reinforcement, the second constituent, by ensuring that the particles or fibers have the right dispersion in the material and by transferring the stresses to them. The matrix's nature defines different composite material categories:

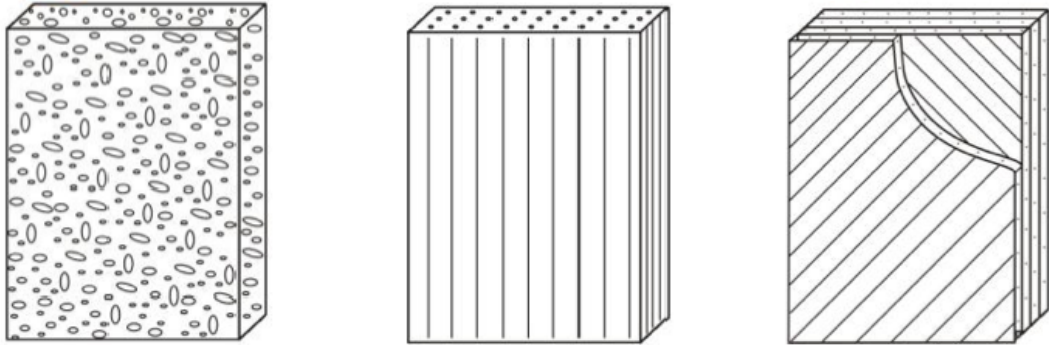
- ceramic-matrix composites (CMCs), in which the matrix is a ceramic material as the alumina (aluminium trioxide);
- metal-matrix composites (MMCs), with a metal matrix, generally aluminium or titanium or their alloys;
- polymer-matrix composites (PMCs), in which the matrix is a *thermoplastic* or a *thermosetting* polymer, like Nylon or epoxy resin.

Obviously, everyone of these matrices provide different characteristics to the composites: for example, in aeronautic applications a PMC is preferred since, thanks to its low density, it ensures a low weight of the final material. The reinforcement is represented by a phase scattered into the matrix in different ways and it is necessary to guarantee stiffness and mechanical strength to the material by sustaining most of the load applied to the structure. As has been done for the matrix, it is possible to classify composite material relative to the reinforcement's type:

- particle reinforced composites (PRC), in which the reinforcement is made of particles;
- fiber reinforced composites (FRC), in which is possible to have different kind of fibers (long, short) and fibers' orientation (unidirectional, multidirectional);
- structured composites, such as sandwich panels and laminated composite materials.

Since the reinforcement is the effective resistant constituent, the material's behavior can be isotropic or anisotropic, depending on the existence of a preferential orientation direction of the reinforcement. So it is intuitive that a particle reinforced composite is always isotropic while a fiber reinforced composite, with unidirectional fibers, is anisotropic. Furthermore, different reinforcements improve different material's characteristics: usually, particles are used to increase the resistance to wear, the superficial hardness, the workability and the resistance at high temperature; instead fiber reinforcement, the most common in mechanical constructions, is used

to improve the resistance to the static mechanical stresses in one direction, if unidirectional, or more directions, if multidirectional, keeping a low overall weight.



(a) Particle reinforced composite (b) Fiber reinforced composite (c) Structured composite (laminated)

Figure 1.3: Different type of composites, depending on the reinforcement's shape

1.2 Different matrices' natures

Following the classification done on the basis of the matrices' typology, it is useful to specify the different characteristics that the material assumes, so to justify the choices made in the continuation of the study.

1.2.1 Polymer matrices

They are made of polymers and, above all, they are the most widespread for both the construction simplicity and the restrained costs. It is possible to classify the matrices of possible use in two categories:

- thermoplastics;
- thermosets.

Thermosets The main characteristics of thermosets is that they require curing, with which they undergo a molecular cross-linking process, formed by strong covalent bonds. This procedure is irreversible and it renders them infusible: this means

that, once the process occurred, the resin cannot be reprocessed. They therefore offer high thermal stability, good rigidity and hardness, and resistance to creep. The use of a certain resin instead of another one depends on the temperature field the application requires. For temperature under 250°C , *epoxy* resins are preferred because of their better mechanical properties compared to other polymers, their excellent cohesion with fibers, good chemical resistance, low retrace, that means low residual stresses, and a remarkable thermal stability. This kind of resin is the most used in aeronautical and aerospace applications. Then, there are the *polyester* resins, used in combination with glass fibers, characterized by a low cost, a brief polymerization time and good mechanical properties: these ones are preferable in railway, naval, chemical and electrical applications. For temperatures above 250°C , *phenolic* resins are used, since they can guarantee the same epoxy's properties even at high temperature. The price to pay is represented by the high pressure required during the polymerization, the high void content and the typical black colour. Concerning what we said, it is possible to find them in high temperature applications [14].

Thermoplastics Resins with a linear molecular structure, which don't undergo chemical modification during the heating mold, are defined thermoplastics. The heat causes the melting and the solidification occurs during the cooling down process. The polymer chain associate through intermolecular forces, weaken rapidly with increased temperature, yielding a viscous liquid, thus it is possible to reshape thermoplastics by heating, but for a limited number of cycle, because too many processes can degrade the resins. They are usually reinforced with short discontinuous fibers such as fiberglass or carbon fibers. There are two major advantages of thermoplastic composites: the first is that thermoplastic resins have an increased impact resistance of comparable thermoset composites, in some instances even 10 times higher; the other major advantage is the ability to reform, that, in theory, also allows for recycling at the end of life. It is possible to find examples of common thermoplastics in polyethylene terephthalate (PET), polypropylene, polycarbonate, vinyl, polyethylene, nylon, polybutylene terephthalate (PBT) and polyvinyl chloride (PVC).

1.2.2 Metal matrices

This kind of matrix is little used because of problems inherent to the introduction of fibers inside the matrix, which has to be in liquid state but with a temperature that doesn't damage the fibers themselves. Another problem is to obtain a uniform fiber distribution and a perfect alignment. One of the most difficult requirement to respect is the wettability: frequently the metal matrix does not soak completely the fibers making it impossible to create a composite. However, the principal danger is represented by the temperature with which the matrix wets the fibers: in this case it is high, providing the potential to form intermediate deposits which damage the fibers. Despite these difficulties, the aerospace industry shows interest in the development of the metal-matrix composites because of their combination of low specific thickness and high resistance: indeed, some parts of the Space Shuttle's fuselage are made in MMCs because of the high operating temperature.

1.2.3 Ceramic matrices

The principal purpose of the reinforcement in this kind of material is to increase the toughness and the resistance typically limited of the ceramic matrices. As the metal matrix composite, the reinforcement can be in the form of particle, short or long fibers but, in every case, it is possible to have an increasing resistance thanks to the effect of the interruption of the crack's propagation. However what we want to obtain is a raising toughness: ceramic materials have interesting characteristics because of their strong covalent or partially covalent ionic bonds that produce a high Young modulus and a significant hardness, even at very high temperatures. Nevertheless, these same bonds that provides such an excellent characteristics, don't let the crystal lattices to slip, preventing any plastic deformation.

The principal problem is represented by the reinforcement's addition: the matrix can't be brought to the fusion point because it decompose before or their fusion temperatures are so high to react with the toughening phase. The only way is the sintering process, that imply to start from the dust to get the final material. Leaving out the difficulties of this process and the low quality obtained from it, the

application in the aerospace industry are numerous: brake disks, thermal barriers, combustion chambers and every situation requiring high temperature resistance.

1.3 Reinforcement phase

As stated before, the principal reinforcement typologies are fibers and particles. The use of a specific kind of reinforcements affects the behaviour of the composite material: in particular, the effective resistance and the degree of anisotropy change drastically between PMC or FRC. Since this is a thesis of aerospace interest, we will focus our attention on the fiber reinforced composite, avoiding the particle reinforced composites.

1.3.1 Fiber reinforcement

The fiber is the part constituting the reinforcement which has the task to serve as resistant part. Many materials have a elevated resistance when they are in fiber shape: glass, for example, normally considered fragile and little tough, has a $R_m = 170 \text{ MPa}$ in its classic form but it can reach the amount of 3500 MPa in fibers with diameter less than $100 \mu\text{m}$. The behaviour of carbon and graphite is similar. Anyway, fibers don't support compression loads, that is why they need a material to serve as matrix who distributes uniformly the stress on the reinforcement and protects them from chemically aggressive environments [1]. In the composite realization, fibers can be *continuous* or *discontinuous*: in the first case, they are long and their disposition is aligned to form woven or laminate, while, in the second instance, they are short and randomly arranged or aligned.

- *Discontinuous fibers* - $d = 1 \div 10 \mu\text{m}$, $L = 10 \div 100 d$ - can be arranged randomly or oriented. If randomly organized, they provide the material an isotropic behavior, as the particle reinforced composite. Instead, if aligned, the composite material is anisotropic or orthotropic;
- *Continuous fibers* - $L \geq 100 d$ - are oriented in a particular direction. Obviously, the behavior is intentionally anisotropic, with a better resistance in a

particular direction, as, for example, that of a specific load. Usually, the matrix is a resin, with good ductility and lightness, reinforced with very strong fibers made with glass, carbon or polymeric substances.

1.3.2 Principal types of fibers

Glass fibers Glass fibers are, by far, the most used reinforcement in the composite industry in order to replace heavier metal parts. Although glass weighs more than carbon, and is not as stiff, it confers a high impact-resistance and higher elongation. Anyway, the properties conferred to the fibers can widely change and different performance levels can be achieved simply modifying the glass type, the fiber diameter and form and the sizing chemistry [36]. Fiber properties are established by the fiber manufacturing process and the elements and coatings used in this process. During glass fiber production, raw materials are melted and formed into long and fragile filaments, varying in diameter between $3.5 \div 24\mu m$. The primary ingredient is silica sand, resulting in more than the 50% of the glass fiber's weight. Other particular materials like metal oxides can be added to the silica or it is possible to change the processing methods in order to obtain fibers for particular applications:

- *E-glass* is the standard form of glass fiber, accounting for more than 90%, well-know for electical applications (Electrical-glass). Its chemical composition makes it an excellent insulator and it is particularly well suited to applications in which radio-signal transparency is desired. It is the most economical glass fiber for composites, offering sufficient strenght in most employment;
- *S-glass* is a high traction resistant glass. Its resistance is, indeed, 33% greater than that one of E-glass and its Young modulus is 20% higher. This glass is usually used for aerospace applications where great resistance-to-weight ratios are required with good characteristics at high temperature and a high fatigue limit, all features that occurs in this kind of fibers;
- *D-glass* is another type of glass fiber, particularly suitable for electrical applications, thanks to its low dielectric constant and lower density, although its mechanical properties are worse than S and E glass ones;

- *C-glass* is the corrosion-resistant glass, that loses much less of its weight when exposed to an acid solution than does E-glass. However, E- and S-glass are much more resistant to sodium carbonate solution than is C-glass.

Carbon fibers The mechanical performance of carbon fibers derive from the particular crystalline structure of graphite: the stronger the crystalline structure, the better the final composite. A graphite crystal has a structure made by overlapping carbon atoms plane layers. The bonds between atoms belonging to same planes are strong (covalent bonds) while those ones between atoms of different layers are moderately weak (van der Waals forces): it is clear that the crystals are strongly anisotropic structures and it is up to the manufacture process to arrange the crystalline structure in the right direction. This is certainly hard to make and practically it is impossible to obtain perfect crystals and orientation precision that is why the resulting mechanical characteristics will be worse than theoretical ones.

To produce carbon fibers, you start with precursors, among which there are polyacrylonitrile (PAN), rayon and pitch, whose choice depend on the production cost, the process complexity and the speed of making, then the precursor fibers are chemically treated, heated and stretched to create high-strength fibers. The most common precursor employed in carbon fiber manufacturing process is PAN because of its amazing mechanical qualities such as high tensile strength (to 6800 *MPa*) and Young modulus. Furthermore, there are a lot of possible applications, ranging from aerospace structures to recreational goods: depending on the final curing temperature, in fact, different classes of carbon fibers are proposed, with different tenacity level and stiffness (from intermediate to ultra-high modulus) [30]. Another production technique starts from petroleum-pitch as precursor: these fibers have high to extremely high stiffness, lower tensile strength and low to negative axial coefficient of thermal expansion (CTE) and these properties are extensively adopted in high stiffness components who needs a good thermal conductivity.

The final product is made up of bundles called joms which have a low specific weight, low CTE, high mechanical resistance and stiffness. Although they are stronger than other kind of fibers, carbon fibers are less impact-resistant and they

can also experience galvanic corrosion in contact with metal: in order to overcome this problem, a barrier material or veil ply (often fiberglass/epoxy) is used during laminate layup [36].

Boron fibers Boron fibers are the result of a research program, whose primary objective was to examine the whole field of elements which have the characteristic to create a reinforcement, on the basis of high fusion point and low density criteria. They are obtained by means of a laser-assisted chemical vapor deposition which, precisely, deposits the elemental boron on a uniform tungsten wire substrate. This process is expensive, for both the cost of the tungsten thread and the deposition's scarce efficiency so they have considered to use, as substratum, the cheaper carbon thread; but during the deposition, boron experiences a remarkable elongation, causing the breakup of the filament carbon. To alleviate the problem the thread shall be covered by a thin pyrolytic graphite layer who postpones the breakup and protects the covering boron from damages.

Aramid fibers They are made up of synthetic polyamide chains, in which the 25% of amide bonds is connected to two aromatic cycles. The aramid fiber, thanks to a combination of excellent specific weight and high traction resistance, has a greater specific resistance of any other fiber both in terms of impact-resistance and of crack-propagation, as well as vibration damping. This is precisely why they are used in bulletproof vests and other armor and ballistic applications, but even for helicopter rotor blades, solid rocket motors, compressed natural gas tanks and other parts that must withstand high stress and vibration. For these applications, the most used aramid fibers are *Nomex* and *Kevlar*. The high cost of high-performance fibers can be a deterrent to their selection.

1.4 Composites for aerospace applications

Fiber-reinforced polymer composites materials, thanks to their combination of lightness and mechanical resistance, are becoming the preferred materials for aerospace

and aeronautical applications, as well as a field where remarkable results are achieved with research projects. «In particular, their use as primary structural materials in recent years in several technology-demonstrator front-line aerospace projects worldwide has provided confidence leading to their acceptance as prime materials for aerospace vehicles» [21]. This is obtained thanks to the will of the aerospace industry to improve the performance of commercial and military aircraft, that constantly drives the development of improved high performance structural materials.

As result of what was said, «the application of high performance composite materials to military aircraft can be traced back almost three decades to the F-14 (US Navy) and F-15(US Air Force) fighters, which use boron/epoxy skins in their empennages» [40]. Since then the use of composite materials in military and transport aircraft has increased. Initial applications to aircraft structures were in secondary structures such as fairings and control surfaces. With technological progresses, the use of composite materials for primary structures such as wings and fuselages has increased [10]. Instead, to find the first significant application of these materials in commercial transport aircrafts, it is necessary to move in Europe where Dasa Airbus introduced a rudder made entirely in composite for the A300 and A310 in 1983, followed in 1985 by a much more complex vertical tail fin. The first significative difference was that the metal vertical tail had about 2000 parts while the composite one had less than 100 parts. As a consequence, the composite vertical was not only lighter but also cheaper than the metal one thanks to the reduced part number and lower assembly costs. So, the usage of this new material with other design efficiencies led to significantly reduce the fuel consumption. Currently the A300-600 airframe weight is 4.5% composites [10].

Nowadays, thanks to their versatility, composites are used for both structural applications and components, in all aircraft and spacecraft, from complete airplanes such as the Beech Starship to helicopter rotor blades, wing assemblies, propellers, seats and instrument enclosures. Here there is reported a table, taken from Nayak [26], that summerizes the principal characteristics of the fibers.

Table 1.1: Different fibers commonly used in aerospace applications [26]

Fiber	Density g/cm^3	Modulus (GPa)	Strength (GPa)
Glass			
E-glass	2.55	65 – 75	2.2 – 2.6
S-glass	2.47	85 – 95	4.4 – 4.8
Aramid			
Low modulus	1.44	80 – 85	2.7 – 2.8
Intermediate modulus	1.44	120 – 128	2.7 – 2.8
High modulus	1.48	160 – 170	2.3 – 2.4
Carbon			
Standard modulus	1.77 – 1.80	220 – 240	3.0 – 3.5
Intermediate modulus	1.77 – 1.81	270 – 300	5.4 – 5.7
High modulus	1.77 – 1.80	390 – 450	2.8 – 4.5
Ultra-High strength	1.80 – 1.82	290 – 310	7.0 – 7.5

The application areas are:

- **Glass fibers**

- *E-glass* - small passenger a/c parts, aircraft interiors, secondary parts; rocket motor casing;
- *S-glass* - highly loaded parts in small passenger a/c ;

- **Aramid fibers**

- *Low modulus* - fairings; non-load bearing parts;
- *Intermediate modulus* - radomes, structural parts; rocket motor casings;
- *High modulus* - highly loaded parts;

- **Carbon fibers**

- *Standard modulus* - almost all types of parts in a/c, satellites, antenna dishes, missiles;

- *Intermediate modulus* - primary structural parts in high performance fighters;
- *High modulus* - space structures, control surfaces in a/c;
- *Ultra-High strength* - primary structural parts in high performance fighters, spacecraft [26].

It was chosen to study carbon fibers thanks to their versatility and greater use in both transport and military aircraft, while, for the matrix, a thermoset resin was picked: the *epoxy* resin is the most popular one, with a moderately high temperature of usage, a low shrinkage (2 – 3%) and a its comparatively ease of process, that makes possible to give varieties of structure, morphologies and wide range of properties, although it is more expensive than other thermosets like phenolic, polyester or polyimides.

1.5 The repeating unit cell

The main purpose of this study is the prediction of the fracture in composite materials, largely described previously. To achieve this goal, it must be considered the effective of the reinforcement's disposition in the matrix: indeed, the distance between two fibers widely influences the stress and strain fields which defines the crack initiation. The theory behind the fracture behavior of a composite material and the derived strength will be discussed in the later chapters, but here is important to introduce the repeating unit cells. They are cell models containing a certain number of fibers, used to obtain the structure of a composite material: in many kind of composites, such as unidirectional fiber reinforced composites, the macrostructure can be seen as made by a periodic array of a simpler microstructure, i.e. the repeating unit cell [43]. So, exploiting the simplicity of the analysis of this cell, which is characterized by reduced dimensions, the overall behavior of a more complex material can be derived. A periodic-array microstructure assumption has as consequence the limitation that the reinforcement phase has constant size and orientation [23]. This is not necessarily true in actual materials, since mistakes in the manufacturing

process could cause the variation in size and distribution of the fibers in the matrix. However, considering that here the subject of study are unidirectional fiber composite materials, we can assume that the fibers are uniformly sized: a fiber diameter of $6\ \mu\text{m}$ is considered for the whole reinforcement phase from now on.

1.5.1 Periodic boundary conditions

So, the usage of a repeating unit cell entails that the entire material should be derived by a repetition along the cross-section space of the basic cell. For this reason, it is necessary to ensure the continuity between neighboring RUCs so that, when the cell is prone to deformations, any separation in the structure will occur [13]. What was said can be achieved by means of periodic boundary conditions, a set of equations (see eq.1.1) in terms of displacements which guarantee that each RUC in the entire structure has the same mode of deformation so that there is no gap or overlap between contiguous RUCs [42]. Considering an arbitrary quadrilateral RUC in the underformed configurations with one corner point placed at the origin $(0, 0, 0)$, the equations corresponding to the periodic boundary conditions are [11]

$$\begin{aligned}
 u_x(L_1, y, z) - u_x(0, y, z) &= \varepsilon_{xx}L_1, \\
 u_y(L_1, y, z) - u_y(0, y, z) &= 2\varepsilon_{xy}L_1, \\
 u_z(L_1, y, z) - u_z(0, y, z) &= 2\varepsilon_{xz}L_1, \\
 u_x(x, L_2, z) - u_x(x, 0, z) &= 2\varepsilon_{yx}L_2, \\
 u_y(x, L_2, z) - u_y(x, 0, z) &= \varepsilon_{yy}L_2, \\
 u_z(x, L_2, z) - u_z(x, 0, z) &= 2\varepsilon_{yz}L_2, \\
 u_x(x, y, L_3) - u_x(x, y, 0) &= 2\varepsilon_{zx}L_3, \\
 u_y(x, y, L_3) - u_y(x, y, 0) &= 2\varepsilon_{zy}L_3, \\
 u_z(x, y, L_3) - u_z(x, y, 0) &= \varepsilon_{zz}L_3
 \end{aligned} \tag{1.1}$$

where L_1 , L_2 and L_3 are the lengths of the cell along the x , y and z directions respectively, u_x , u_y and u_z are the displacement of the RUC boundary along the x , y and z direction and ε_{ij} is the tensorial strain [11].

1.5.2 RUCs realizations

The following figures represent the RUCs created for the analysis. As said before, the fiber diameter d_f is constant and equal to $6 \mu m$ while the fiber volume fraction, defined by

$$V_f = \frac{v_f}{v_c} \quad (1.2)$$

where v_f is the volume of the fibers contained within the volume of the cell v_c , is equal to 0.52.

Three different type of RUC are taken into account, containing 5, 10 or 30 fibers randomly arranged. Every RUC is a square and it is simple to evaluate the length of the cell's side, from the total area of the fibers, given by $(\pi r_f^2) \times N_f$, where r_f is the fiber radius and N_f is the number of fibers, divided by the fiber volume fraction V_f .

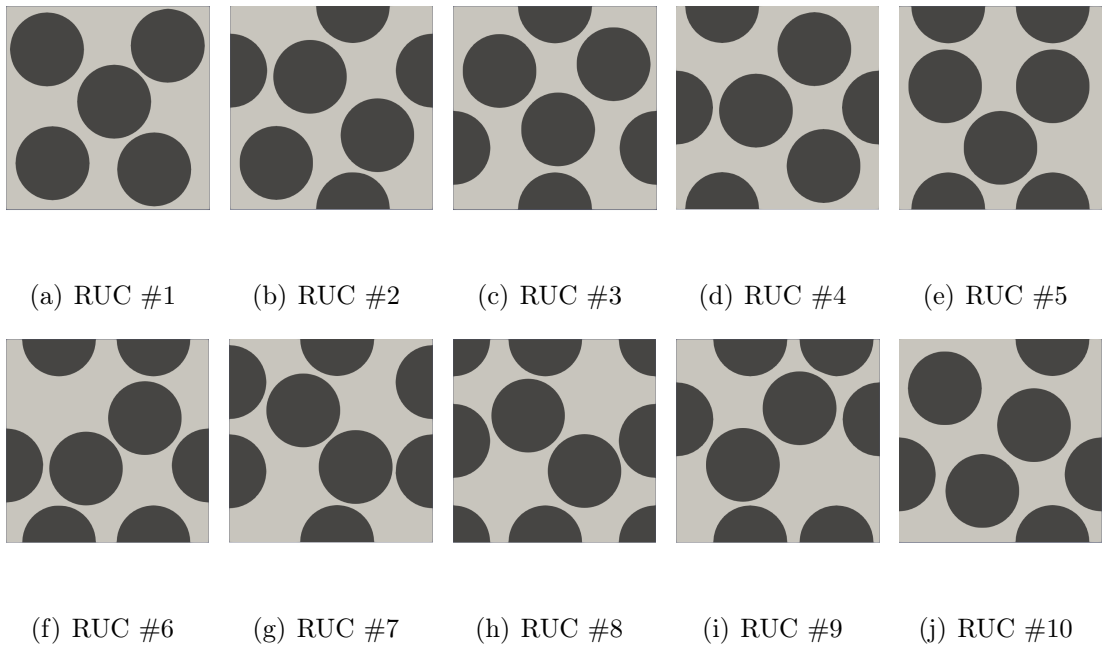


Figure 1.4: Five-fibers RUC renditions, $L = 16.49 \mu m$

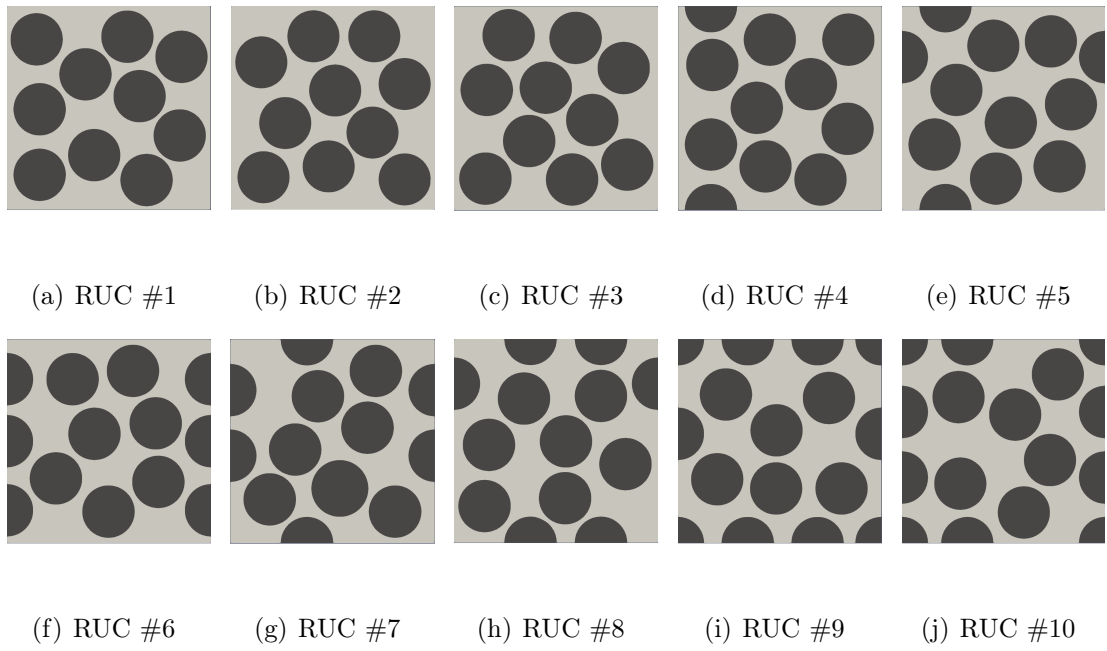


Figure 1.5: Ten-fibers RUC renditions, $L = 23.32 \mu m$

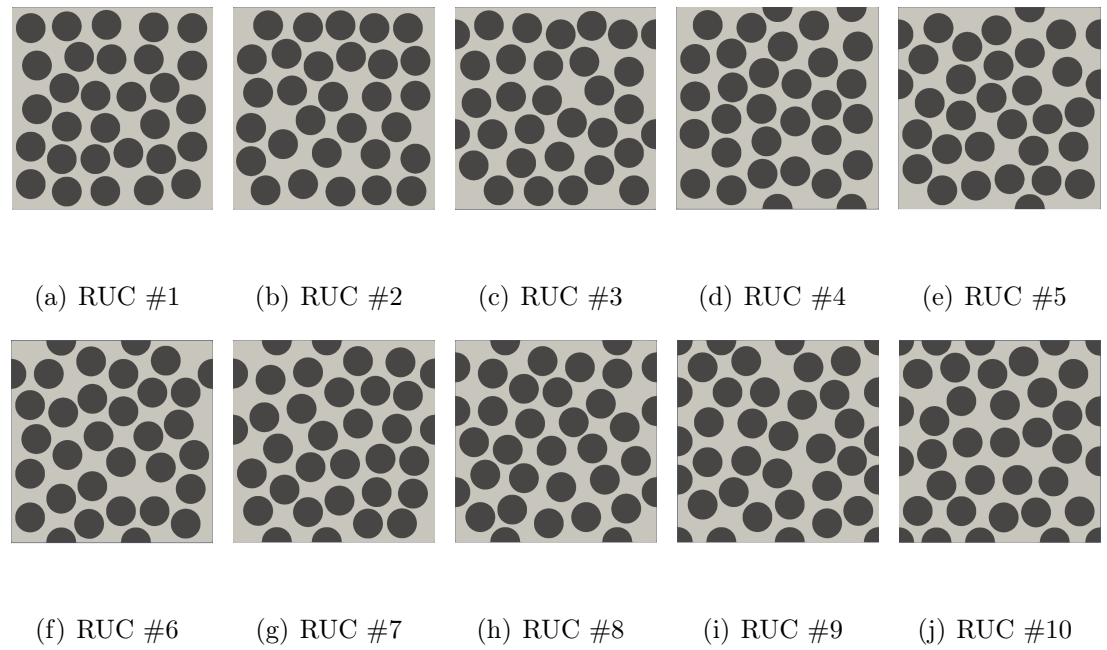


Figure 1.6: Thirty-fibers RUC renditions, $L = 40.39 \mu m$

Chapter 2

Theoretical background: Finite Elements Method and Unified Formulation

The laws describing every physical phenomena are usually expressed in terms of partial or ordinary differential equations (PDEs or ODEs). This means that, to have a solution of typical problems in a area of interest such as structural analysis, fluid flow, mass transport, heat transfer and electromagnetical potential, boundary value problems must be solved analytically.

For the vast majority, these problems, with different geometries, cannot be solved with classical methods. So, an approximation of the equations can be constructed typically based upon different types of discretizations: these methods approximate the partial differential equations with numerical model equations, resulting in an algebraic system. The solutions of the numerical model equations are, in turn, an approximation of the real solution to the PDEs or the ODEs. In order to obtain what was said, the finite elements method (FEM) is used.

The finite elements method yields values of the unknowns at discrete number of points over the domain, called nodes. To solve the problem, it subdivides a domain of interest into smaller, simpler parts that are called finite elements and then the simpler equations which describe these finite elements are assembled into a larger system of equations that models the entire problem. In the end, an associated

error function is minimized to approximate a solution. For this purpose, variational methods from the calculus of variation is used.

There are two important peculiarity in FEM that make this method so popular:

1. «piece-wise approximation of physical fields on finite elements provides good precision even with simple approximation functions (increasing the number of elements we can achieve any precision)» [27];
2. «locality of approximation leads to sparse equation system for a discretized problem. This helps to solve problems with very large number of nodal unknown» [27].

As said, to enhance the precision of the method, i.e. to obtain a more realistic solution, it is important to increase the number of elements which describes the physical domain: this means that a greater number of algebraic equations must be solved and therefore a lot of time to perform the calculations. For this reason, the turning point in the application of the finite element methods there was when computers capable to quickly solve complex algebraic systems were developed. Similarly, even innovations in mathematical field were waited: in particular, methods that can be used to approximate the differential equations were necessary, among which an especially significant one is the weight residual method [6].

2.1 Introduction to the Unified Formulation

Considering now that the Finite Elements analysis is common knowledge, so to not dwell on the procedures characterizing this method, it is important to introduce a new method to derive the FE matrices and vectors which are involved in every study about the mechanics of structures: the Carrera Unified Formulation (CUF).

The CUF is a class of theories of structures, for both one dimensional (beam) and two dimensional (plate and shell) cases, who, using a condensed notation, allows us to express the displacement field along the cross-section or the thickness as an expansion with arbitrary functions. The result of this notation is called *Fundamental Nuclei*, simple matrices or vectors independent from the theory of structures used,

and it can provide, with a low computational cost, the same results obtained only by 3D elements by using only 1D and 2D finite elements [6]. So, the derivation of the Fundamental Nuclei is essential and it is here analyzed.

2.2 FEM and Theory of structures approximations

Let us consider a simple structure, such as a cantilevered beam, and let's take into account the displacement field along the three direction x and z , the cross-section coordinates, and y the axial direction. In the most general situation, the three displacement components, who are called u_x , u_y and u_z , where the subscript indicates the direction of the displacement, are dependent from the three coordinates of the space

$$\begin{aligned}u_x &= u_x(x, y, z) \\u_y &= u_y(x, y, z) \\u_z &= u_z(x, y, z)\end{aligned}\tag{2.1}$$

So, we can include these three components in a vector \mathbf{u} ¹ which can be expressed as follows

$$\mathbf{u}^T = (u_x, u_y, u_z)\tag{2.2}$$

At this point, as the Finite Elements formulation suggests, the entire structure can be discretized along the axial direction y , into a set of simpler elements defined by the nodes: in this way, the displacement field can be seen as the sum of the nodal displacements u_i multiplied by a shape function N_i

$$u(x, y, z) = N_i(y)u_i(x, z)\tag{2.3}$$

where the repeating indexes follow the Einstein notation. As we can notice, the dependence from the three coordinates is so splitted and, while the shape functions take the y -axis dependence, the nodal displacements become only dependent by the cross-section coordinates x and z .

¹From now on, all the variables reported in bold are vectors or matrices

Now, it is possible to introduce the Unified Formulation by considering the nodal displacements, as done by the finite elements formulation, as the sum of generic functions $F_\tau(x, y)$ multiplied by a coefficient $u_{\tau i}$

$$\begin{aligned} u_i(x, z) &= F_\tau(x, z)u_{\tau i} \\ &= F_1(x, z)u_{1i} + F_2(x, z)u_{2i} + \dots + F_\tau(x, z)u_{\tau i} + \dots + F_m(x, z)u_{mi} \end{aligned} \quad (2.4)$$

where m is the number of terms in the expansion and $u_{\tau i}$ are the actual unknown. So, the final displacement field will be expressed in term of a double expansion, depending from two indexes, τ and i :

$$\mathbf{u} = N_i(y)F_\tau(x, z)\mathbf{u}_{\tau i} = \sum_{i=1}^n \sum_{\tau=1}^m N_i F_\tau \mathbf{u}_{\tau i} \quad (2.5)$$

and even its virtual variation can be expressed with the same notation just changing the indexes from τ and i to s and j

$$\delta \mathbf{u} = N_j(y)F_s(x, z)\delta \mathbf{u}_{sj} \quad (2.6)$$

2.3 Derivation of the Fundamental Nucleus

In order to apply the finite element method, the first thing to do is to write the geometrical relations and the constitutive equations from the displacement field, in a way similar to the eq.2.5. The geometrical relation that we need is between strain and displacement by means of the partial derivative

$$\varepsilon_{ij} = \frac{1}{2} \left(\frac{\partial u_i}{\partial x_j} + \frac{\partial u_j}{\partial x_i} \right) \quad (2.7)$$

while the constitutive equation is given by the Hooke's law, which link stress and strain by using of the material coefficient matrix \mathbf{C}

$$\boldsymbol{\sigma} = \mathbf{C}\boldsymbol{\varepsilon} \quad (2.8)$$

Considering that the displacement field is 3-dimensional, we can write the differential operator \mathbf{b} as follows

$$\mathbf{b} = \begin{bmatrix} \partial/\partial x & 0 & 0 \\ 0 & \partial/\partial y & 0 \\ 0 & 0 & \partial/\partial z \\ \partial/\partial z & 0 & \partial/\partial x \\ 0 & \partial/\partial z & \partial/\partial y \\ \partial/\partial y & \partial/\partial x & 0 \end{bmatrix} \quad (2.9)$$

so that the strain and the stress become

$$\boldsymbol{\varepsilon}(x, y, z) = \mathbf{b}N_i(y)F_\tau(x, z)\mathbf{u}_{\tau i} \quad (2.10)$$

$$\boldsymbol{\sigma}(x, y, z) = \mathbf{C}\mathbf{b}N_i(y)F_\tau(x, z)\mathbf{u}_{\tau i} \quad (2.11)$$

and the virtual variation

$$\delta\boldsymbol{\varepsilon}(x, y, z) = \mathbf{b}N_j(y)F_s(x, z)\delta\mathbf{u}_{sj} \quad (2.12)$$

At this point it is easy to derive the virtual variation of the internal work δL_{int} , made by the integral on the volume of the virtual variation of the strain multiplied by the stress

$$\begin{aligned} \delta L_{int} &= \int_V \delta\boldsymbol{\varepsilon}^T \boldsymbol{\sigma} dV = \delta\mathbf{u}_{sj} \mathbf{k}^{\tau sij} \mathbf{u}_{\tau i} \\ &= \delta\mathbf{u}_{sj}^T \int_V \left[F_s(x, z)N_j(y)\mathbf{b}^T \mathbf{C}\mathbf{b}N_i(y)F_\tau(x, z) \right] dV \mathbf{u}_{\tau i} \end{aligned} \quad (2.13)$$

where the 3×3 matrix $\mathbf{k}^{\tau sij}$ is the *fundamental nucleus* and it is made by [6]

$$\mathbf{k}^{\tau sij} = \int_V F_s(x, z)N_j(y)\mathbf{b}^T \mathbf{C}\mathbf{b}N_i(y)F_\tau(x, z) dV \quad (2.14)$$

2.4 Assembly technique

The derivation of the matrices through the Unified Formulation can be easily implemented in computer code by using four loops on the four indexes i , j , τ and s . The

finite element matrix will be the results of these loops where the fundamental nucleus is evaluated for every combination of these indexes. Here is reported a scheme, taken from the book cited in [6], that make easy to understand how this assembly procedure can be obtained to describe and entire structure

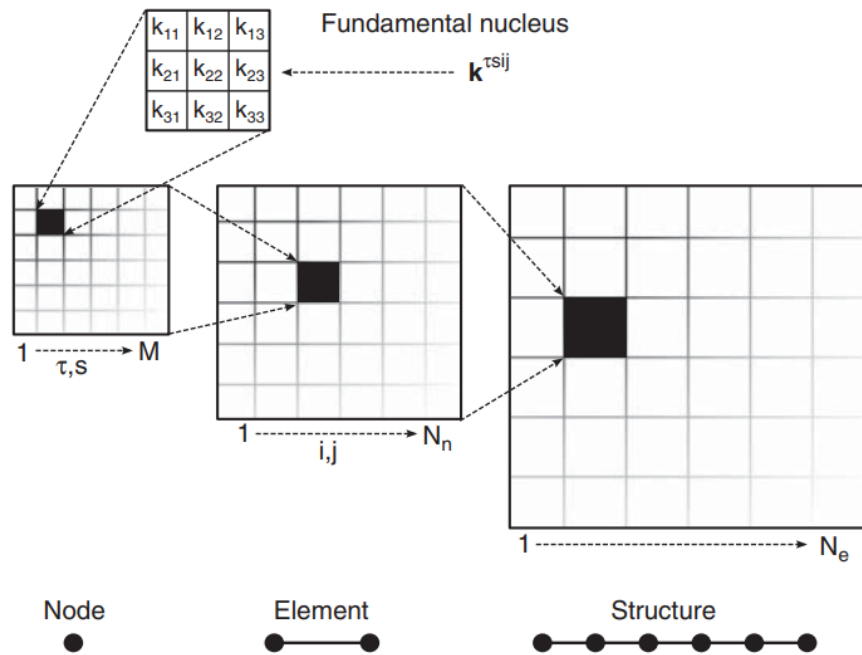


Figure 2.1: «Representation of the assembly procedure: the fundamental nucleus is the core, the loops on τ and s build the matrix for a given pair of i and j , the loops on i and j give the matrix of the elements, and the loop on the elements give the global stiffness matrix» [6]

2.5 Weak Form of the Solid Model

At this point, it is possible to use the Principle of Virtual Displacements to derive the equilibrium equations in terms of the Fundamental Nuclei. In particular, there are two possible forms of the equilibrium equations:

- the "strong" form, who is the entire formulation of the equilibrium equations without any simplification, in terms of displacements, stresses and strains. It allow us to evaluate the equilibrium of a generic point into a generic body, but, as we can imagine, these kind of equations are difficult to solve and they can be used only for simple geometries and simple boundary conditions;

- the "weak" form, which instead can be used to solve the problem in a lot of practical applications and which satisfies the equation derived for the strong form only according to an integral criterion. Thanks to the assumption of this weak form, the derivative of the virtual displacements can be approximated without using the integration by part [6].

Now, considering that the Principle of Virtual Displacements (PVD) is given by the equivalence between the work done by the external tractions and body forces on an admissible displacement field and the work done by the equilibrated stresses (solution of the actual problem) on the virtual strain, which corresponds, in a static case, to

$$\delta L_{int} = \delta L_{ext} \quad (2.15)$$

it is necessary to obtain the virtual variation of the external work (δL_{ext}) following what has been done in the book [6].

Let us consider as known the vector containing the external loads, acting for simplicity at the nodes of the body that we are analyzing: this vector can be expressed as \mathbf{P} . To obtain the external work, we need a vector containing the virtual nodal displacements, that is $\delta \mathbf{U}$, even used to write the displacement field in the finite element method: from this, it is immediate

$$\delta L_{ext} = \delta \mathbf{U}^T \mathbf{P} \quad (2.16)$$

The displacement field \mathbf{u} can be written, in accordance to the finite elements method, as the product of the nodal displacements and the shape functions (usually Lagrange polynomials)

$$\mathbf{u} = \mathbf{N} \mathbf{U} \quad (2.17)$$

from whom we can obtain the strain

$$\boldsymbol{\varepsilon} = \mathbf{b} \mathbf{u} = \mathbf{b} \mathbf{N} \mathbf{U} = \mathbf{B} \mathbf{U} \quad (2.18)$$

The virtual variation of the internal work derived from this notation and from the application of the Hooke's law is

$$\delta L_{int} = \int_V \delta \boldsymbol{\varepsilon}^T \boldsymbol{\sigma} dV = \int_V \delta \boldsymbol{\varepsilon}^T \mathbf{C} \boldsymbol{\varepsilon} dV = \int_V \delta \mathbf{U}^T \mathbf{B}^T \mathbf{C} \mathbf{B} \mathbf{U} dV \quad (2.19)$$

Since the nodal displacements are constant on the volume, they can be removed from the integral

$$\delta L_{int} = \delta \mathbf{U}^T \left(\int_V \mathbf{B}^T \mathbf{C} \mathbf{B} dV \right) \mathbf{U} \quad (2.20)$$

where

$$\int_V \mathbf{B}^T \mathbf{C} \mathbf{B} dV = \mathbf{K} \quad (2.21)$$

So, from the equivalence of the principle of the virtual work derives

$$\delta \mathbf{U}^T \mathbf{K} \mathbf{U} = \delta \mathbf{U}^T \mathbf{P} \quad (2.22)$$

which means

$$\mathbf{K} \mathbf{U} = \mathbf{P} \quad (2.23)$$

the equilibrium equation in "weak" form for a structural element [6].

2.6 The Taylor expansion class

The definition of the equilibrium equations for a structural model goes through the characterization of a proper displacement field, for both the shape functions and the terms of the expansion F_τ who defines the cross-section behavior: the Unified Formulation allows to choose arbitrarily the number of terms, i.e. the order of the expansion and the accuracy of the displacement field above the cross-section. It is considered as well-known the choice of the shape functions $N(y)$, that usually are Lagrange polynomials, so we can focus our attention on the two possibilities for the class of expansion: the Taylor- and the Lagrange-class. Here is presented the Taylor-like expansion and the relevant fundamental nuclei [6].

It is possible to start showing the complete linear expansion model, made by a first-order Taylor-like polynomial. From now on, N is the order of the expansion: for this linear case $N = 1$. The displacement field is given by the following equations:

$$\begin{aligned} u_x &= u_{x_1} + xu_{x_2} + zu_{x_3} \\ u_y &= u_{y_1} + xu_{y_2} + zu_{y_3} \\ u_z &= u_{z_1} + xu_{z_2} + zu_{z_3} \end{aligned} \quad (2.24)$$

where, as we can see, there are 9 displacements variables and it showed a complete linearity in x and z . This linear model is responsible of a constant distribution of the strain above the cross-section ($\varepsilon_{xx}, \varepsilon_{zz}$ and γ_{xz}) and a linear one of the strain along the axial direction ($\varepsilon_{yy}, \gamma_{xy}$ and γ_{yz} , see Eq.2.7). It should be noticed that, with some simplifications, from this model is possible to obtain the Euler-Bernoulli and the Timoshenko beam theory (EBBT, TBT).

2.6.1 Unified formulation of expansion

On the basis of what we have said in the previous sections, in according to the Einstein notation the displacement vector can be written as

$$\mathbf{u} = F_{\tau} \mathbf{u}_{\tau} \quad (2.25)$$

where

$$\mathbf{u} = \begin{bmatrix} u_{x_1} + xu_{x_2} + zu_{x_3} \\ u_{y_1} + xu_{y_2} + zu_{y_3} \\ u_{z_1} + xu_{z_2} + zu_{z_3} \end{bmatrix} \quad (2.26)$$

So, the expansion's functions F_{τ} are

$$\begin{aligned} F_{\tau=1} &= 1 \\ F_{\tau=2} &= x \\ F_{\tau=3} &= z \end{aligned} \quad (2.27)$$

2.6.2 Higher-order Taylor expansion class

The linear model is sufficient to describe simple situation as the bending of a beam, but, in order to derive the mechanical response for complex loads, boundary conditions or geometry, higher orders are required [6]. In the unified formulation, it is possible to define the displacement field starting from the Eq.2.25 where F_{τ} are functions of the cross-section coordinates x and z while u_{τ} are the unknown nodal displacements: so, to get a higher order of the description, i.e. a more accurate description of the mechanical phenomenon, it is sufficient to increase the order of the

functions of x and z . Obviously, as the order of the functions increases, the number of the unknowns will increase too, which means an increasing computational cost.

In the following table, various F_τ are specified until $N = 3$, where M is the number of terms in the expansion

Table 2.1: Taylor-like expansion [6]

N	M	F_τ
0	1	$F_1 = 1$
1	3	$F_2 = x, F_3 = z$
2	6	$F_4 = x^2, F_5 = xz, F_6 = z^2$
3	10	$F_7 = x^3, F_8 = x^2z, F_9 = xz^2, F_{10} = z^3$
\vdots	\vdots	\vdots
N	$(N + 1)(N + 2)/2$	$F_{(N^2+N+2)/2} = x^N, \dots, F_{(N+1)(N+2)/2} = z^N$

For orders greater than 3, a technique similar to the Tartaglia’s triangle can be used to evaluate F_τ , considering every F as the product of the elements above on the left and on the right.

2.7 The Lagrange expansion class

To define the displacement field of structures, different classes of functions can be chosen, such as harmonics, exponentials or polynomials. Among these, the second class of functions on which is based the CUF models consists of the Lagrange polynomial expansions, where the F_τ expansion functions coincide with the Lagrange polynomials, similarly to what happen for the shape functions N , while the unknown variables u_τ are nodal displacements, that can be physically placed on the structure discretizing the cross-section with a set points [6].

This particular class of functions can be useful in many situation thanks to its features. First of all, the Lagrange expansion is dependent only on the elements used to discretize the cross-section: this means that a local refinement of the model can be simply done refining the discretization of the structure. Moreover, the unknown variables are displacement components, without rotations or higher-order variables.

What was described, lead to enhanced capabilities of the CUF Lagrangian-Elements models in terms of accuracy and computational cost.

The first important thing to remember about the Lagrange polynomials is that, usually, they are given in terms of normalized coordinates, even though this is not a compulsory choice: its utilisation is preferred because, with respect to the actual coordinates, it entails to advantages that will be discussed in the next paragraphs. Since the Lagrange polynomials depend on the number of nodes of discretization, different solutions are presented having different features in terms of accuracy and computational cost. This lead to the definition, as done in the book Carrera et al. [6], of different sets of elements with triangular or quadrilateral shape, containing respectively 3 or 6 nodes and 4 or 9 nodes.

Because of the choices done in this thesis, here only the quadrilateral elements will be presented.

2.7.1 Normalized coordinates and Lagrange polynomials

As said before, two kinds of quadrilateral elements can be used: the simplest Lagrange polynomial involves four points above the cross-section and the relevant elements is so called $L4$, as we can see from Fig.2.2 in which α and β are the normalized cross-section axis [6].

Similarly to what we have done for the Taylor expansion class, it is possible to define the F_τ for the displacement field, in terms of the normalized coordinates (see Eq.2.28 below)

$$F_\tau = \frac{1}{4}(1 + \alpha\alpha_\tau)(1 + \beta\beta_\tau), \quad \tau = 1, 2, 3, 4 \quad (2.28)$$

where α_τ and β_τ are the coordinates of the normalized cross-section's nodes, presented in the table below.

Table 2.2: Normalized coordinates of the four-nodes cross-section [6]

<i>Point</i>	α_τ	β_τ
1	-1	-1
2	1	-1
3	1	1
4	-1	1

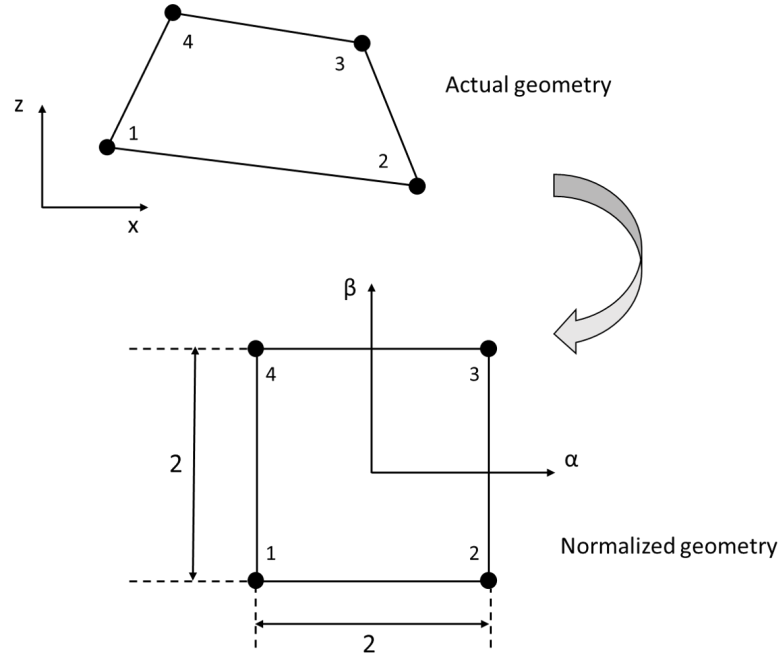


Figure 2.2: Lagrange element with four-nodes in actual and normalized coordinates

In practice, the $L4$ expansion can be seen as a linear expansion in α and β , with the addition of a bilinear term $\alpha\beta$.

Now, to enhance the accuracy of the description of the displacement field, the $L9$ elements are introduced, adding a node for every side of the quadrilateral and another one in the center (see Fig.2.3). The equations of the F_τ are given by [6]

$$\begin{aligned}
 F_\tau &= \frac{1}{4}(\alpha^2 + \alpha\alpha_\tau)(\beta^2 + \beta\beta_\tau), \quad \tau = 1, 3, 5, 7 \\
 F_\tau &= \frac{1}{2}\alpha_\tau^2(\alpha^2 + \alpha\alpha_\tau)(1 - \beta^2) + \frac{1}{2}\beta_\tau^2(\beta^2 + \beta\beta_\tau)(1 - \alpha^2), \quad \tau = 2, 4, 6, 8 \\
 F_\tau &= (1 - \alpha^2)(1 - \beta^2), \quad \tau = 9
 \end{aligned} \tag{2.29}$$

where the coordinates $(\alpha_\tau, \beta_\tau)$ of the nodes in the normalized system are exhibited in the table 2.3

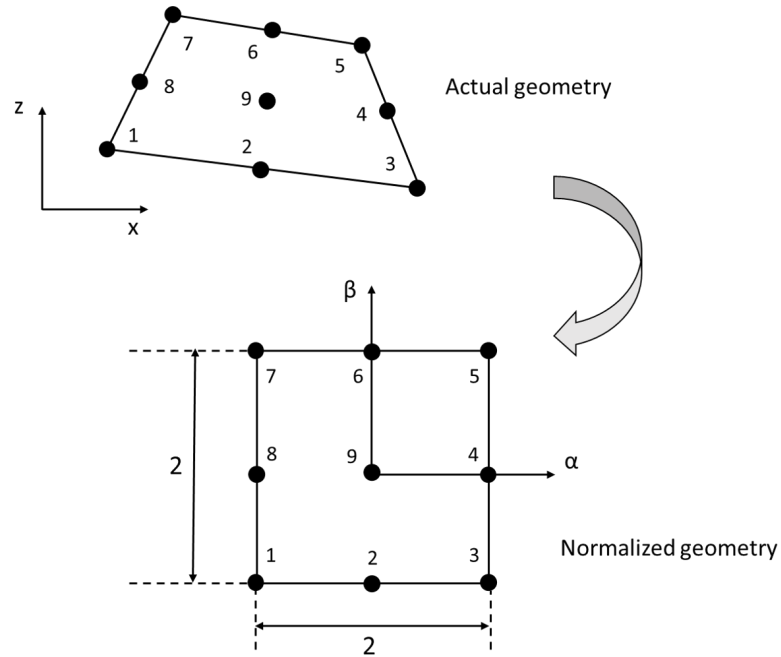


Figure 2.3: Lagrange element with nine-node in actual and normalized coordinates

Table 2.3: Normalized coordinates of the nine-nodes cross-section [6]

<i>Point</i>	α_τ	β_τ
1	-1	-1
2	0	-1
3	1	-1
4	1	0
5	1	1
6	0	1
7	-1	1
8	-1	0
9	0	0

2.7.2 Displacement field with a Lagrange elements

Now, in order to describe the cross-section displacement field, Lagrange elements are used, defined by a set of Lagrange polynomials. We have already said that the unknown variables of the displacement field are only translational displacements:

moreover, since every Lagrange elements is defined by a set of given point, it is possible to place the unknowns on the physical surface of the body using a discretization of the cross-section [6]. Obviously, since every node is linked to an unknown variable, the definition of the cross-section mesh define in turn the degrees of freedom of the structure, i.e. the computational cost.

The displacement field introduced by a $L4$, the Lagrange polynomial with four nodes is

$$\begin{aligned} u_x &= F_1 u_{x_1} + F_2 u_{x_2} + F_3 u_{x_3} + F_4 u_{x_4} \\ u_y &= F_1 u_{y_1} + F_2 u_{y_2} + F_3 u_{y_3} + F_4 u_{y_4} \\ u_z &= F_1 u_{z_1} + F_2 u_{z_2} + F_3 u_{z_3} + F_4 u_{z_4} \end{aligned} \quad (2.30)$$

while the one related to the $L9$ is

$$\begin{aligned} u_x &= F_1 u_{x_1} + F_2 u_{x_2} + F_3 u_{x_3} + F_4 u_{x_4} + F_5 u_{x_5} + F_6 u_{x_6} + F_7 u_{x_7} + F_8 u_{x_8} + F_9 u_{x_9} \\ u_y &= F_1 u_{y_1} + F_2 u_{y_2} + F_3 u_{y_3} + F_4 u_{y_4} + F_5 u_{y_5} + F_6 u_{y_6} + F_7 u_{y_7} + F_8 u_{y_8} + F_9 u_{y_9} \\ u_z &= F_1 u_{z_1} + F_2 u_{z_2} + F_3 u_{z_3} + F_4 u_{z_4} + F_5 u_{z_5} + F_6 u_{z_6} + F_7 u_{z_7} + F_8 u_{z_8} + F_9 u_{z_9} \end{aligned} \quad (2.31)$$

So, it is not so difficult to evaluate the degrees of freedom of the expansions, which is given by the number of unknown variables u_{x_1}, \dots, u_{z_N}

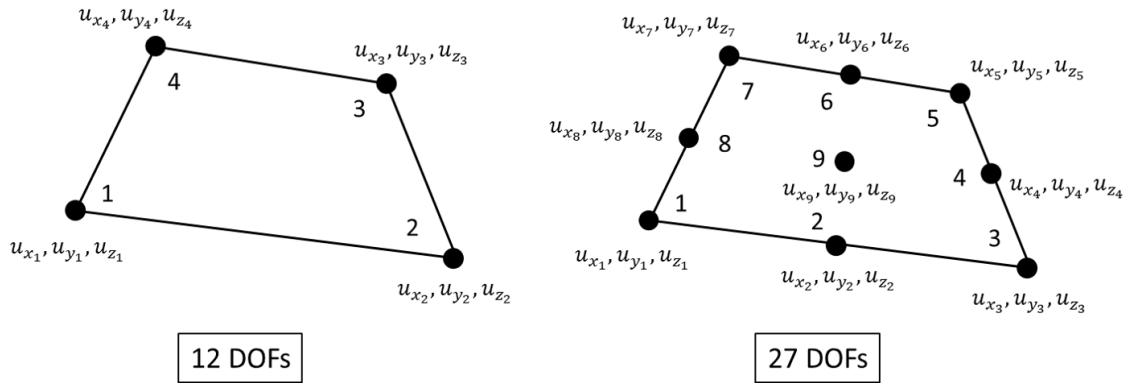


Figure 2.4: $L4$ and $L9$ elements with the relevant Degrees of Freedom

2.7.3 Locally refined cross-sections

The other important feature of the Lagrange expansion class is that, since the polynomials depend on the points of the cross-section discretization, it is possible to

obtain a more accurate model just increasing the density of the mesh: in particular, this possibility can be exploited to refine locally the structural model, as, for example, if there is the necessity to impose geometrical discontinuities [6]. The utilisation of several Lagrange elements for the discretization requires the definition of a local and a global connectivity, as it can be seen in the following figures in which there is an example of structure made by two $L9$ elements.

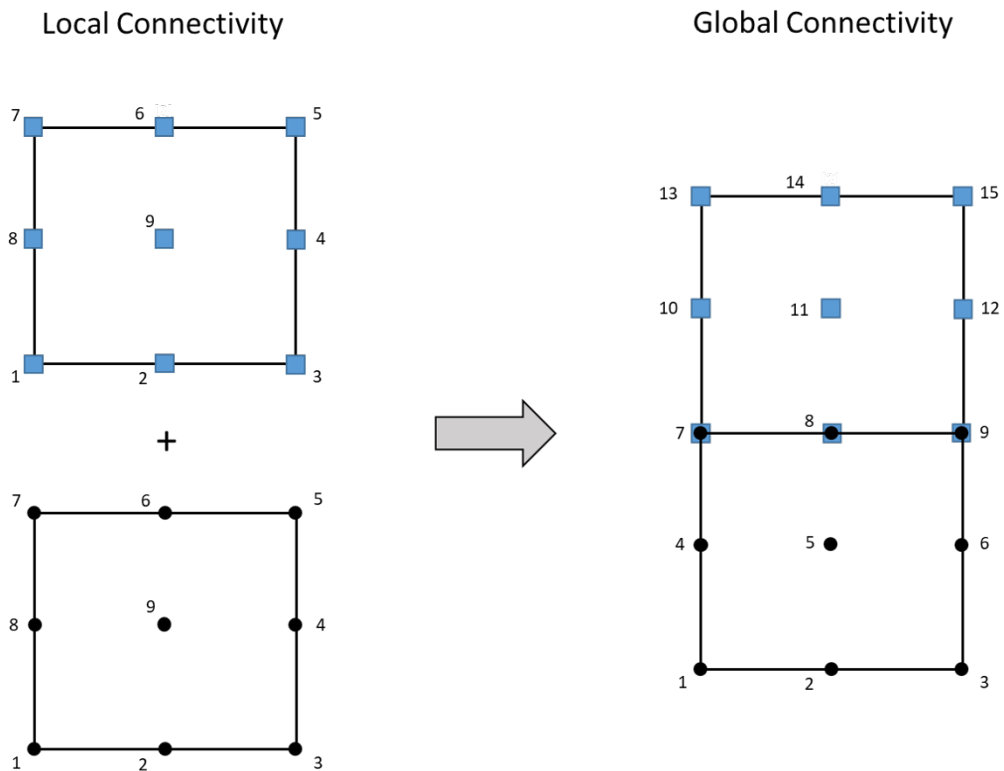


Figure 2.5: An example of two elements assembled

So, the most interesting feature is given by the local refined models, which can be used when local effects are discriminatory for the global behavior of the structure. A typical example is given by a thin-walled structure under the action of a punctual load on both the top and the bottom edges [6]. In fact, the displacement of the cross-section is accentuated close to the loading points, while the load is much less effective on the vertical edges. To properly detect the resulting displacement using the Taylor-like expansion, it is necessary to increase the order of the terms which defines the displacement field acting globally on the structure's cross-section, even where the effect of the loads is not marked; conversely, using the Lagrange polynomials is

possible to increase the number of the nodes where they are necessary, resulting in fewer degrees of freedom. (see Fig.2.6).

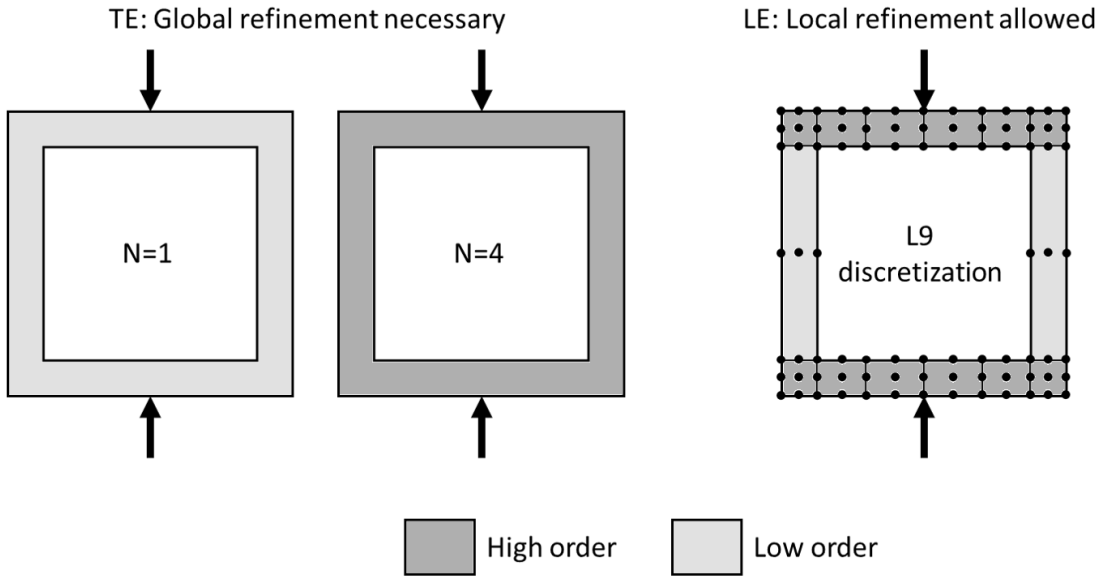


Figure 2.6: Different refinement for TE and LE elements

Actually, the local refinement is possible even using the TE elements but the process would require the imposition of compatibility conditions by means of Lagrange multipliers [6].

Now, after the introduction to the theoretical basis of the Unified Formulation, in the next chapter several structures will be analyzed using these procedures.

Chapter 3

CUF application: assessment of referred structures

The purpose of this chapter is to analyze some referred structures using the Carrera Unified Formulation. The use of this particular approach can be extended to a large casuistry who concerns the static and the modal analysis of different structures, from simple cantilever beams to more complex geometries, and even usual micromechanical problems of simple and complex composite structures, variable from a single fiber Representative Volume Element to periodical cellular materials.

It was already specified that, by varying the basic geometries of the axial discretization or the element of the cross-section mesh, it is possible to obtain different complex geometries with a relative constructive simplicity. Moreover by choosing a more or less dense mesh, i.e. a greater o smaller number of elements of discretization, for both the axial direction and the cross-section, different levels of accuracy of the results can be achieved, with a higher or lower computational cost respectively.

Then, in this chapter, the effect of the shear locking phenomenon is also evaluated with three different approaches for its correction: the reduced integration, the selective integration and the mixed interpolation tensorial components approach. The shear locking is a numerical phenomenon who can occur if the thickness of the structure, which is subject to numerical study, tends to zero (Cinefra et al. [8];

Reddy [33]). As the thickness decreases in fact the shear stiffness tends to be infinite, causing consequently an overestimation. In order to correct this behavior, a lower number of Gauss points are used to define the discretization, with a lower resulting stiffness[6].

3.1 Static analysis of a cantilever beam

In this section, a cantilever beam is considered in order to evaluate the displacement under the action of different types of load.

The analysis will be conducted using the Finite Element Method and more specifically the Carrera Unified Formulation, varying the number and the type of the elements for the discretization along the axial direction of the beam, two different expansion classes for the displacement field on the cross-section and two different approaches for the shear locking phenomenon's correction.

Introduction to the problem Let us consider a cantilever beam, defined by one free tip and one clamped tip, under the action of a load $P_z = -50 N$ applied in one single point at the center of the free tip [6]. The reference system used is shown below (Fig. 3.1). The cross-section edge, h , is $0.2 m$ long and two slenderness ratios are considered: $L/h = 100, 10$. The material used is the aluminium, with a Young's modulus $E = 75 GPa$ and a Poisson's ratio $\nu = 0.33$.

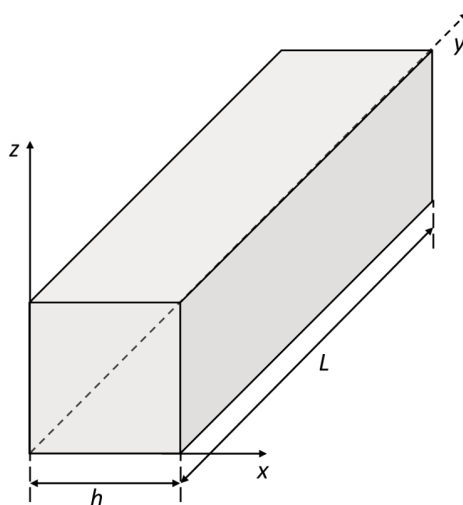


Figure 3.1: Reference system

3.1.1 Analysis via Taylor-like expansion

This first part of the analysis is done using a Taylor-like expansion, following what was said in the previous chapter of the thesis (2). The Taylor-like expansion can be seen as a generalisation of the model provided by Euler-Bernoulli [12] and Timoshenko [39] and it can be enhanced varying the order of the expansion, i.e. adding elements to the sum.

Obviously, as we can expect, increasing the order of the Taylor-like expansion, the computational cost will increase, even though this is not well-visible for simple problems in which the number of the elements is limited.

The objective of this example is to evaluate the displacement of the free-tip along the z direction, u_z , and to see how many elements are necessary to achieve convergence of results. Different degree of approximation can be obtained varying the following parameters:

- the *number* of the elements adopted for the description of the beam, from 5 to 40;
- the *elements' type*, who can be chosen between $B2$, $B3$ and $B4$;
- the order of the Taylor-like expansions of the displacement field, indicated as $N = 2, 3, 4$;

where the number of elements indicates the y-axis mesh's density and the type of elements specifies the number of nodes which defines each elements of the axial mesh. In particular, in the key-word, B stands for Beam-like element and the following number is the number of nodes which it contains (see Fig.3.2).

Finally, it is good to specify that two possibility will be considered to avoid the problem of the shear locking: the selective integration and the reduced integration. These two methods will be important especially in the cases of low-order expansion.

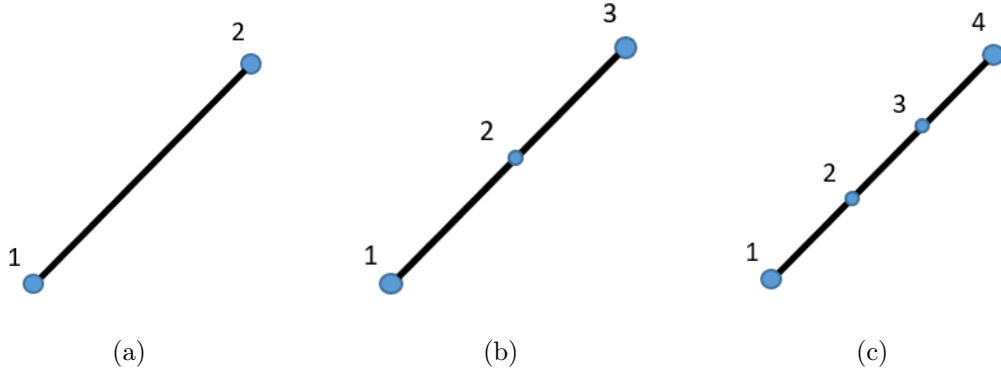


Figure 3.2: From left to right: $B2$, $B3$ and $B4$ element in their local reference system

Mesh refinement and convergence analysis The results obtained are summarized in the tables below (Tab. 3.1, 3.2 e 3.3), sorted on the theory order, where the last three columns report the values acquired via *Full integration*, *Selective integration* and *Reduced integration*.

In order to evaluate the accuracy of the results, it is possible to compare the results with the Euler-Bernoulli Beam Theory (EBBT), which allow us to calculate the displacement of the free tip for the cantilever beam using the formula

$$u_{zEBBT} = \frac{P_z L^3}{3EI} \quad (3.1)$$

where P_z is the load, L is the length of the beam, E is the Young modulus and I is the cross-section moment of inertia. It is good to remember that the Euler-Bernoulli theory have better results for beams with high slenderness ratios.

It can be noticed that, as the number of nodes for each element increases, less elements are required for the axial discretization, since there are globally still many points. Moreover, the effectiveness of the Reduced Integration to correct the shear locking phenomenon is proved: it is possible to obtain very accurate results even when the theory order, the number of elements and the type of the element are not sufficient for a good characterization. In this sense, the Selective Integration shows worse results while using the Full Integration it is not even possible to achieve usable values for the $B2$ elements. The numerical effect of the shear locking is mitigated considering a thicker beam ($L/h = 10$), in fact the value of the displacement is close to the comparison value.

Finally, it seems that the order of the Taylor-like expansion does not produce any effect since the simplicity of the problem is well described by the hypothesis of the Euler-Bernoulli theory, so it is useless to consider higher order terms.

Table 3.1: Theory order $N = 2$

<i>Type of elements</i>	<i>No. of elements</i>	<i>Full I.</i>	<i>Sel. I.</i>	<i>Red. I.</i>
$L/h = 100, u_z \times 10^2 m$				
$u_{z_{EBBT}} \times 10^2 = -1.331 m$				
B2	5	-0.009	-1.236	-1.320
	10	-0.035	-1.286	-1.329
	20	-0.128	-1.310	-1.331
	40	-0.397	-1.322	-1.332
B3	5	-1.284	-1.297	-1.333
	10	-1.311	-1.315	-1.332
	20	-1.323	-1.324	-1.332
	40	-1.328	-1.329	-1.332
B4	5	-1.311	-1.314	-1.332
	10	-1.323	-1.324	-1.332
	20	-1.328	-1.328	-1.332
	40	-1.331	-1.331	-1.332
$L/h = 10, u_z \times 10^5 m$				
$u_{z_{EBBT}} \times 10^5 = -1.336 m$				
B2	5	-0.521	-1.243	-1.317
	10	-0.950	-1.293	-1.326
	20	-1.204	-1.315	-1.328
	40	-1.294	-1.324	-1.329
B3	5	-1.301	-1.304	-1.329
	10	-1.320	-1.320	-1.329
	20	-1.326	-1.326	-1.329
	40	-1.328	-1.328	-1.329
B4	5	-1.319	-1.319	-1.329
	10	-1.326	-1.326	-1.329
	20	-1.328	-1.328	-1.329
	40	-1.329	-1.329	-1.329

Table 3.2: Theory order $N = 3$

<i>Type of elements</i>	<i>No. of elements</i>	<i>Full I.</i>	<i>Sel. I.</i>	<i>Red. I.</i>
$L/h = 100, u_z \times 10^2 m$				
$u_{z_{EBBT}} \times 10^2 = -1.331 m$				
B2	5	-0.009	-1.236	-1.320
	10	-0.035	-1.286	-1.330
	20	-0.128	-1.310	-1.332
	40	-0.397	-1.322	-1.332
B3	5	-1.284	-1.298	-1.333
	10	-1.311	-1.315	-1.332
	20	-1.323	-1.324	-1.332
	40	-1.329	-1.329	-1.332
B4	5	-1.311	-1.314	-1.333
	10	-1.323	-1.324	-1.332
	20	-1.328	-1.329	-1.332
	40	-1.331	-1.331	-1.332
$L/h = 10, u_z \times 10^5 m$				
$u_{z_{EBBT}} \times 10^5 = -1.336 m$				
B2	5	-0.521	-1.245	-1.322
	10	-0.951	-1.295	-1.328
	20	-1.206	-1.317	-1.330
	40	-1.296	-1.326	-1.330
B3	5	-1.303	-1.306	-1.331
	10	-1.322	-1.322	-1.331
	20	-1.328	-1.328	-1.331
	40	-1.330	-1.330	-1.331
B4	5	-1.321	-1.321	-1.331
	10	-1.328	-1.328	-1.331
	20	-1.330	-1.330	-1.331
	40	-1.331	-1.331	-1.331

Table 3.3: Theory order $N = 4$

<i>Type of elements</i>	<i>No. of elements</i>	<i>Full I.</i>	<i>Sel. I.</i>	<i>Red. I.</i>
$L/h = 100, u_z \times 10^2 m$				
$u_{z_{EBBT}} \times 10^2 = -1.331 m$				
B2	5	-0.009	-1.236	-1.320
	10	-0.035	-1.286	-1.329
	20	-0.128	-1.310	-1.331
	40	-0.397	-1.322	-1.332
B3	5	-1.284	-1.298	-1.333
	10	-1.311	-1.315	-1.332
	20	-1.323	-1.324	-1.332
	40	-1.328	-1.329	-1.332
B4	5	-1.311	-1.314	-1.333
	10	-1.323	-1.324	-1.332
	20	-1.328	-1.329	-1.332
	40	-1.331	-1.331	-1.332
$L/h = 10, u_z \times 10^5 m$				
$u_{z_{EBBT}} \times 10^5 = -1.336 m$				
B2	5	-0.521	-1.245	-1.323
	10	-0.951	-1.295	-1.329
	20	-1.206	-1.317	-1.332
	40	-1.297	-1.327	-1.332
B3	5	-1.303	-1.306	-1.333
	10	-1.322	-1.323	-1.332
	20	-1.329	-1.329	-1.332
	40	-1.332	-1.332	-1.332
B4	5	-1.321	-1.322	-1.333
	10	-1.329	-1.329	-1.332
	20	-1.331	-1.331	-1.332
	40	-1.332	-1.332	-1.332

3.1.2 Analysis via Lagrange polynomials

As said before, in addition to the Taylor-like expansion, it is possible to use the Lagrange polynomials in order to evaluate the displacement field along the cross-section. This kind of analysis involves a proper definition of the cross-section through L-elements: in fact, a set of Lagrange polynomials is defined by a given number of points which, in turn, depend on the type and number of elements used for the cross-section mesh. So in contrast to the Taylor-like, the order of the terms for the displacement field is defined by the density of the mesh.

In this analysis five different discretization are chosen: $1L4$, $2 \times 1L4$, $1 \times 2L4$, $2 \times 2L4$, $1L9$ (note that 2×1 indicates that there are 2 elements $L4$ along the x-axis and 1 element $L4$ along the z-axis), where the elements are represented in the figure below.

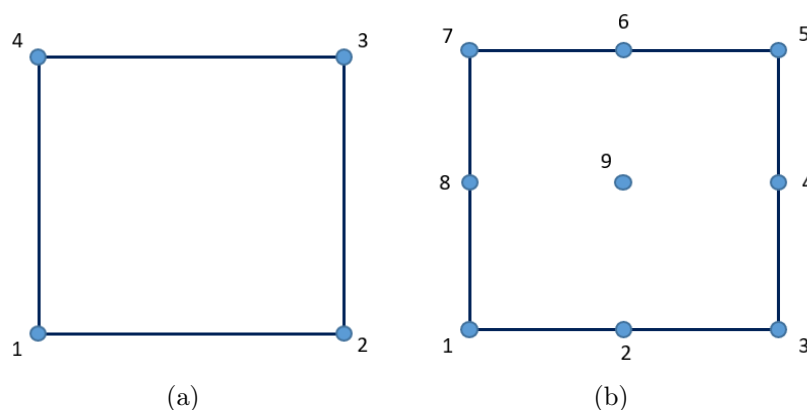


Figure 3.3: $L4$ and $L9$ element

Mesh refinement and convergence analysis The problem considered is the same proposed in the previous section: a cantilever beam, with a compact square cross-section ($h = 0.2 m$) having a length-to-thickness ratio equal to 100, made by the same material and under the same loading condition. The displacement of the free tip is evaluated [6]. Considering the previous analysis, the full integration is chosen, in order to define better the influence of the cross-section discretization, with $40B4$ elements along the y-axis.

The results are summarized in the following table and they show that, even considering the same number of points, if we see at the different result from $2 \times 2L4$

and from 1L9, the type of the element plays an important part into the accuracy of the analysis. In the table, *TE* means the usage of a Taylor-like expansion and *LE* of the Lagrange-like expansion.

Table 3.4: Effect of the L-type elements ($L/h = 100$), $u_{z_{EBBT}} \times 10^2 = -1.331 m$

<i>Model</i>	$u_z \times 10^2 m$
TE	
$N = 2$	-1.3306
$N = 3$	-1.3307
$N = 4$	-1.3307
LE	
1L4	-1.8656
$2 \times 1L4$	-1.1641
$1 \times 2L4$	-1.2340
$2 \times 2L4$	-1.2676
1L9	-1.3307

Then two different cantilever beams are considered with two square cross-section: the material, the load and the geometry of the section are unvaried, but we may take into account two length-to-thickness ratio, $L/h = 10, 100$.

The following tables show us the effect of the number of elements along the y-axis combined with different cross-section discretizations [5]. It has to be take in account that, for the y-along mesh, *B4* elements were used with the *selective integration*.

Table 3.5: Effect of the number of elements ($L/h = 100$)

<i>No. Elem.</i>	5	10	40
$u_z \times 10^2 m$			
$N = 2$	-1.314	-1.324	-1.331
1L4	-1.846	-1.858	-1.866
1L9	-1.314	-1.324	-1.331

Table 3.6: Effect of the number of elements ($L/h = 10$)

<i>No. Elem.</i>	5	10	40
	$u_z \times 10^5 m$		
$N = 2$	-1.319	-1.326	-1.329
$N = 3$	-1.321	-1.328	-1.331
$N = 4$	-1.322	-1.329	-1.332
1L4	-1.846	-1.853	-1.854
1L9	-1.319	-1.326	-1.329

Table 3.7: Effect of the number of L4 elements ($L/h = 100$)

<i>No. Elem.</i>	1L4	$2 \times 1L4$	$1 \times 2L4$	$2 \times 2L4$
	$u_z \times 10^2 m$			
5	-1.843	-1.154	-1.220	-1.252
10	-1.856	-1.160	-1.228	-1.261
40	-1.866	-1.164	-1.234	-1.268

It is immediate to understand that the L9 elements provides better results, while the L4 elements can be used only combined with many elements on the y-axis mesh or if in a large number themselves. Moreover, a lower computational cost has to be paid if the Lagrange polynomials are used instead of the Taylor-like expansion.

3.2 Static analysis of a hollow square cross-section

Let us now establish a hollow square cross-section beam, made with an isotropic material with $E = 75 GPa$, $\nu = 0.33$ and $\rho = 2700 kg/m^3$. The beam is clamped at both the edges and the cross-section geometry is defined by $L/h = 20$, $h/t = 10$ and $h = 1 m$.

It is possible to study the displacement of the middle-length section, varying the load applied, using first the Taylor-like expansion and then the Lagrange polynomials [6].

3.2.1 One punctual load

It is considered one punctual load applied to the coordinates $(0, L/2, -h/2)$. The displacement of the loaded point will be calculated using three different orders for the TE ($N = 4, 8, 11$) and three cross-section's discretization made up by $8L9, 9L9, 11L9$ LE elements (see fig.3.4).

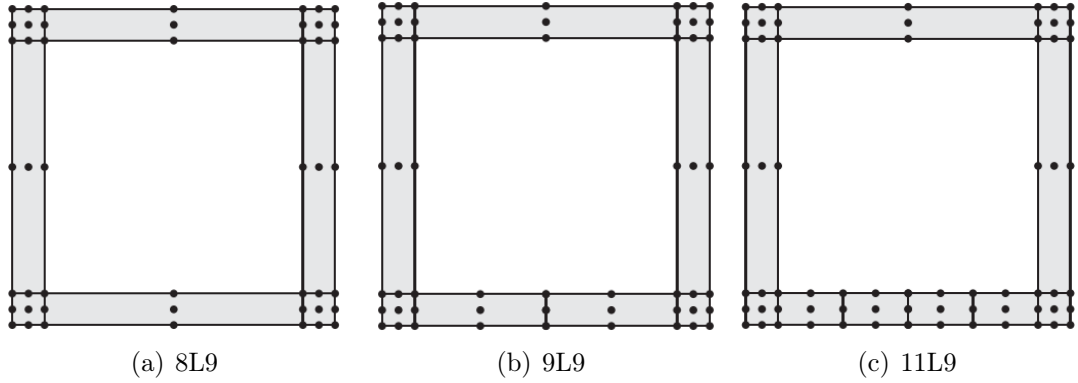


Figure 3.4: Cross-section discretization [6]

The results are showed in the tab.3.8

Table 3.8: Loaded point transverse displacement of the hollow square beam [6]

Theory	$u_z \times 10^8 m$	
	Results	Reference
	TE	
$N = 4$	1.199	1.209
$N = 8$	1.249	1.291
$N = 11$	1.262	1.309
	LE	
$8L9$	1.246	1.277
$9L9$	1.311	1.308
$11L9$	1.330	1.326

3.2.2 Two punctual loads

Two punctual loads are now applied to the same beam: $P_z = \pm 1 N$ applied at $(0, L/2, \mp h/2)$. It is possible to investigate the transverse displacement of the two

loaded point using the Taylor-like expansion and the Lagrange polynomials with the discretization (3.4(a)) and (3.4(c)).

Table 3.9: Two loaded point transverse displacement [6]

Theory	$u_{z_{top}} \times 10^9 m$		$u_{z_{bot}} \times 10^9 m$	
	Results	Reference	Results	Reference
TE				
$N = 4$	-0.180	-0.178	0.180	0.178
$N = 8$	-1.011	-1.046	1.011	1.046
$N = 11$	-1.221	-1.270	1.221	1.270
LE				
8L9	-0.939	-0.985	0.939	0.985
11L9	-0.927	-0.972	1.436	1.456

3.3 Static analysis of a C-shaped cross-section beam

The analysis of the differences between the results attained with Taylor expansions and Lagrange polynomials continues with the open cross-sections [6]. The first one considered is a C-shaped beam (see Fig.3.5) with the following parameters: $L/h = 20$, $h/t = 10$, $h = b_2 = 1 m$, $b_1 = b_2/2$. The material is, as usual, an isotropic metal.

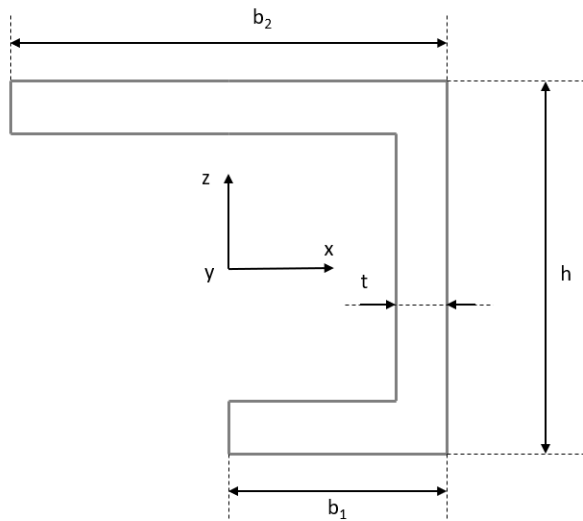


Figure 3.5: C-shaped cross-section

The displacement of the point at $(-b_2/2, L, 0.4)$ in the Tab.3.10 is obtained using the Taylor-like expansion with order $N = 4, 8, 11$ and the Lagrange polynomials with two $L9$ meshes, showed in Fig.3.6.

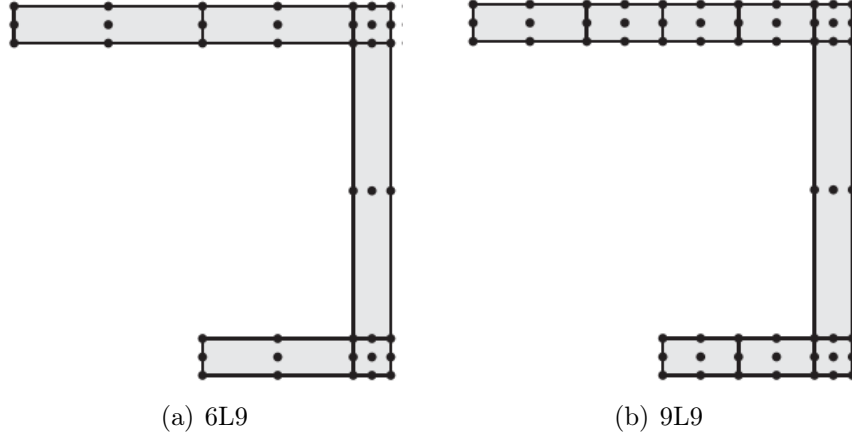


Figure 3.6: C-shaped cross-section discretization [6]

Table 3.10: Transverse displacement at $(-b_2/2, L, 0.4)$ [6]

Theory	$u_z \times 10^8 m$	
	Results	Reference
	TE	
$N = 4$	-0.237	-0.245
$N = 8$	-2.159	-2.161
$N = 11$	-2.561	-2.565
	LE	
$6L9$	-2.930	-2.930
$9L9$	-2.983	-2.982

3.3.1 Flexural-torsional load

A flexural-torsional load is considered as a second loading case. A point force ($P_z = -1 N$) is applied at $(b_1, L, -h/2)$ and, in this case, two length-to-thickness ratio are taken into account ($L/h = 20, 10$) with a $9L9$ cross-section discretization. The results consist of tension and displacement in particular points (Tab.3.11) while, following, the deformed shape of the beam is showed.

Table 3.11: Displacements and stresses of the C-shaped beam [6]

Length-to-thickness Ratio	Results	Reference	(x, y, z)
$L/h = 20$	$u_z \times 10^6 m$		
	-1.462	-1.462	$(-b_2/2, L, h/2)$
	$\sigma_{yy} \times 10^{-2} Pa$		
	4.052	3.976	$(b_1, L/10, h/2)$
	$\sigma_{xy} \times 10^{-2} Pa$		
	-2.040	-1.691	$(b_1, L, -h/2)$
$L/h = 10$	$u_z \times 10^7 m$		
	-2.272	-2.272	$(-b_2/2, L, h/2)$
	$\sigma_{yy} \times 10^{-2} Pa$		
	2.026	2.055	$(b_1, L/10, h/2)$
	$\sigma_{xy} \times 10^{-2} Pa$		
	-3.649	-3.837	$(b_1, L, -h/2)$
	$\sigma_{yz} \times 10^{-1} Pa$		
	-2.333	-2.348	$(0.4, L/10, 0)$
	-1.855	-1.863	$(0.4, L/10, 0)$

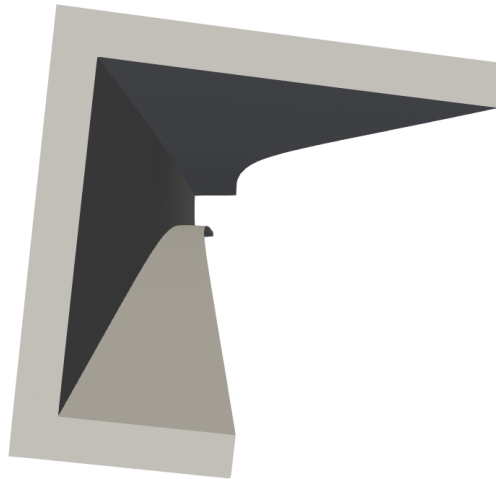


Figure 3.7: Free-tip of the C-shaped beam after the application of the load

3.4 Static analysis of a open hollow square cross-section beam

An open, square cross-section is now considered (Fig.3.8), while the cross section is defined by the ratios $L/h = 20$, $h/t = 10$, where $h = 1\text{ m}$. The material is isotropic, characterized by a Young modulus $E = 75\text{ GPa}$, a Poisson ratio $\nu = 0.33$ and density $\rho = 2700\text{ kg/m}^3$, the structure is clamped at both the edges with two opposite unit loads ($\pm P_x$) applied at $(0, L, -0.45)$ [6].

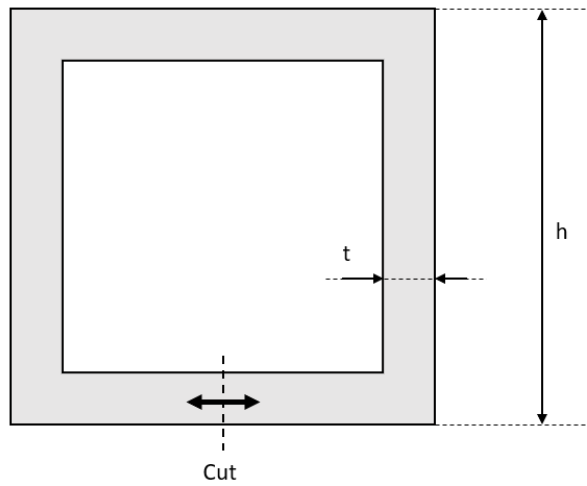


Figure 3.8: Open, hollow square cross-section

Three different $L9$ discretization are adopted (see Fig.3.9) in order to calculate the x-axis displacement of the point $(0, L, -h/2)$.

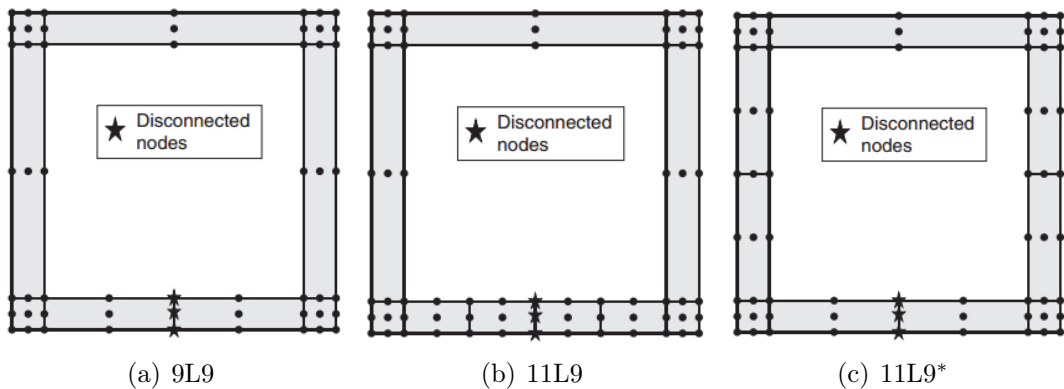


Figure 3.9: Open square cross-section discretization [6]

Results The displacement is indicated in Tab.3.12. It is important to specify that this kind of problem cannot be analyzed by the Taylor-like expansion, since the application of the two opposite force at the same point would imply null displacement.

Table 3.12: Horizontal displacement at $(0, L, -h/2)$ [6]

Elements	$u_x \times 10^8 m$	
	Results	Reference
9L9	4.897	4.884
11L9	4.906	4.888
11L9*	5.135	5.116

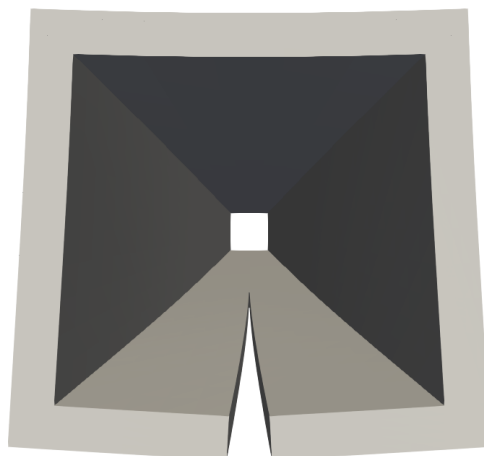


Figure 3.10: Free-tip of the open square cross-section under the load's application

3.5 Static analysis with solid-like geometrical BCs

Differently from the cases in which the geometrical boundary conditions are imposed over the entire cross-section, it is possible that the problem requires more localized BCs. The next examples place themselves in this argument.

3.5.1 Compact rectangular beam

The first example take into account is a compact rectangular beam, clamped at the lateral edges (see Fig.3.11), with the following geometrical characteristics: $L/h =$

100, $b/h = 10$, $h = 0.01 m$. A set of 21 unitary point loads is applied over the surface ($z = h/2$) along the mid-span cross-section, with constant steps on x [6]. It is possible to evaluate the vertical displacement u_z of the point at the middle of the beam $(0, L/2, 0)$ using the Lagrange polynomials for the displacement field with a mesh, over the cross-section, of $10L9$ elements (Tab.3.13).

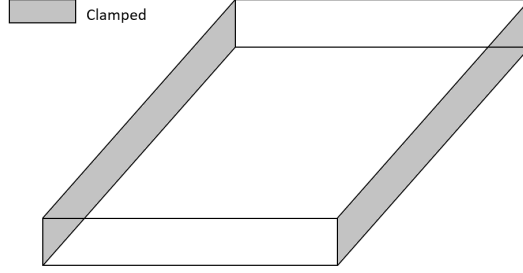


Figure 3.11: Compact rectangular beam, clamped at the edges

Table 3.13: Vertical displacement at $(0, L/2, 0)$ [6]

Elements	$u_z \times 10^7 m$	
	Results	Reference
10L9	-1.102	-1.110

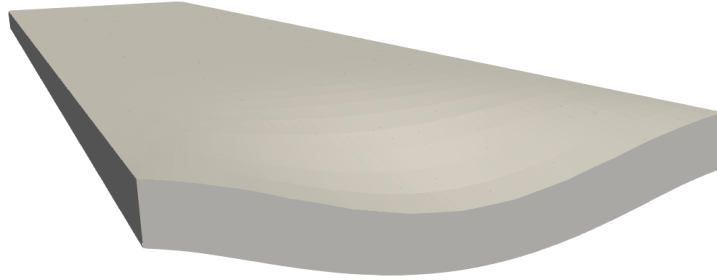


Figure 3.12: Deformed mid-span cross-section of the compact beam

3.5.2 Compact rectangular curved beam

Now let us consider a circular arch cross-section beam clamped at the lateral edges (Fig.3.13) [6]. The geometry is defined by the length $L = 2m$, the outer radius $r_1 = 1m$, the inner radius $r_2 = 0.9m$ and the angle of the arch $\theta = \pi/4 rad$, while

three unitary point load are applied, in the radial direction, on the bottom surface at $y = 0, L/2, L$.

The mesh over the cross-section is made by $12L9$ elements, organized as in the Fig.3.14 and it is possible to calculate the vertical displacement of the point on the top surface, along the mid-span cross-section, in correspondence of the loaded point ($y = L/2, \theta = \theta/2$) (see Tab.3.14).

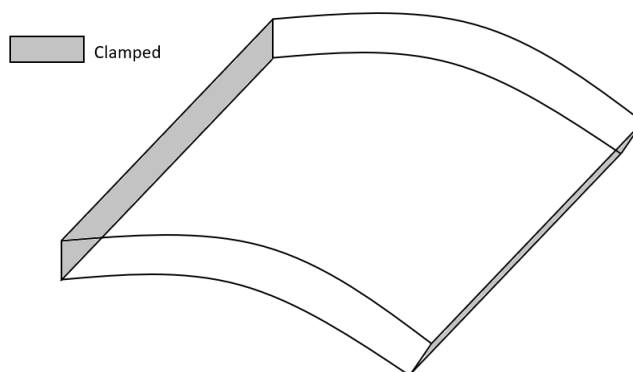


Figure 3.13: Circular arch cross-section rectangular beam, clamped at the edges

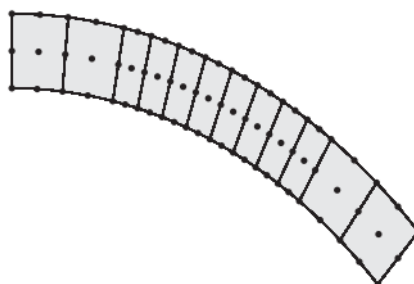


Figure 3.14: L9 mesh for circular arch cross-section rectangular beam [6]

Table 3.14: Vertical displacement of the beam's top surface ($y = L/2, \theta = \theta/2$) [6]

Elements	$u_z \times 10^{10} m$	
	Results	Reference
12L9	4.703	4.809

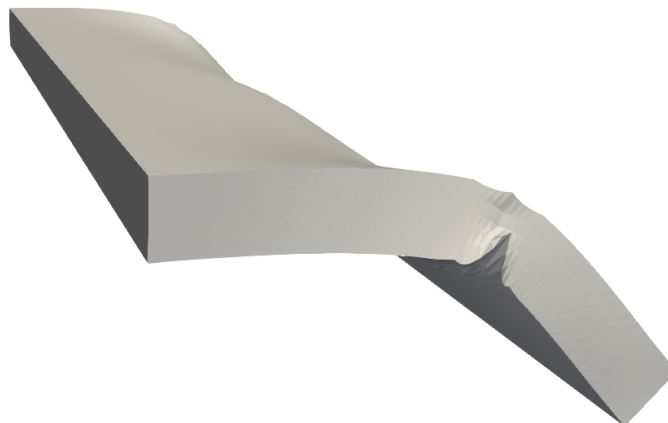


Figure 3.15: Deformed shape of the curved beam

3.5.3 C-shaped cross-section beam

It is now taken into consideration the previous c-shaped cross-section beam (see Fig.3.5) with the same geometrical parameters [6]. The boundary condition proposed is that one showed in the following figure (Fig.3.16), with only the bottom flanges clamped, while the $L9$ mesh chosen in made by 13 elements (Fig.3.17).

Two point load $P_z = -1 N$ are applied at $(0, 0, 0.4)$ and $(0, L, 0.4)$: it is possible to evaluate the vertical displacement of the loading point using the Lagrange polynomials (Tab.3.15).

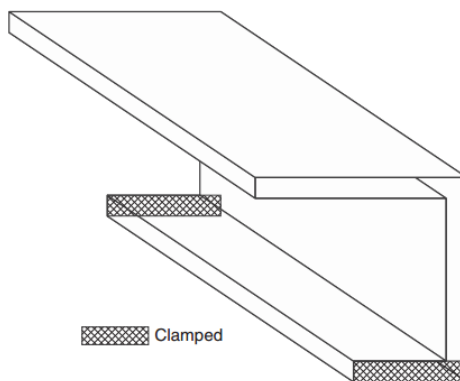


Figure 3.16: C-shaped cross-section beam, bottom flanges clamped [6]

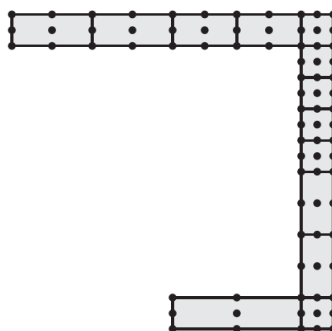


Figure 3.17: L9 mesh for c-shaped cross-section beam [6]

Table 3.15: Vertical displacement of the loading point (0, 0, 0.4) [6]

Elements	$u_z \times 10^{10} m$	
	Results	Reference
13L9	-3.690	-3.662

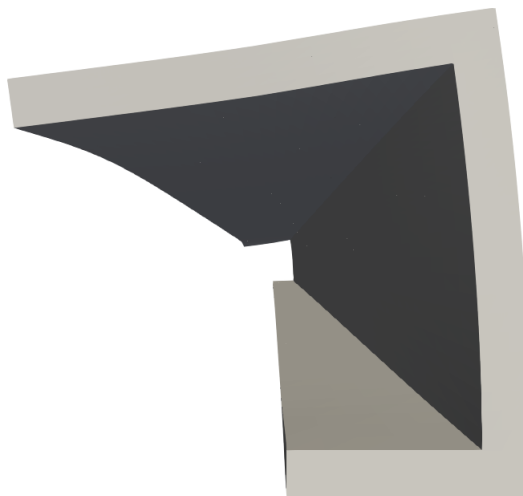


Figure 3.18: C-shaped cross-section beam with bottom flanges clamped after deformation

3.6 Static analysis of a symmetric laminated beam

A three-layer symmetric beam is considered [28] (see Fig.3.19). The dimensions of the beam are known: the length $L = 2m$, the width $b = 0.2m$ and the height $h = 0.1m$. The beam is divided into three sub-domains, one per layer, and everyone of their is made of an orthotropic material with the following properties:

$E_L = 25.0 \text{ GPa}$, $E_T = E_Z = 1.0 \text{ GPa}$, $\nu_{LT} = \nu_{LZ} = \nu_{TZ} = 0.25$, $G_{LT} = 0.5 \text{ GPa}$ and $G_{TZ} = G_{LZ} = 0.2 \text{ GPa}$.

As we said before, a symmetric $[0^\circ, 90^\circ, 0^\circ]$ cross-ply lamination is applied. The beam is clamped at $y = 0$ while it is loaded at $y = L$ with four point load $P_z = -25 \text{ N}$ at $(0, L, \pm h/2)$ and $(b, L, \pm h/2)$.

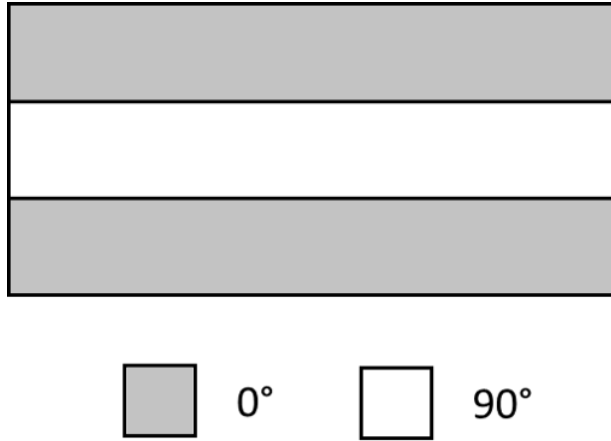


Figure 3.19: Three layered symmetric beam

Results Discretizing the cross-section in $3L9$ elements, it is possible to investigate the displacements, the normal stresses and the shear stresses at different points of the beam (Tab.3.16) and, using paraview, the variation of σ_{yy} and σ_{yz} over the cross-section height is also obtainable (see Fig.3.20).

Table 3.16: Displacements and stresses on the beam [28]

Theory	$u_z \times 10^3 \text{ m}$ $(0, L, h/2)$		$\sigma_{yy} \times 10^{-3} \text{ Pa}$ $(0, L/2, h/2)$		$\sigma_{yz} \times 10^{-3} \text{ Pa}$ $(0, L/2, 0)$	
LE	Res.	Ref.	Res.	Ref.	Res.	Ref.
$3L9$	-0.73	-0.72	311.01	311.07	-6.99	-6.92
TE	Res.		Res.		Res.	
$N = 6$	-0.74		310.86		-7.25	

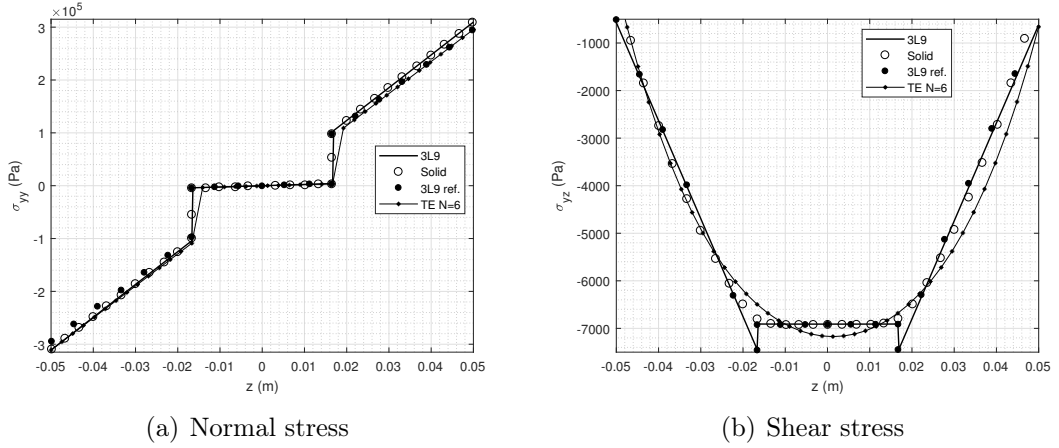


Figure 3.20: Variation of normal and shear stresses along the z-axis, Solid and 3L9 ref. solution are referred to [28]

3.7 Static analysis of a eight-layer composite beam

For this test, a cantilever eight-layer composite beam is taken into account [28]. The geometry of the structure is shown in the Fig.3.21, where the materials have the following characteristics:

1. $E_L = 30 \text{ GPa}$, $E_T = E_Z = 1 \text{ GPa}$, $G = 0.5 \text{ GPa}$ and $\nu = 0.25$;
2. $E_L = 5 \text{ GPa}$, $E_T = E_Z = 1 \text{ GPa}$, $G = 0.5 \text{ GPa}$ and $\nu = 0.25$.

Four equal loads are applied at the corners of the beam's cross-section tip, directed as the z-axis with a value of -0.05 N . The vertical displacement and the normal stress are investigated into two different points (Tab.3.17) and the evolution of normal and shear stresses, along the mid-length cross-section, are plotted versus the beam's height (Fig.3.22).

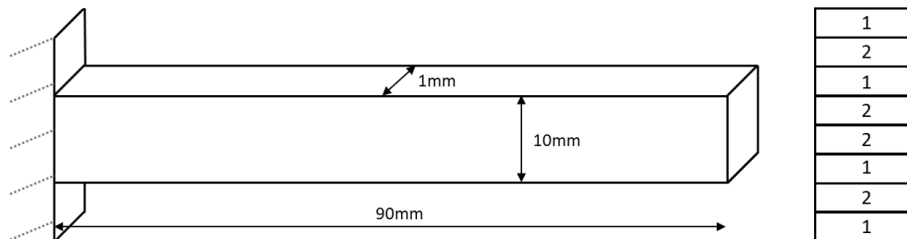
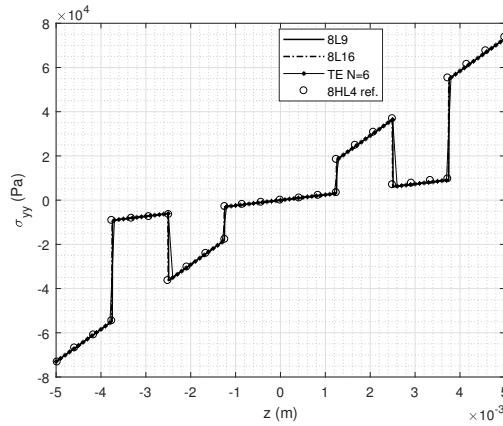


Figure 3.21: Eight layered composite beam

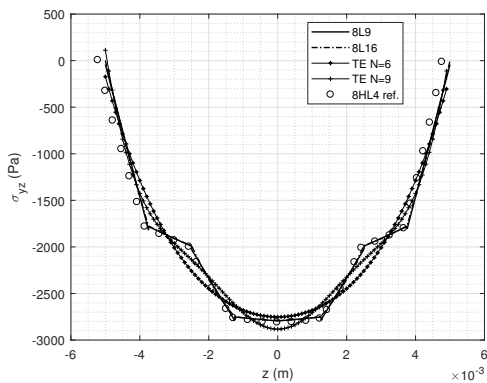
Results As we said before, stresses and displacements are investigated using the CUF, describing the displacement field with the Taylor-like expansion and the Lagrange polynomials, in order to obtain increasingly accurate results.

Table 3.17: Displacements and stresses on the eight-layer beam. The reference value is in the brackets [28]

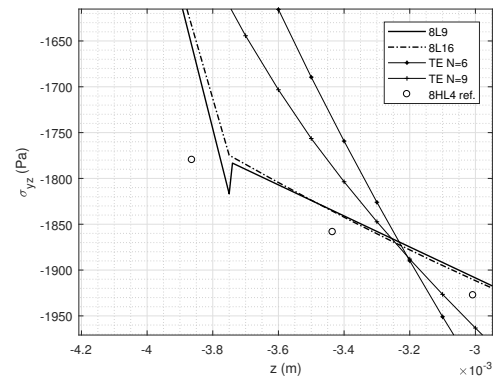
Model	$u_z \times 10^6 m$ ($a/2, L, 0$)	$\sigma_{yy} \times 10^2 Pa$ ($a/2, L/2, -h/2$)
<i>LE</i>		
8L9	-3.029 [-3.029]	-730 [-730]
8L16	-3.029	-730
<i>TE</i>		
$N = 6$	-3.027	-730
$N = 9$	-3.031	-730



(a) Normal stress



(b) Shear stress



(c) Detail of the shear stress' curve

Figure 3.22: Variation of normal and shear stresses along the z-axis, 8HL4 ref. solution is referred to [28]

3.8 Single and double cell static analysis

For the following analysis a single cell and then a double cell unit is considered, in order to perform the analysis of basic units who can be repeated all along the space to simulate structure with a high level of complexity [3]. The cross-section model for the single cell model is described in the Fig.3.23 where the cell is square and $b = 0.1 \text{ mm}$, $d = 0.08 \text{ mm}$, $L/b = 10$. Isotropic material is then chosen for this assessment:

1. fiber is defined by $E = 202.038 \text{ GPa}$ and $\nu = 0.2128$;
2. matrix has $E = 3.252 \text{ GPa}$ and $\nu = 0.355$.

while the structure is clamped at $y = 0$ and loaded at $(b/2, L, 0)$ with a vertical load $F_Z = -0.1 \text{ N}$. Results were obtained by means of TE and LE models, using a $10B4$ mesh with a cross-section discretization defined using $20L9$ elements, as shown in Fig.3.23.

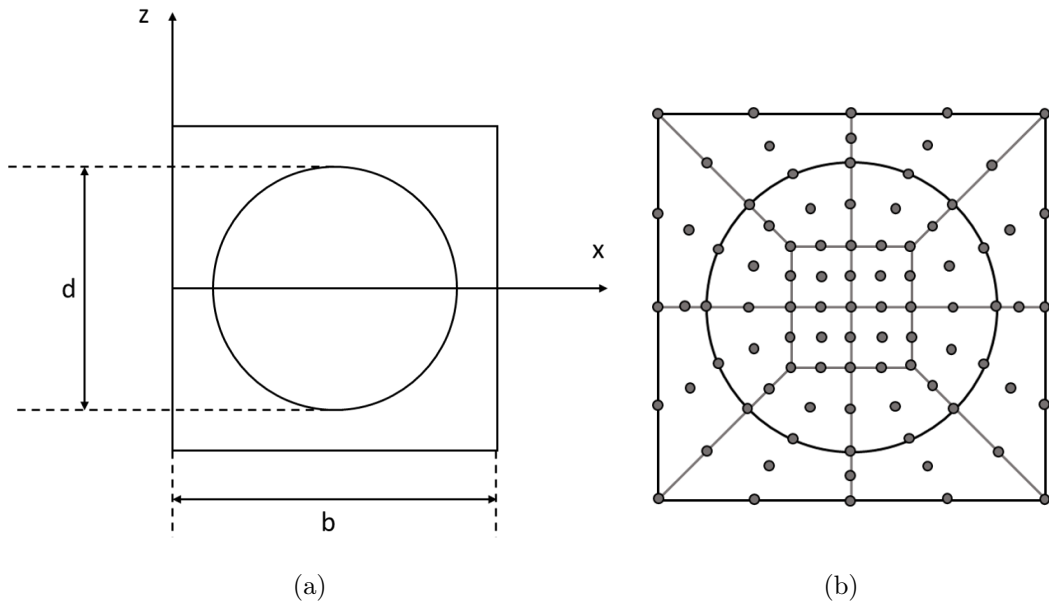


Figure 3.23: Single fiber-matrix cross-section and relevant discretization

The double cell model is instead obtained just repeating the single cell model, shifted over the x -axis, and maintaining the same cross-section discretization and materials (Fig.3.24). It is necessary to specify that $a = 2b$.

The structure is clamped at $y = 0$ and loaded with two vertical point load, applied at Point A ($a/4, L, b/2$) and Point B ($3a/4, L, b/2$).

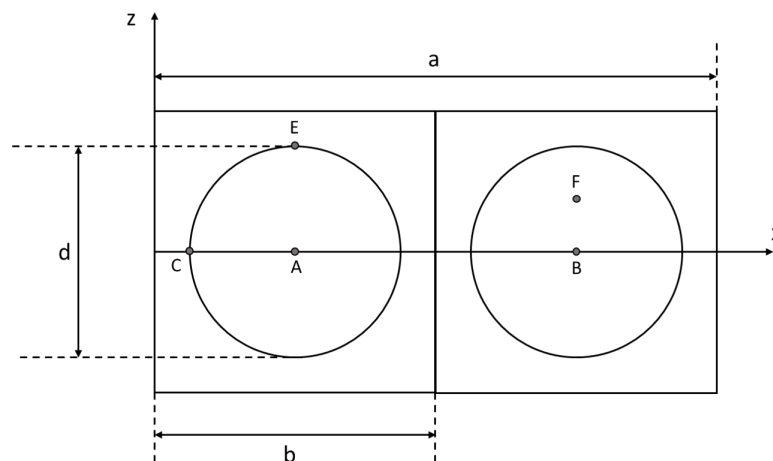


Figure 3.24: Double cell cross-section

Results for single cell model The displacement of the loading point is analyzed, varying the model of the cross-section displacement field (Tab.3.18).

Table 3.18: Vertical displacement of the loading point ($b/2, L, 0$) [mm] [3]

Model	$u_z \times 10^5 \text{ mm}$	
	Results	Reference
	<i>LE</i>	
20L9	-7.825	-7.933
	<i>TE</i>	
$N = 1$	-7.844	-7.835
$N = 2$	-7.783	-7.774
$N = 3$	-7.786	-7.777
$N = 4$	-7.803	-7.794
$N = 5$	-7.804	-7.795
$N = 6$	-7.809	-7.800
$N = 7$	-7.809	-7.800
$N = 8$	-7.813	-7.804

Results for double cell model First, the displacement of the point A is analyzed, using the LE and TE model (Tab.3.19). Then, the normal and the shear stress

is evaluated in Points E ($a/4, L/2, 0.04$), F ($3a/4, L/2, 0.03$) and C ($0.01, L/2, 0$) (Tab.3.20), where the Solid solution is obtained from Abaqus.

Table 3.19: Vertical displacement of the loading point ($a/4, L, 0$) [mm] [3]

Model	$u_z \times 10^5 mm$	
	Results	Reference
<i>LE</i>		
20L9	-3.646	-3.958
<i>TE</i>		
$N = 1$	-3.922	-3.917
$N = 2$	-3.871	-3.868
$N = 3$	-3.872	-3.869
$N = 4$	-3.881	-3.879
$N = 5$	-3.881	-3.879
$N = 6$	-3.887	-3.885
$N = 7$	-3.887	-3.885
$N = 8$	-3.889	-3.887

Table 3.20: Normal and shear stresses on the double cell, the reference values are in the brackets [3]

Model	$\sigma_{yy} \times 10^{-2} MPa$		$\sigma_{yy} \times 10^{-2} MPa$		$\sigma_{yz} \times 10^{-1} MPa$	
	Point E		Point F		Point C	
<i>LE</i>						
40L9	4.657	(4.647)	3.508	(3.522)	-1.321	(-1.584)
<i>TE</i>						
$N = 1$	4.680	(4.734)	3.555	(3.551)	-0.981	(-0.981)
$N = 2$	4.627	(4.679)	3.514	(3.509)	-1.592	(-1.591)
$N = 3$	4.627	(4.679)	3.514	(3.509)	-1.773	(-1.771)
$N = 4$	4.576	(4.625)	3.517	(3.513)	-1.760	(-1.759)
$N = 5$	4.576	(4.625)	3.517	(3.513)	-1.656	(-1.655)
$N = 6$	4.597	(4.641)	3.557	(3.552)	-1.671	(-1.670)
$N = 7$	4.597	(4.641)	3.557	(3.552)	-1.592	(-1.590)
$N = 8$	4.619	(4.664)	3.561	(3.556)	-1.584	(-1.583)
<i>SOLID</i> [3]						
		(4.744)		(3.546)		(-1.519)

3.9 Static Analysis of a cross-ply beam with different models

Let us consider a cross-ply beam [4], made by three layers at $[0^\circ, 90^\circ, 0^\circ]$, with the following geometry: length $L = 40 \text{ mm}$, width $b = 0.8 \text{ mm}$ and height $h = 0.6 \text{ mm}$. The fibers considered have a diameter of 0.016 mm each one and every different component is studied with its mechanical characteristic:

1. Fiber is considered orthotropic with $E_1 = 202.038 \text{ GPa}$, $E_2 = E_3 = 12.134 \text{ GPa}$, $G_{12} = G_{13} = 8.358 \text{ GPa}$, $G_{23} = 47.756 \text{ GPa}$, $\nu_{12} = \nu_{13} = 0.2128$ and $\nu_{23} = 0.2704$;
2. Matrix is an isotropic material with $E = 3.252 \text{ GPa}$ and $\nu = 0.355$;
3. Layer's characteristics are calculated by means of the Rules of Mixture, from which results $E_1 = 103.173 \text{ GPa}$, $E_2 = E_3 = 5.145 \text{ GPa}$, $G_{12} = G_{13} = 2.107 \text{ GPa}$, $G_{23} = 2.353 \text{ GPa}$, $\nu_{12} = \nu_{13} = 0.2835$ and $\nu_{23} = 0.3124$,

where 1 is the longitudinal direction, 2 is the orthogonal direction and 3 is the transverse one.

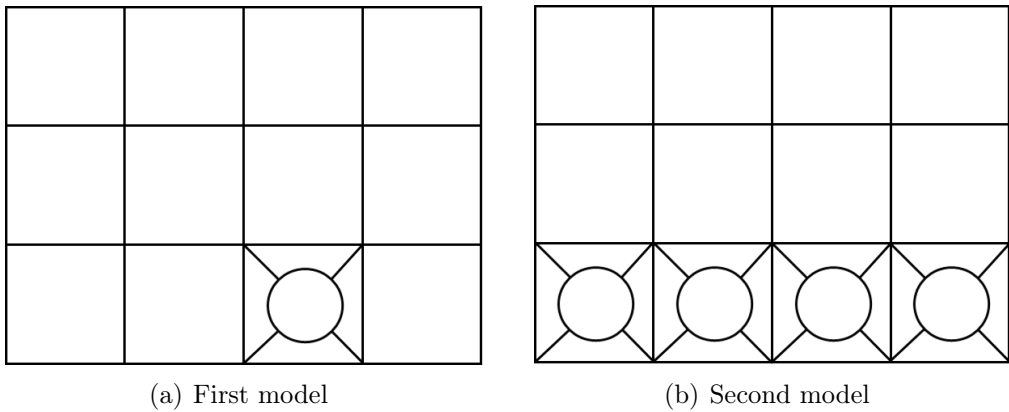


Figure 3.25: Two models for the cross-section of the cross-ply beam

Two different models are taken into account for the structural analysis: the first model is made by three layers and just one single fiber-matrix cell is inserted in the bottom layer; instead, the second one is obtained with four cell in bottom e top

layer, while the middle layer is constituted by the orthotropic material indicated before (Fig.3.25).

The cross-ply beam is considered cantilevered, with one edge clamped and the other edge loaded with a vertical point load $F_Z = -1 N$ at $(b/2, L, 0)$.

Results The displacement and the stresses are calculated in different point over the cross-section and they are displayed in Tab.3.21. In particular, the vertical displacement is calculated in the center of the cross-section at $(b/2, L, 0)$, while σ_{yy} and σ_{yz} are evaluated at the center point of the third cell of the bottom layer, which means at $(5b/8, L/2, -0.2)$.

Table 3.21: Displacement and stresses on the cross-ply beam, the reference values are in the brackets [4]. σ_{yz} is obtained using the Mixed Interpolation Tensorial Components approach for the model 1 and the Selective Integration for the model 2.

Theory	Order	$u_z \times 10^2 mm$		$\sigma_{yy} \times 10^{-2} MPa$		$\sigma_{yz} \times 10^{-1} MPa$	
		$(b/2, L, 0)$		$(5b/8, L/2, -0.2)$		$(5b/8, L/2, -0.2)$	
Model 1							
LE	30L9	-1.447	(-1.498)	-5.467	(-5.659)	-2.954	(-2.381)
TE	$N = 5$	-1446	(-1.498)	-5.457	(-5.659)	-0.378	(-2.381)
Model 2							
LE	164L9	-1.089	(-1.548)	-5.538	(-5.849)	-1.391	(-2.169)
TE	$N = 5$	-1.435	(-1.548)	-5.538	(-5.849)	-0.764	(-2.169)

3.10 Modal analysis of a cantilever beam

The utilisation of the Carrera Unified Formulation is possible even in case of Modal Analysis of simple and complex geometries. In particular, the natural frequencies of some structures can be evaluated under different constraint conditions, materials or cross-sections.

In this section, two different geometries for the cross-section are analyzed, both cantilevered, with one edge clamped and the other one free to move. The study will be performed using the Taylor-like expansion and it has, as objective, the evaluation

of the effect of the theory order on the accuracy of the results.

3.10.1 Cantilevered compact section

Let us consider a cantilevered beam with a rectangular cross-section [29]. The geometry of the section is shown in Fig. 3.26, where $b = 0.03\text{ m}$ and $h = 0.1\text{ m}$, with a length-to-thickness ratio $L/h = 100$.

The material used is steel, with $E = 210\text{ GPa}$, $\nu = 0.33$ and $\rho = 7900\text{ kg/m}^3$, and the discretization along y -axis is done with 40B4 elements.

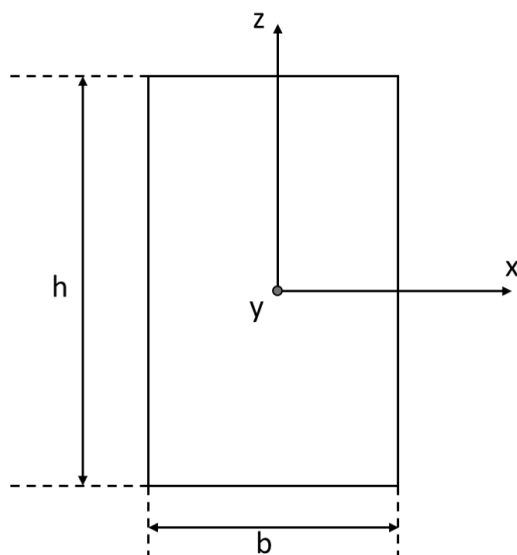


Figure 3.26: Rectangular cross-section

It is possible to calculate analytically the natural frequencies by means of the Euler-Bernoulli model (EBBM)

$$\omega_n = \frac{1}{2\pi} \sqrt{\frac{EI}{\rho A}} (\beta_n)^2 \quad (3.2)$$

and then compare these results with those ones obtained via FEM and Taylor-like expansion to describe the displacement field.

Results In the table below there are the first ten natural frequencies

Table 3.22: Natural frequencies (Hz) for $L/h = 100$, via Taylor-like expansion

Frequencies	Analytical Solution	<i>TBM</i>	$N = 1$	$N = 2$	$N = 3$	$N = 4$
f_1	0.250	0.250	0.250	0.250	0.250	0.250
f_2	0.833	0.833	0.833	0.834	0.834	0.834
f_3	1.566	1.566	1.566	1.569	1.569	1.569
f_4	4.384	4.384	4.384	4.391	4.391	4.391
f_5	5.219	5.217	5.217	5.223	5.223	5.223
f_6	8.592	8.590	8.590	8.604	8.603	8.603
f_7	14.203	14.198	14.198	14.221	14.220	14.220
f_8	14.615	14.597	14.598	14.616	14.613	14.613
f_9	21.216	21.207	21.207	21.242	21.240	21.240
f_{10}	28.639	28.577	28.577	28.613	28.604	28.604

In the end the error is obtained using the formula

$$\Delta_{\%} = \left| \frac{\omega_{an} - \omega}{\omega_{an}} \right| \times 100 \quad (3.3)$$

Table 3.23: Percentage error with reference to the analytical solution

Frequencies	Analytical Solution	<i>TBM</i>	$N = 1$	$N = 2$	$N = 3$	$N = 4$
f_1	0.250	0	0	0	0	0
f_2	0.833	0	0	0.12	0.12	0.12
f_3	1.566	0	0	0.19	0.19	0.19
f_4	4.384	0	0	0.16	0.16	0.16
f_5	5.219	0.04	0.04	0.08	0.08	0.08
f_6	8.592	0.02	0.02	0.14	0.13	0.13
f_7	14.203	0.04	0.04	0.13	0.12	0.12
f_8	14.615	0.12	0.12	0.01	0.01	0.01
f_9	21.216	0.04	0.04	0.12	0.10	0.10
f_{10}	28.639	0.22	0.22	0.09	0.12	0.12

3.10.2 Cantilevered thin-walled structure

It is now considered a thin-walled beam with a semi-circular cross section, as shown in Fig.3.27 [29]. The geometrical dimensions are given as following: the radius $r = 0.0245\text{ m}$, the thickness $t = 0.004\text{ m}$ and the length $L = 0.82\text{ m}$.

The material is assumed to be aluminium with $E = 68.9\text{ GPa}$, $\nu = 0.3$ and $\rho = 2700\text{ kg/m}^3$ and the boundary condition chosen is one edge clamped and one edge free (cantilever beam). In the end a mesh of 20B4 elements is setted with a cross-section discretization made by 10L9 elements.

The first three coupled and the first three uncoupled frequencies are in Tab.3.24.

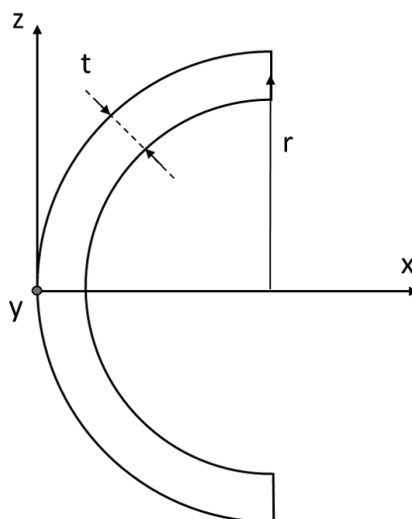


Figure 3.27: Semi-circular cross-section cantilever beam

Table 3.24: First three coupled and uncoupled natural frequencies with for a semi-circular cross-section cantilever beam [29]

Frequence	EBBM		N=2		N=4	
	Results	Reference	Results	Reference	Results	Reference
<i>Uncoupled frequencies (Hz)</i>						
1	31.94	31.86	32.04	31.98	31.98	31.00
2	199.95	199.57	199.47	199.07	198.81	193.28
3	558.81	557.77	552.62	551.50	549.54	532.99
<i>Coupled frequencies (Hz)</i>						
1	72.99	72.84	70.77	72.81	68.68	67.33
2	454.64	453.71	446.09	445.18	349.70	357.81
3	1260.55	1257.94	1204.68	1202.23	593.33	593.76

3.11 Micromechanical analysis

The aim of this section is the micromechanical analysis of composites structures. This target can be achieved using two different processes: homogenization and de-homogenization that, respectively, returns the effective material properties of a composite or the stiffness matrix and the tension field in a Representative Volume Element (RVE) using the Carrera Unified Formulation.

3.11.1 Fiber reinforced composites

The effective moduli of uni-directional fiber reinforced composites are examined in this section [18].

Two different cases are analyzed, both of them modeled with a square pack RVE, as shown in Fig.3.28: the first one is an Aluminium matrix in which Boron fibers are immersed, with a fiber volume fraction of 47%; the second case is a composite made by Epoxy matrix and Graphite reinforce (60%).

The properties of the two materials are the following:

- Boron fiber - $E_{11} = E_{22} = 379.3 \text{ GPa}$, $G_{12} = 172.41 \text{ GPa}$, $\nu_{12} = \nu_{23} = 0.1$;
- Graphite fiber - $E_{11} = 235.0 \text{ GPa}$, $E_{22} = 14.0 \text{ GPa}$, $G_{12} = 28 \text{ GPa}$, $\nu_{12} = 0.2$, $\nu_{23} = 0.25$;
- Aluminium matrix - $E_{11} = E_{22} = 68.3 \text{ GPa}$, $G_{12} = 26.3 \text{ GPa}$, $\nu_{12} = \nu_{23} = 0.3$;
- Epoxy matrix - $E_{11} = E_{22} = 4.8 \text{ GPa}$, $G_{12} = 1.8 \text{ GPa}$, $\nu_{12} = \nu_{23} = 0.34$;

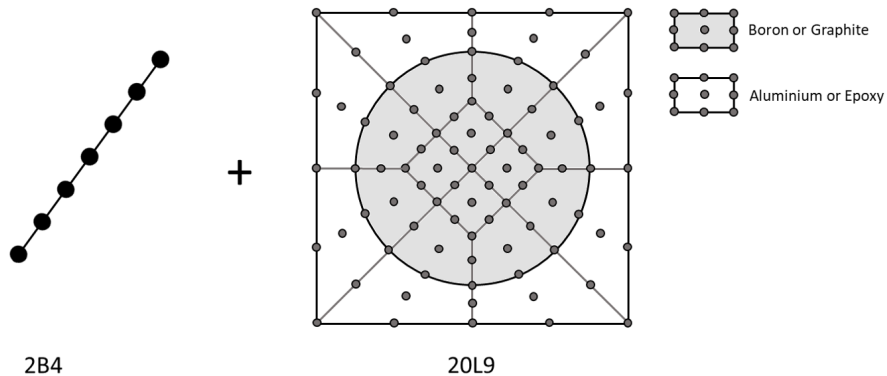


Figure 3.28: Component-wise discretization of the square pack RVE

Results The Component-wise discretization is made using $20L9$ elements for the cross-section and $2B4$ elements for the beam. The displacement field along the cross-section is obtained using the Lagrange polynomials and the results are compared with those written in [18] (Tab.3.25).

Table 3.25: Effective moduli of the materials [18]

	E_{11} (GPa)	E_{22} (GPa)	G_{12} (GPa)	G_{23} (GPa)	ν_{12} (–)	ν_{23} (–)
Boron/Aluminium Composite, $VF = 40\%$						
Result	215.2	144.2	54.4	45.9	0.195	0.254
Reference	215.2	144.3	54.4	46.0	0.195	0.253
Graphite/Epoxy Composite, $VF = 67\%$						
Result	142.8	9.6	6.10	4.47	0.252	0.349
Reference	142.8	9.6	6.10	3.13	0.252	0.349

3.11.2 Void filled composite

In the following example, it is analyzed the local and global behaviour of a void-filled composite [18].

As shown in Fig.3.29, two kinds of geometry are investigated, one with a circular and the other with a square inclusion. The beam, made of copper, with the Young modulus $E = 127 GPa$ and Poisson ratio $\nu = 0.34$, is discretized with $2B4$ elements while the cross-section with $40L9$ elements.

The result of the analysis is the modified Young modulus in the longitudinal direction E_{22} : for this purpose, four different volume fractions are considered: 0.0204, 0.1837, 0.5102, 0.7511 (Tab.3.26).

Results The Young modulus was evaluated, referred to those obtained in [18] while, in Fig.3.30, the von-Mises stress field, σ_{vm} , is depicted when a transverse tensile strain ϵ_{11} of 0.001 is applied.

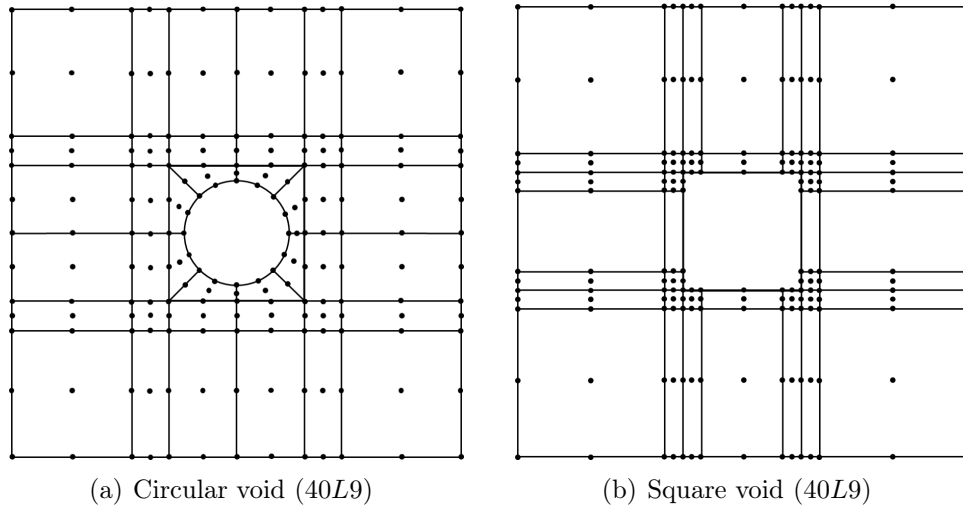


Figure 3.29: Discretization of the two types of inclusion

Table 3.26: Transverse Young modulus E_{22} (GPa) of void-filled composite with different void volume fraction [18]

	Void volume fraction			
	0.0204	0.1837	0.5102	0.7511
Circular void				
Result	120.58	83.03	39.59	12.26
Reference	120.36	82.27	39.57	10.32
Square void				
Result	120.47	81.90	39.86	18.28
Reference	120.22	82.02	39.85	18.28

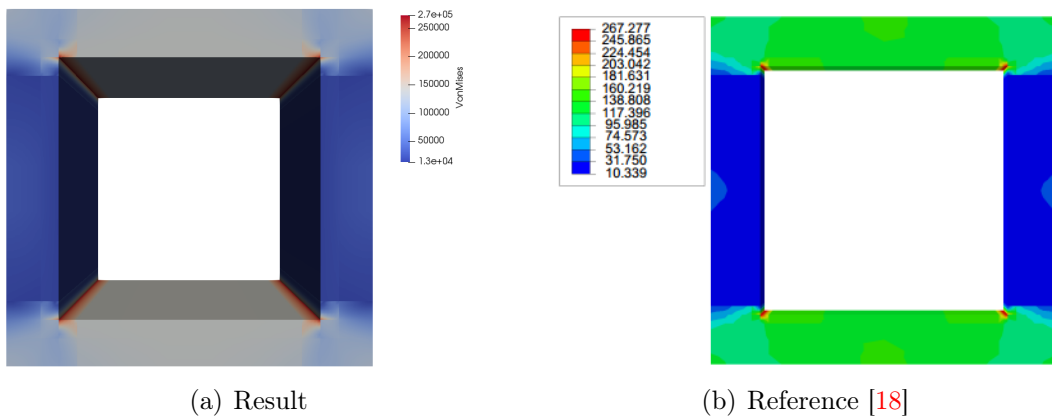


Figure 3.30: von-Mises stress contours σ_{vm} [MPa] over the cross-section of the RVE with a void volume fraction of 0.5102

The analysis exposed so far has to be seen as an introduction to the real work on the microstructure of a composite material. The same approach used in these example will be extended to the micromechanical analysis through homogenization and de-homogenization processes in order to figure out the strength of a particular Repeating Unit Cell. Then, after a proper statistical study on the fiber distribution for each cell, it will be possible to correlate the strength and the stiffness achieved to the randomness' degree characterizing the reinforcement phase.

Bearing this goal in mind, it is now possible to discuss the statistical analysis of the repeating unit cells showed in chapter 1.

Chapter 4

Statistical analysis of the RUCs: description of fibers' arrangement and degree of randomness

The complete characterisation of a repeating unit cell, of whom we want to model the micromechanical behavior and define the crack mechanism, goes through the definition of the fiber volume fraction. The reinforcing phase is, in fact, responsible of the composite material's resistance under the application of a load and, consequently, a greater or a smaller amount of fibers influences the value of properties such as the proportional limit, yield strength or fracture strength.

Nevertheless, it is obvious that the only characterisation of this parameter is not enough to completely understand the stress and strain field who modifies, in a meaningful way, the crack initiation process. Indeed, microstructural details like fiber distribution or imperfections generate high local stresses and/or strains [7], causing weakness in such areas: it is not unusual that, considering a cross-ply laminate, the transverse plies are cause of crack initiation even though their load is lower than that one associated to the parallel plies [16].

Therefore, it is possible to indentify two different variability factors: the first one consists of the constituent properties, as it was studied during the years [20, 17]; instead the second one is about the morphological variability, that is any divergence from the ideal fiber arrangement, defined by the hexagonal pack of fiber [35], that

can lead to fiber clustering or accumulation of matrix. This morphological non-uniformities are caused by techniques and parameters chosen for the manufacturing process and, since often they are not editable, it is necessary to characterize them in order to evaluate how they affect plastic deformation, damage evolution and fracture of the global material.

In this chapter, statistical descriptors of the fiber arrangement are investigated to provide quantitative informations about the randomness' degree and to detail the interaction for both long range and short range. Then, they are applied to different repeating unit cell and it will be possible to distinguish the pattern of the second-phase population and to correlate the latter with the local stress field.

4.1 Nearest neighbor distribution

As the name can suggest, the nearest neighbor distribution can be seen as the as the probability of finding the closest neighbor of a given point as a function of the distance from that particular reference: it is given by the probability density function $\psi(r)$ such that $\psi(r)dr$ is the probability to have no point in the circular region defined by the distance r from a given fiber's center and to have at least one point in the annular region with inner radius r and outer radius $r + dr$. It can be seen as a descriptor of the minimum distance between fibers and this is particularly important in the micromechanical behavior of the composite material, since it has been found that the greatest peak in the stress field, which can produce a fracture, normally appear where the inter-fibers distance is smallest [15].

So, this distribution function can be used to detail short range fibers interaction, if the closest neighbor is considered, but it can even be used as a quantitative descriptor of intermediate and long range interaction, if higher order nearest neighbor are taken into account.

The first possibility that we have is to consider the random array of fibers as a spatial point pattern, an arrangement of zero-dimensional point in a two-dimensional geometry. This can be represented by a stationary Poisson point process [37], defined by an intensity N_A , namely the total number of points divided by the area

of observation. In the stationary Poisson point process, the probability that the nearest neighbor is located exactly at a distance defined by r is easy to obtain and it is given as follows [38]

$$\psi_n(r) = 2\pi r N_A \frac{(\pi r^2 N_A)^{n-1}}{(n-1)!} e^{-\pi r^2 N_A} \quad (4.1)$$

where n defines the neighbor's order that we want to analyze. The expression for the closest neighbor, i.e. $n = 1$, is given by Gurland in [9].

Now, a real microstructure of a composite material consists of unidirectional fibers of finite size in a three-dimensional space which becomes, if we consider the cross-section that is the fundamental point of our study, a set of randomly arranged circles in a two-dimensional geometry: this means that the distribution is similar the one described by the Poisson point process but, since it can't exist fiber overlapping, the position of every entity is not independent from that of the other fibers inside the cell. For this reason, the Eq. 4.1 cannot be used to describe the nearest neighbor probability density function. Nevertheless, we may assume that the position of every fiber is defined by zero-dimensional points distant each other at least the fiber diameter and that the nearest neighbor probability distribution function follows the Gaussian distribution (or Normal distribution).

The normal distribution is the most common continuous probability distribution, widely used to represent random variables whose distributions are uncertain or that are supposed to concentrate their value around a single mean one. It is defined by the two parameters:

- μ , the mean value or the expectation of the variable

$$\mu = \frac{\sum_{n=1}^N x_n}{N} \quad (4.2)$$

where x_n is the variable of interest and N is the total number of occurrences;

- σ^2 , the variance, that is the expectation of the squared deviation from the mean value (where σ is the standard deviation)

$$\sigma^2 = \frac{\sum_{n=1}^N (x_n - \mu)^2}{N - 1} \quad (4.3)$$

The probability density function of the Gaussian distribution is

$$f(x|\mu, \sigma^2) = \frac{1}{\sqrt{2\pi\sigma^2}} e^{-\frac{(x-\mu)^2}{2\sigma^2}} \quad (4.4)$$

and this very function will be used to define the nearest neighbor distance probability function, considering the variable x as the distance between a given fiber's center and its closest neighbor.

It is therefore essential to develop a script that can compute the distance between a fixed point and the others forming-part of the population in order to find then the minimum of these distances: for this purpose, the MATLAB environment has been chosen.

4.2 Second-order intensity function

In order to distinguish between different types of point patterns and to characterize the long-range fibers interaction, the second-order intensity function, also known as the Ripley's K-function, is the most used descriptor.

This function is defined as the number of further points expected to lie within a radial distance from a given center and divided by the number of points per unit area, N_A . The reason why this descriptor is associated to the figure of B.D. Ripley is that he provided a correct estimator to take into account a correction for the effect of the edges' proximity [34]. The equation that can be used to estimate this descriptor, is the following

$$K(r) = \frac{A}{N^2} \sum_{k=1}^N w_k^{-1} I_k(r) \quad (4.5)$$

where A is the area of observation, N is the total number of points, $I_k(r)$ is the number of points inside the circular area defined by the radius r and w_k is the ratio of the circumference contained within the area A to the whole circumference with radius r , in other words the correction factor, as shown in the Fig.4.1.

In addition, to understand the functioning of the second-order intensity function, it is possible to refer to the work of Pyrz [32] who used this descriptor to distinguish different spatial point pattern. Some examples of points arrangement are reported in Fig.4.2.

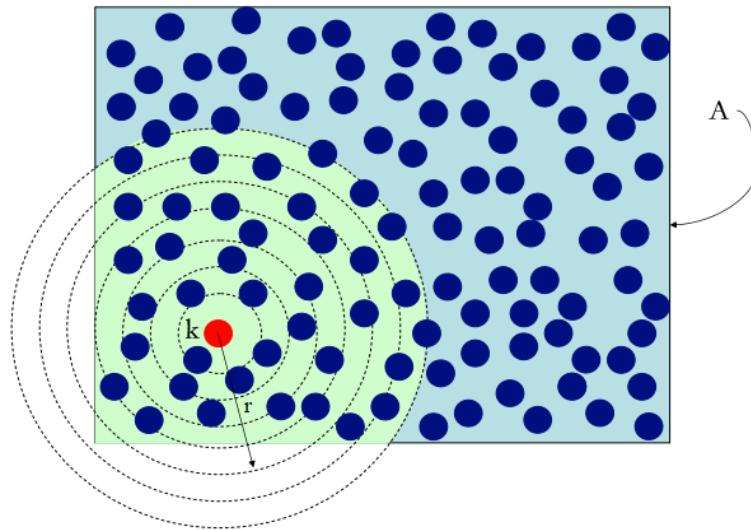


Figure 4.1: Estimation of $K(r)$ [22]

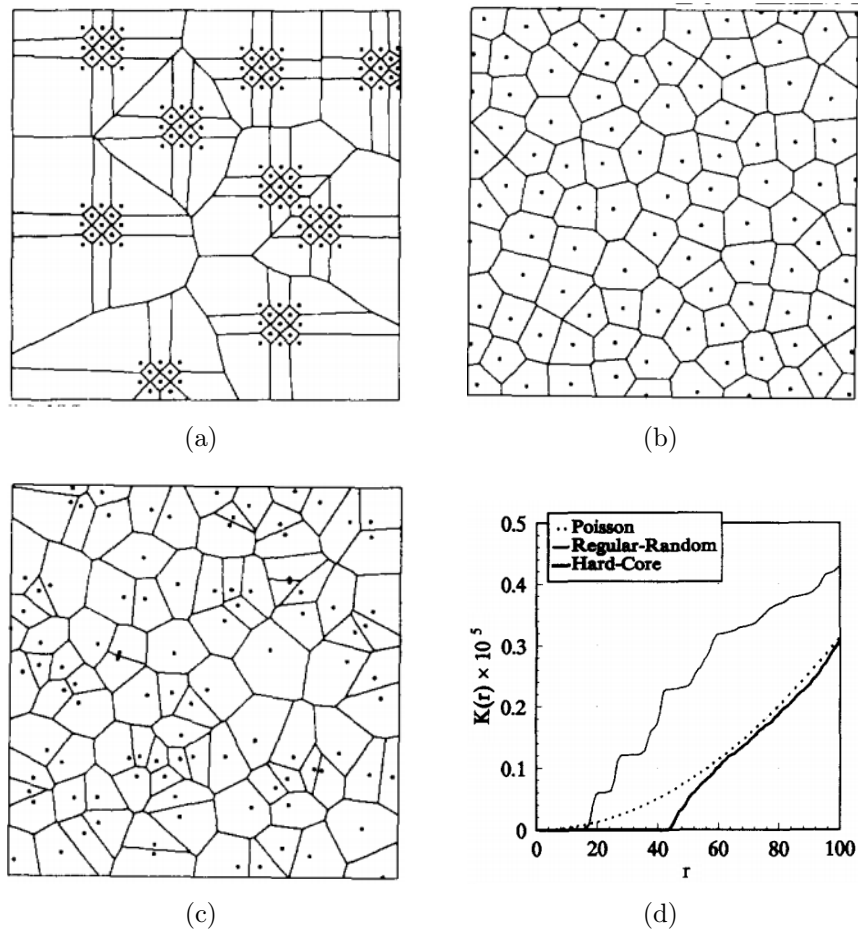


Figure 4.2: From top left to bottom right: regular-random, hard-core and Poisson arrangement and relevant K-function [32]

Firstly, it is necessary to remember that the Poisson distribution is built under the hypothesis of completely positional independence, which means that for every point in the area of observation, each possible location has about as much chance to be chosen as every other else. Although this distribution doesn't fit well the real case, in which there is the constraint of the fibers overlapping, the Poisson process of points is one of the most studied and may sometimes provide a useful basis for comparison to understand how a pattern deviate from complete randomness. Moreover, if from the figure seems that the arrangement is not so chaotic, with couples of points close and large empty regions, any impression of aggregation is misleading [32]. The second-order intensity function for the Poisson distribution is well-known and equal to πr^2 [31] and its line on the K-function graph divides clustered patterns from regular arrangement.

The regular-random pattern shows instead a characteristic "stair" shape, similarly to a regular set, alternately horizontal fragments and tract with a high slope: the first ones are indicative of an empty region in the cell at the corresponding distances, while the second ones identify clustered amount of points. It is therefore important to say that a strong clustering of regular random-random models results in a function far above the $K(r)$ corresponding to the Poisson set.

Finally, for the hard-core distribution, probably the most similar to that reproduced in this thesis. The relevant K-function is, at first, constant and equal to zero since the minimum inter-punctual distance is defined by the finite size of the fibers, then it approaches to the Poisson curve from below, suggesting that, at the end, the distribution is on the regular side of random [32]. The sensibility of this function is such as to be capable to identify every disturbance of a regular pattern: in fact, since a perfect regular arrangement would have a ideal step function, in the event of a distorsion the curve will decline from its ideal trend.

It is also important to report the work of Zeman and Šejnoha [45] who have evaluated the effect of the correction factor w_k comparing the values of the K-function assuming periodicity to the values obtained using the correction factor w_k , in order to take into account points outside of the sampling area. This result is shown in Fig.4.3

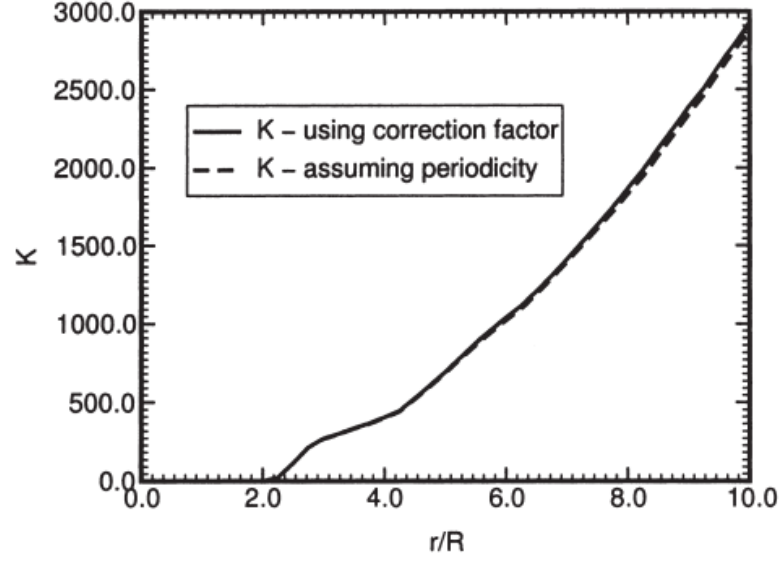


Figure 4.3: Effect of the w_k factor in according to [45]

4.3 Radial distribution function

The last descriptor that can be used to define the arrangement of fibers and the degree of randomness is directly derived from the second-order intensity function [31]. Starting from the definition of the second-order intensity function, who gives the average number of points lying within a radial distance from a given center, if we want to know the average number of fibers whose center lies in an annular region with inner radius r and outer radius $r + dr$, it is sufficient to evaluate the difference

$$dK(r) = K(r + dr) - K(r) \quad (4.6)$$

and to divide this value by the area of the ring, $2\pi r dr$, and the number of fibers per unit area, N_A [2]. This leads to the radial distribution function, or pair distribution function, $g(r)$, which is defined by the equation

$$g(r) = \frac{1}{2\pi r N_A} \frac{dK(r)}{dr} \quad (4.7)$$

where N_A is the ratio of the total number of fiber N in the observation area A , while the other elements are already known.

Referring to the the work of Matsuda et al. [24], it is possible to obtain a discretized definition of the pair distribution function as follows

$$g(r) = \frac{1}{2\pi r N_A dr} \frac{1}{N} \sum_{i=1}^N dK(r) \quad (4.8)$$

where N is the total number of centers in the considered area, and that provides the same results of the continuous definition.

The radial distribution function provides not only informations about the variation of the average fiber density as a function of the distance from a point [41], but even informations about the occurrence intensity of inter-fibers distances: local maxima indicates a inter-fiber distance more frequent while local minima represent the least ones. Here there are some examples taken from Pyrz [31], which show the pair correlation function $g(r)$ for some well-known point pattern

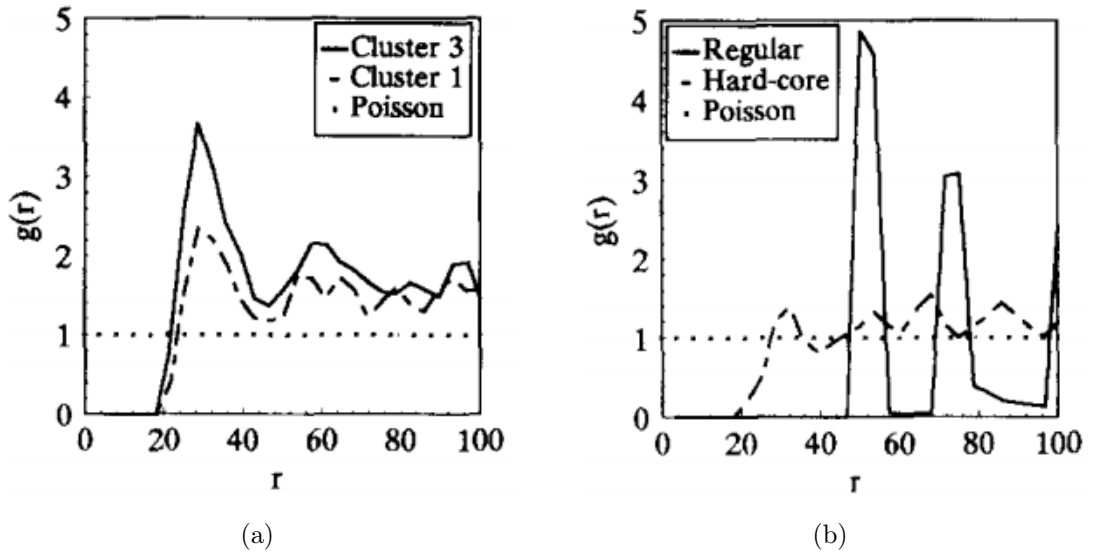


Figure 4.4: Pair distribution function, from [31]

The values obtained for a random Poisson distribution are identically equal to 1: therefore, values of $g(r)$ which lies above the Poisson one show that the relevant distance occurs more frequently than in the case of perfect randomness, while, on the contrary, values smaller than 1 define infrequent distances [31]. For this reason, it seems reasonable to assume that, in a cross-section with a random distribution of fibers, the damage initiation will happen where $g(r) > 1$. Nevertheless, for a population of finite size fibers, such as the one that will be examined, a value of the pair distribution function greater than 1 doesn't mean necessarily clustered fibers. This is because, as demonstrated in the work of Yang et al. [44], $g(r)$ for an actual material depends not only on the spatial fibers centers pattern but even on the fiber volume fraction, on the average size of the second-phase, etc. Also, it is

important to specify that the radial distribution function tend to be unitary as the value of the radius tends to be infinite. In fact, since the area of the annular region is linearly dependent on the radius ($A_{ar} = 2\pi r dr$), as the distances become sufficiently large, the annular area becomes so large that, automatically, it will contain every possible variation of the fiber distribution. So $dK(r) \rightarrow N_A(2\pi r dr)$ as $r \rightarrow +\infty$ and consequently $g(r) \rightarrow 1$ [44].

Anyway, if it is possible to find a value of r for which the function is approximately equal to 1, this distance can be seen as the scale of local disorder [31], that is the distance by which the effect of a local geometrical disorder should be taken into consideration, a geometrical range of inter-fibers interaction. Instead, for a deterministic distribution, the pair distribution continuously decreases, showing peaks in correspondance of a deterministic inter-fiber distances [22].

4.4 Analysis of the repeating unit cells

Once the statistical descriptors were defined, it is necessary to use them to describe the fiber arrangement in every repeating unit cell, in order to define the degree of randomness and how this affects the strength of the composite material.

As said before, different amounts of fibers were chosen for the RUCs so to have several possibilities for the fibers centers pattern, which is reflected, in turn, in a wider coverage of actual cases. Every RUC created has been reported in the first chapter of this thesis, while the all curves obtained for each of them are in the Appendix.

4.4.1 Five-fibers RUCs

The first type of RUC analyzed is that with five fibers.

Nearest neighbor distribution function In order to show different possibilities in the nearest neighbor distances, five repeating unit cells are chosen, defined by numbers 3, 6, 8, 9 and 10, since they seem to cover a broader range of cases. Both the

probability density function and the number of occurrences of the nearest neighbor distance will be shown to better define the fibers centers pattern.

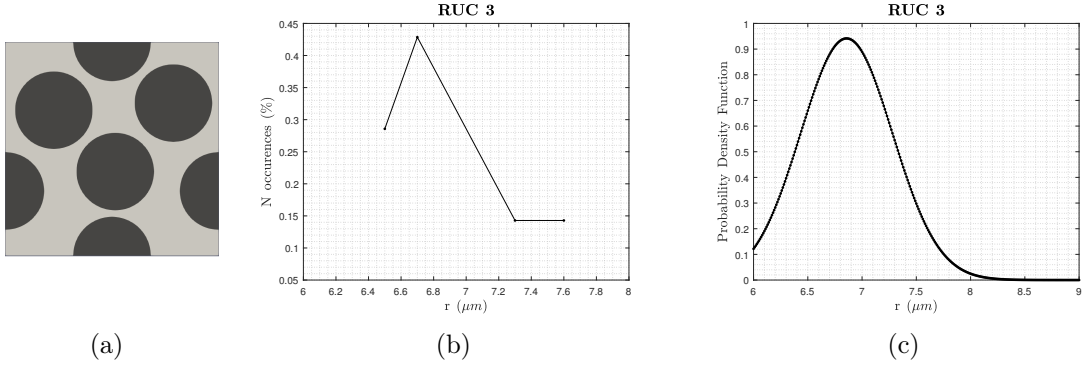


Figure 4.5: Five-fibers RUC #3 and relevant nearest neighbors distances and distribution function

For the RUC 3, which contains seven points of observation, there are four different distances between a fiber and its closest neighbor, as it is possible to see in Fig.4.5(b). This means that, even if the cell seems to have a regular pattern in the fiber distribution, actually the spacing is not constant but there are two couples of points who are closer in respect to the others.

However, since the number of fibers contained is relatively small, it is easy to think that the two occurrences are indeed the same distance of $6.7 \mu m$ measured two times: the first one from a fiber 1 to its closest neighbor, the fiber 2; conversely, the second time from the fiber 2 to the fiber 1. Being this distance smaller than others, we can expect that this inter-fiber region will be the crack initiation zone.

In the end, since the first nearest neighbor distance occurs for a value greater than $6 \mu m$, there aren't fibers in contact, as we can actually see from the RUC representation in Fig.4.5(a).

The RUC #6 (see Fig.4.6) has 6 points of observation out of 8 who are closer while the remaining two are more far. Also, the three smaller values are diversified by only a tenth of micron: this means that the damage of the material will be influenced not only by the inter-fiber distance but even from some other factors, like the quality of the fiber-matrix interface.

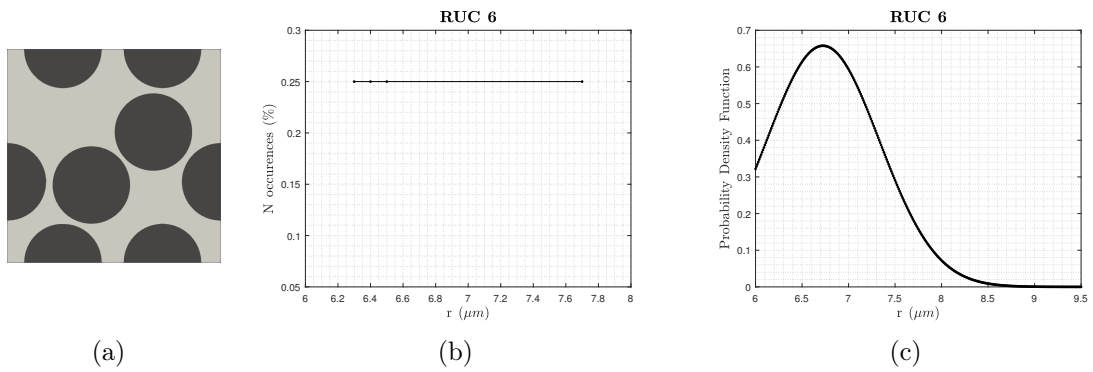


Figure 4.6: Five-fibers RUC #6 and relevant nearest neighbors distances and distribution function

It is nevertheless important to make clear that, even if the distances are well-distributed, the degree of randomness reached in this case is high, because a lot of possibilities, in terms of distances, have the same probabilities to happen: the low and wide curve of the probability density function demonstrates this, so it is possible to think that this spatial point pattern is very similar to a hard-core pattern seen in the Pyrz's work [32]. In fact, in that distribution, every point of the RUC has the same probabilities to be occupied by a fiber than any other point as long as there is not fibers overlapping, as it is happening in this case.

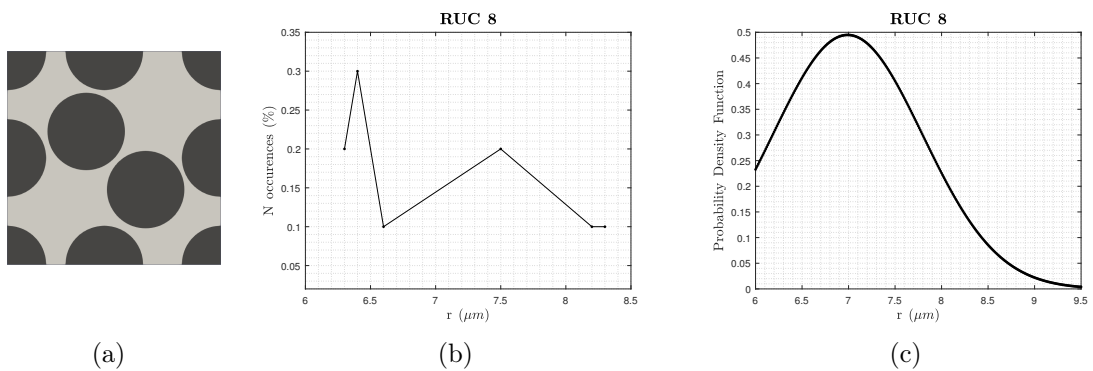


Figure 4.7: Five-fibers RUC #8 and relevant nearest neighbors distances and distribution function

The two curves resulting for this RUC #8, containing 10 fibers, show us a good degree of randomness: the two more internal fibers, substantially, are differently spaced from the others, although of a small amount, and, moreover, they interrupt

a regular pattern. This can be a good example of unintended inclusion in the reinforcing phase.

The probability density function of the nearest neighbor distances covers a wide range of distances, which means that stress and strain field will be extremely variable.

The fourth case (see Fig.4.8) shows us a very simple situation, with two couples of fibers near, with a small nearest neighbor distance, while the other ones have a greater distance from its closest neighbors. This suggests that these two couples of fibers with a smaller inter-fiber distance will be that between which the strain and the stress will increase until the breaking point.

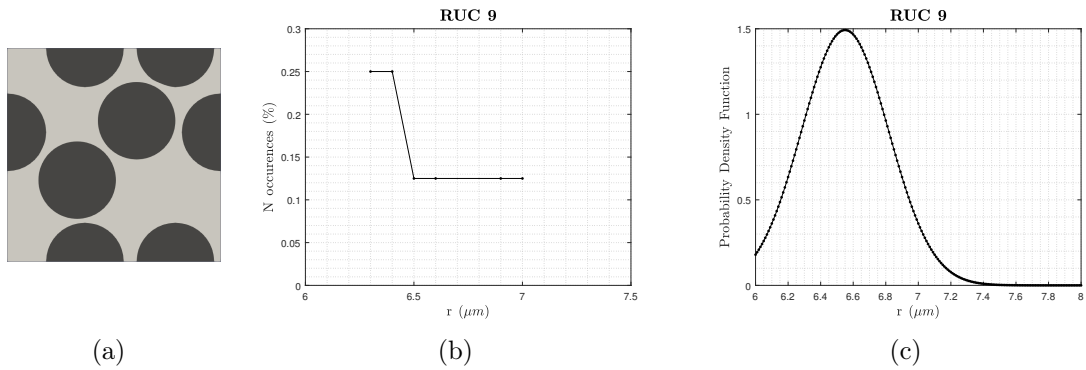


Figure 4.8: Five-fibers RUC #9 and relevant nearest neighbors distances and distribution function

It is good to notice that in no case fibers overlapping or contact is showed, since the nearest neighbor distance is always strictly greater than the fibers' diameter. Moreover, it results that a greater degree of randomness is reached when the curve of the nearest neighbor distance's occurrences is horizontal, i.e. when the probability density function is low and wide, because this can be intended as no regularity in the arrangement of the fibers. On the contrary, a higher and narrow pdf would mean that fibers are regularly spaced.

For the last case (see Fig.4.9), we have choose a RUC with 7 points of observation which shows a very high degree of randomness. In fact, as it is possible to imagine looking at the fibers' centers pattern in Fig.4.9(a), the fibers cover the area of observation without clustering.

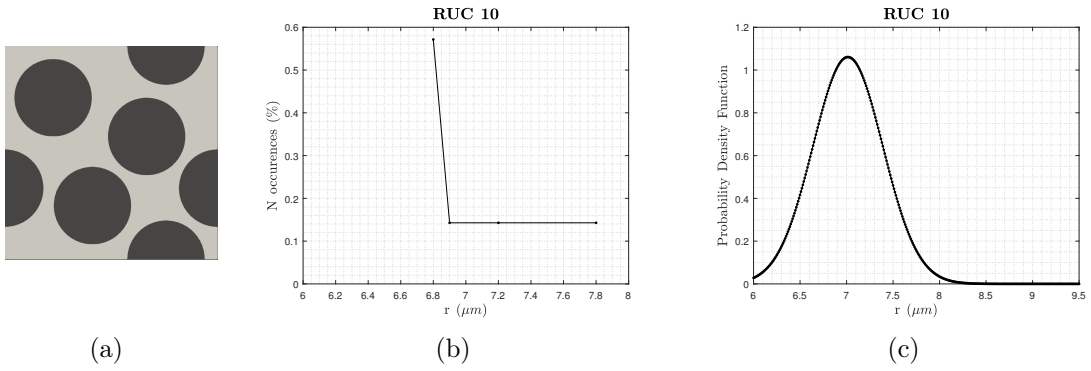


Figure 4.9: Five-fibers RUC #10 and relevant nearest neighbors distances and distribution function

The result of this arrangement is that the distance of $6.8 \mu m$ is the most frequent because it was evaluated for 4 times out of 7: considering the small number of fibers, this can mean that two couples of fibers are the closest, a situation similar to that one seen for the RUC 9, in Fig.4.8.

After these examples, it seems easy to understand that the degree of randomness which affects these RUCs, influences the strength since a different distance between two fibers causes a different stress and strain field.

Second-order intensity function Now it is possible to analyze the second-order intensity function for the same RUCs, in order to understand something more about the long range interaction between fibers.

The analysis is stopped for a value of the distance for which w_k is not so small, i.e. the circumference considered is not entirely outside of the RUC, in this way the function won't approach to infinite. Also, the mesh used in MATLAB for r is very dense so to catch every variation in the area of interest, even if the function will appear fragmented.

The first characteristic that can be noticed, looking at Fig.4.10 is that the second-order intensity function is identically equal to zero until a particular distance: the value of r for which the function is, for the first time, different from zero is the same who can be found in the nearest neighbour distance curve of the occurrences as the smaller distance between two closest neighbors.

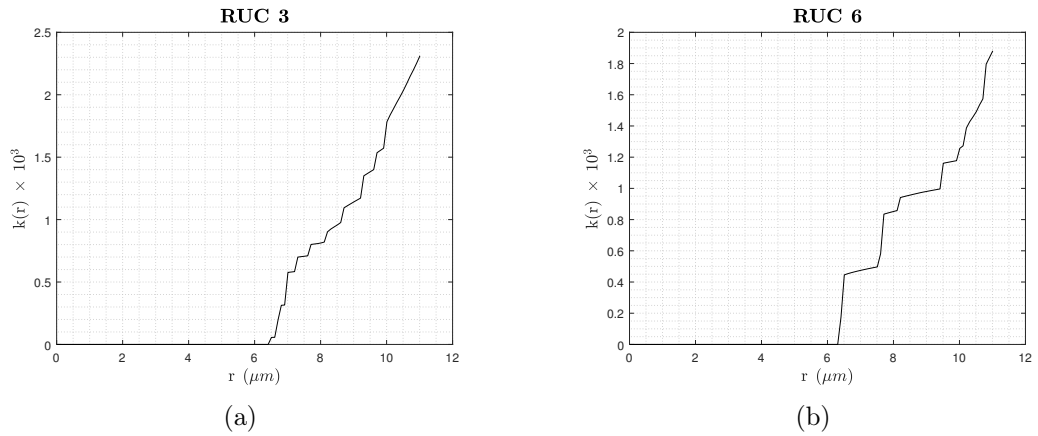


Figure 4.10: Second-order intensity function for RUC #3 and RUC #6

In fact, if the circumference has radius $r \leq 6 \mu\text{m}$, there are no fibers inside its area, so the value of $k(r) = 0$. Moreover, the fewer the occurrences for the smallest nearest neighbor distance, the smaller the first value of $k(r) \neq 0$.

It is even possible to see how the two curves show a totally different pattern: for the RUC 3, the function is made by short tracts, which is identifier of a high variability of the inter-fibers distance and a high degree of randomness, while, for the RUC 6, the curve is made by longer tracts, which means that the number of occurrences for the same inter-fibers distance is greater than 1. Similarly, longer tracts with a lower slope means empty regions in the area of observation: the two informations combined demonstrate that the RUC 6 is more regular than the RUC 3, information confirmed by the trend of the nearest neighbor curves.

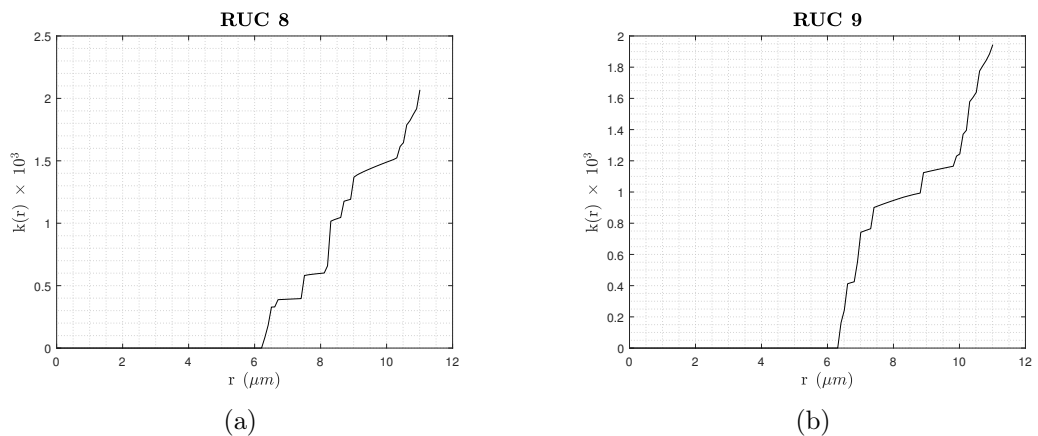


Figure 4.11: Second-order intensity function for RUC #8 and RUC #9

The RUC 8 is that one with the greatest number of points of observation and the trend of the curve is highly fragmented: in fact this cell exhibits a pronounced set of stairs that can suggest a regular pattern of the points, as it is possible to say looking at Fig.4.7(a).

Nevertheless, the different size of every stair let us assume that the distance between every fiber is variable, so this pattern is random but less than the other RUCs seen so far. Differently, the RUC 9 exhibits, at first, a vertical trend of the curve that, though with some short fragments with low slope, lasts for a greater value of r .

Actually, the RUC 6 and 9 seem really similar at first sight but the second-order intensity function is very sensitive to every variation in the punctual pattern analyzed, so that it is possible to understand the difference between the two RUC: the RUC 6 has a more regular trend since the curve looks like a *stair-shape* function, that is characteristic of the regular pattern (Pyrz [32]); instead, the RUC 9 shows a regular-clustered trend, which means that a high number of fibers are clustered while, for long range, the matrix occupies most of the cell.

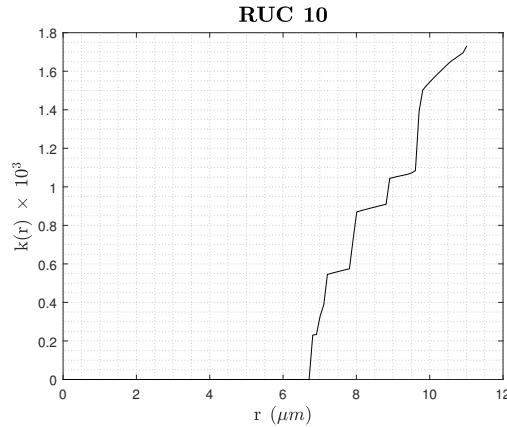


Figure 4.12: Second-order intensity function for RUC #10

The last RUC is the number 10. The trend of the second-order intensity function is different from the other RUCs seen until now: in fact, the function tends to assume higher slope for short- and long-range (i.e. between 6 and 8 μm and between 10 and 12 μm), while it is flat for the medium-range.

So it is easy to think that, with respect of a given point, there is some fibers clustering for short and long distances and empty regions for medium distances.

Radial distribution function The third statistical descriptor is the radial distribution function, defined in the previous section, with which it is possible to figure out the variation of the fiber density in respect to the distance from a given point.

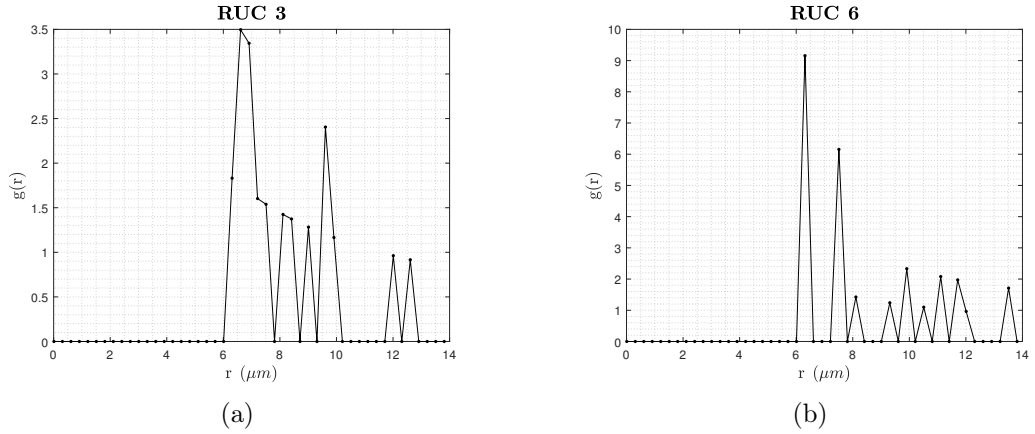


Figure 4.13: Radial distribution function for RUC #3 and RUC #6

As it was found with the second-order intensity function, this function has values different from zero only for $r > 6 \mu m$, because there isn't fibers overlapping. Moreover, the choice of the distance mesh in MATLAB has a very strong influence over the results: since we are evaluating the number of points inside an annular region with thickness equal to dr , a dense mesh, with a very high number of elements and a small dr , results in a thin shell and, considering the low number of fibers inside the RUC, a lot of situations in which the annular area doesn't catch the fibers' centers. This explain the high number of distances for which the value of the function is equal to zero.

Nevertheless, the trend of the curve is very clear. As it was possible to understand from the literature, the Poisson curve, which define the complete random pattern, is indentically equal to one: for this reason, values of $g(r)$ greater than one means that the relative distance, that has to be read as a particular inter-fibers distance, is more frequent than abscissa's value with a radial distribution function lower than one. So, for the RUC 3 there are a lot of radii for which $g(r) > 1$, i.e. a highly random repeating unit cell, while for the RUC 6 a couple of distances show a pair distribution function far greater than one, which can be read as a more regular arrangement. Furthermore, as we can see in Fig.4.13(b), the curve has an asymptote equal to 1,

so $N_A = N/A$ is illustrative of the entire section.

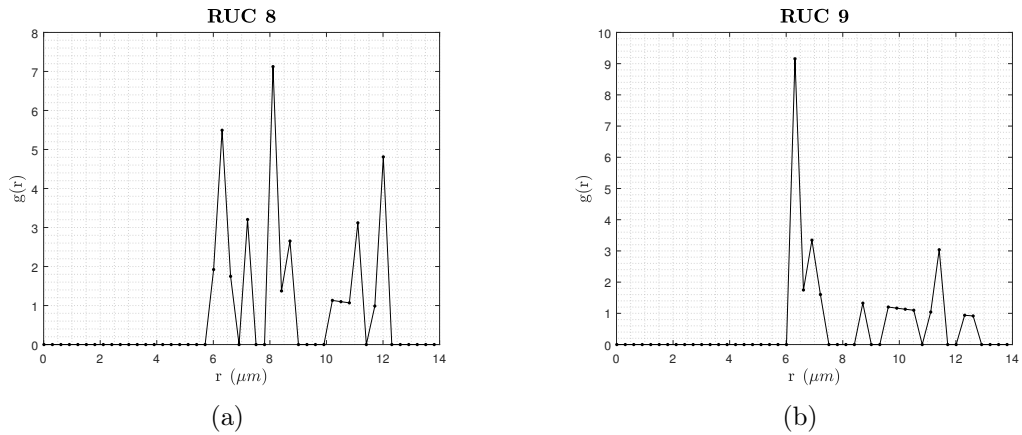


Figure 4.14: Radial distribution function for RUC #8 and RUC #9

The RUC 8 has a very particular trend, similar to the regular pattern described in the literature, with a lot of spikes and zeros. Moreover, since there aren't values of r for which the function approaches to a constant value, it is not possible to define a scale of a local disorder which, in fact, affects the whole RUC.

On the contrary, the curve of the RUC 9 have a trend similar to the hard-core pattern: the function rapidly decreases after a first peak, which is the value of the inter-fiber distance more frequent, and it seems to assume a constant value for high r . Actually, it would be like this if it wasn't for the reduced dimensions of the RUC who make empty every annular region before achieving of a constant value.

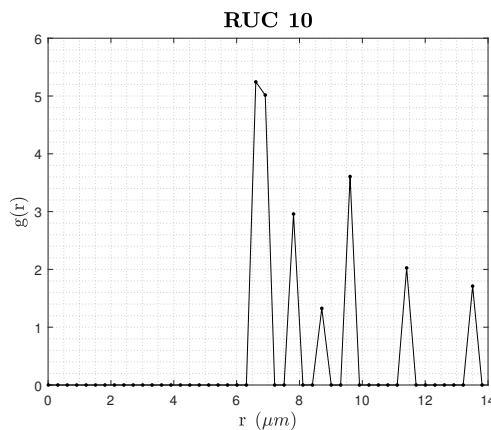


Figure 4.15: Radial distribution function for RUC #10

In the end, the radial distribution function for the RUC 10 shows us several peaks: the average density of fibers is extremely variable and, in particular, this

seems higher for both short- and medium-range, that are the distances identified by the higher values of $g(r)$. Obviously, even in this case, as r increases, the function tends to be zero, since the annular region would be outside the RUC.

4.4.2 Ten-fibers RUCs

Nearest neighbor distribution function As done in the previous section, five different RUCs are chosen, containing 10 different fibers, with both the probability density function and the number of occurrences of the nearest neighbor distance.

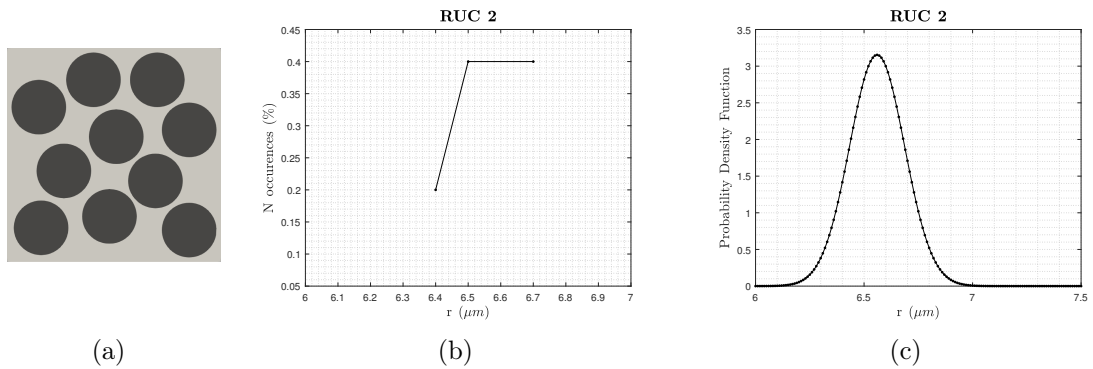


Figure 4.16: Ten-fibers RUC #2 and relevant nearest neighbors distances and distribution function

The RUC 2 contains ten points of observation, from which only three different distances results with respect of its closest neighbor. As we can see from Fig.4.16(b), a value of $6.4 \mu\text{m}$ was found for 2 times out of 10 while $6.5 \mu\text{m}$ and $6.7 \mu\text{m}$ divide equally the remaining 8 events. Obviously, this is reflected in the probability density function, which focus itself around these two values. For these reasons, it is possible to think that the cell coverage is sufficiently regular even if the RUC itself has a good degree of randomness, since the disposition doesn't follow a particular pattern.

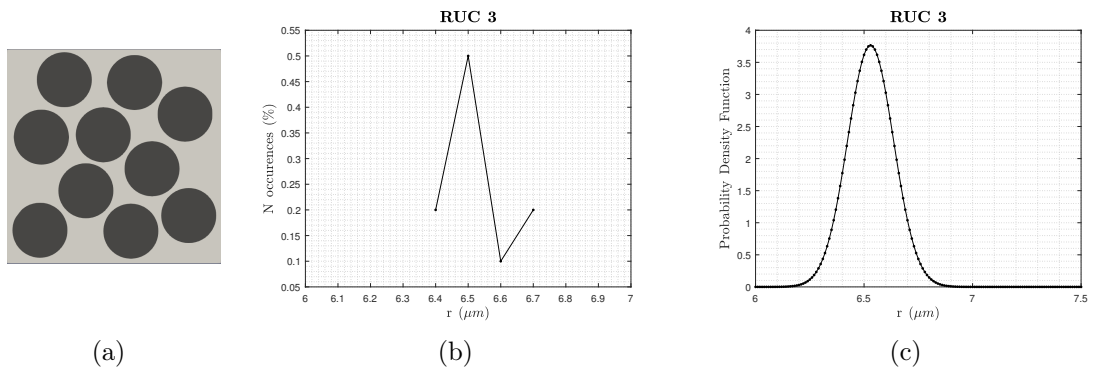


Figure 4.17: Ten-fibers RUC #3 and relevant nearest neighbors distances and distribution function

Looking only at the fibers pattern, showed in Fig.4.17(a), this repeating unit cell doesn't seem so different from the previous one, exhibiting the same number of points of observation and a complete random arrangement. Nevertheless, the short-range interaction between the fibers is different since there is one particular inter-fibers distance that happens for most of the times ($6.5 \mu m$ for 50% of occurrences). This will influence the stress and strain field, modifying the strength of the material. The resultant probability density function is more narrow than the previous one, with a peak around that value of the distance.

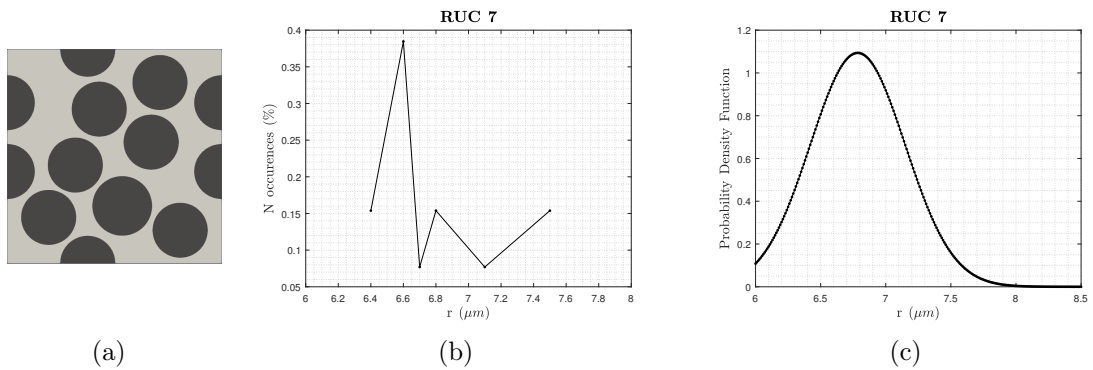


Figure 4.18: Ten-fibers RUC #7 and relevant nearest neighbors distances and distribution function

The situation represented with the RUC 7 is far from the previous two showed until now. Even though in Fig.4.18(b) is appreciable a value of the nearest neighbor distance which occurs more frequently than any other else, it has to be taken into account the number of fibers centers in the RUC. In fact, since there are 13 points

of observation, the distance $r = 6.6 \mu m$ can be found only for 5 times, compared to the other relative maxima, which correspond to 2 occurrences. What was said can be cleared looking at Fig.4.18(c) where it is represented the probability density function who results wider and more flattened compared to that ones in Fig.4.16(c) and 4.17(c). Therefore, it is difficult to understand only with this informations where the crack will initiate.

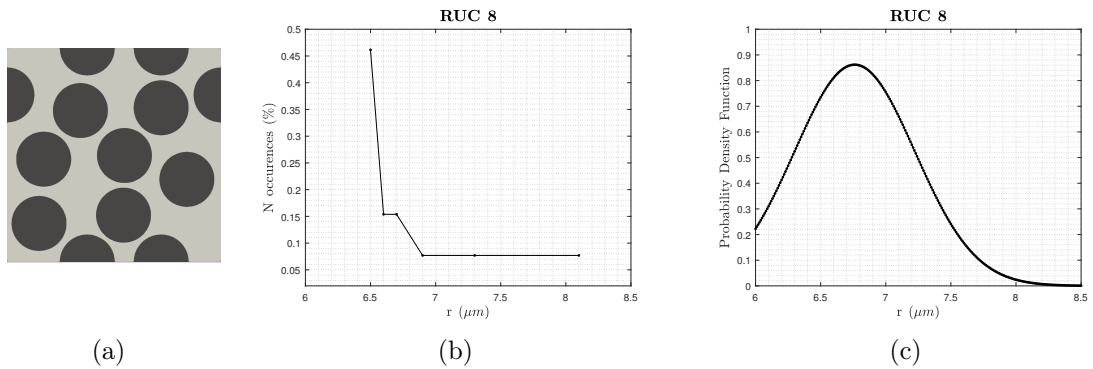


Figure 4.19: Ten-fibers RUC #8 and relevant nearest neighbors distances and distribution function

The RUC 8 shows a behavior, for the short-range interaction, similar to the last one, with a wide and flattened probability density function but, actually, the result obtained in Fig.4.19(c) is distorted by the presence of a fiber isolated from the others. The number of occurrences' curve exhibits an initial peak, reaching almost the 50% of the total occurrences, and then other 5 different distances which happens for a fewer times. For this reason, the pdf curve should be stretched around the most frequent value: if this didn't happen it is because, for a single time, a nearest neighbor distance of $8.1 \mu m$ is measured, relatively to the isolated fiber, and this make the average value of the nearest neighbor distance increases. Because of this increased value, the pdf is flattened so to cover a wider range of distances. Anyway, the repeating unit cell doesn't seem to have a regular spatial point pattern but only evenly spaced fibers.

The last RUC chosen is the number 9. It is the RUC with the greatest number of points of observation (16) so the number of occurrences' nearest neighbor curve should be particularly variable.

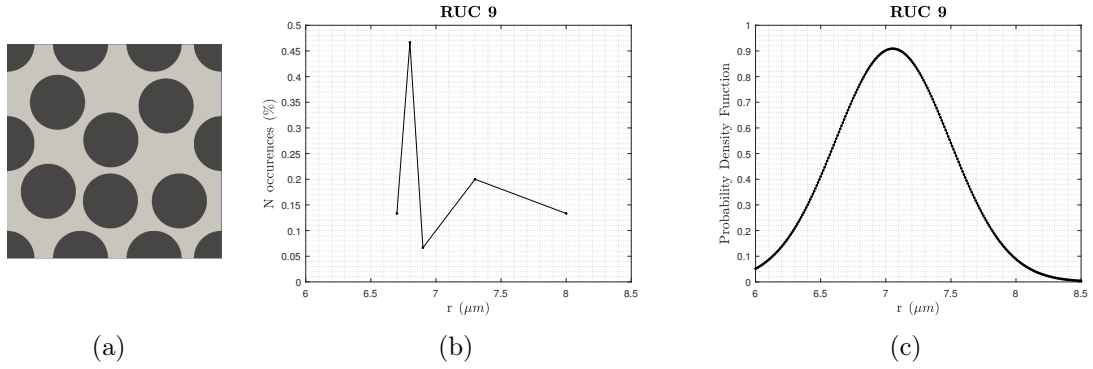


Figure 4.20: Ten-fibers RUC #9 and relevant nearest neighbors distances and distribution function

Actually, only five different distances are measured which means that the values recur between different couples of fibers and that the higher values in the stress and strain field may be located in different regions of the cell. Furthermore, it is important to notice that the trend of the curve in Fig.4.20(b) is very similar to the one concerning the RUC 7 but, since a greater number of fibers are located on the edges of the repeating unit cell, a fewer fibers are inside the area so that the fiber volume fraction is constant but the average inter-fibers distance is higher. As result, the trend of the curve is similar, so that we can imagine a similar punctual pattern, but it is translated by $0.5 \mu m$ so that the strength of the RUC should reflect that. Similarly, the pdf curve has a highest value a little lower than the pdf curve for the RUC 7, which depends on the number of fibers inside the cell, and the function is traslated to greater distances.

Second-order intensity function Then, in order to define the long-range interaction between fibers and to understand the fiber arrangement, we can observe the k-function. As we can see from the two figures (Fig.4.21), since there is no fibers overlapping, the second-order intensity function start for values of the distance greater than $6 \mu m$. Moreover, what was said for the five-fibers RUC is still valid: the function is highly fragmented because of the number of points inside the cell and because of the spacing of the distance's mesh chosen in MATLAB which the more is dense, the greater the probability of finding empty regions in the cell, i.e. horizontal tracts of the curve.

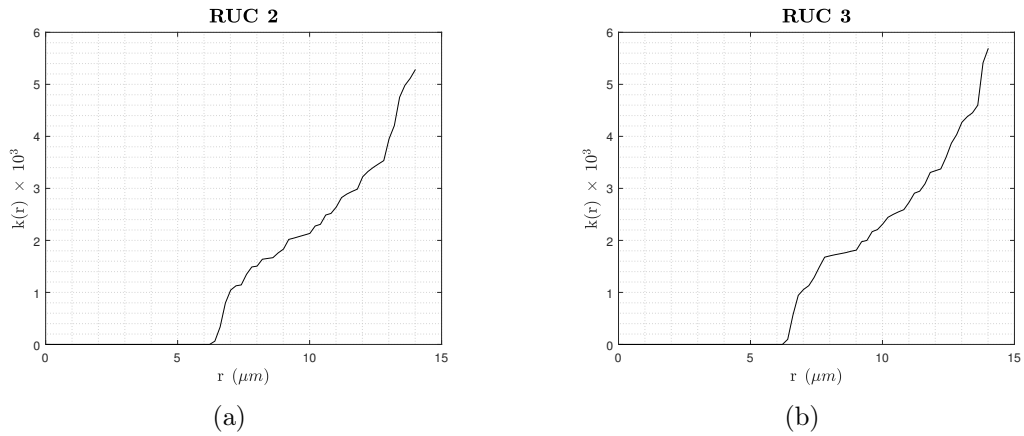


Figure 4.21: Second-order intensity function for RUC #2 and RUC #3

The general trend is more interesting to characterize: for both the two RUC, the curve assumes the same values at short- and medium-range and the first idea made looking at the nearest neighbor distribution function is confirmed. The cells seems similar but, while the distance between a given point and its closest neighbor resulted different in the sense of the frequency of the event, here the average interaction between fibers is defined and, for $r \leq 13 \mu m$, the trend is the same. A bigger difference instead results for high values of the radius as the final value of $k(r)$ differs by 0.5×10^3 . This means only that the fibers, for the RUC 2, are shifted towards the edges of the section. That said, the pattern for the two RUCs is what we can expect from a hard-core pattern, as seen in Pyrz [32].

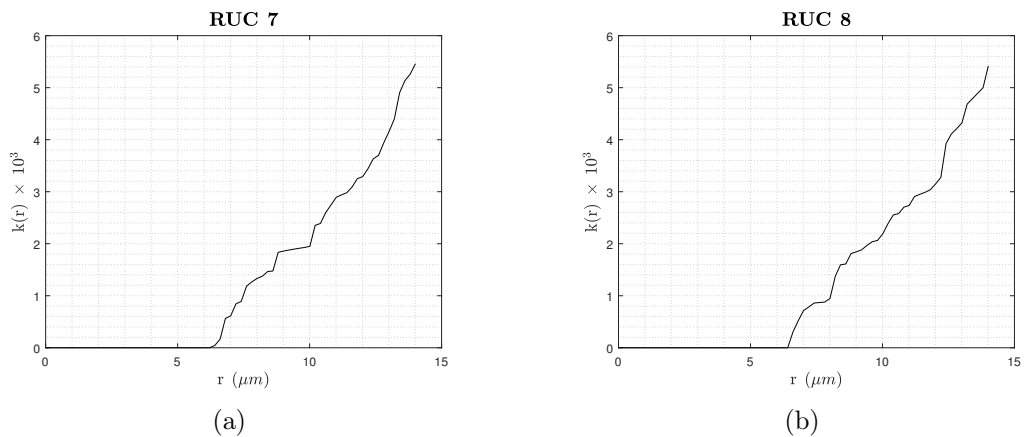


Figure 4.22: Second-order intensity function for RUC #7 and RUC #8

The next RUCs, in Fig.4.22, are identified by number 7 and 8. Both the curves

exhibit a more linear general trend, with a concavity less accentuated which defines, in respect to the previous unit cells, less clustered fibers. On the contrary, if we focus our attention on a smaller scale, several differences will become clear. Horizontal fragments of the curve are indicative of empty regions in the area of observation and, in general, a lower slope means a lower concentration of fibers for the relevant distances: in this sense, it is possible to highlight the difference between the two RUC because the n^o 7 has a more visible horizontal tract around $10 \mu m$ (so on average that distance from a given center is occupied by the matrix); the n^o 8 instead shows two distinct horizontal tracts around $7 \mu m$ and $12 \mu m$, which means that the medium range interaction for the two unit cell is different.

What was said certainly will define a different crack propagation, but, anyway, these considerations will be more clear during the micromechanical study of the cross-section.

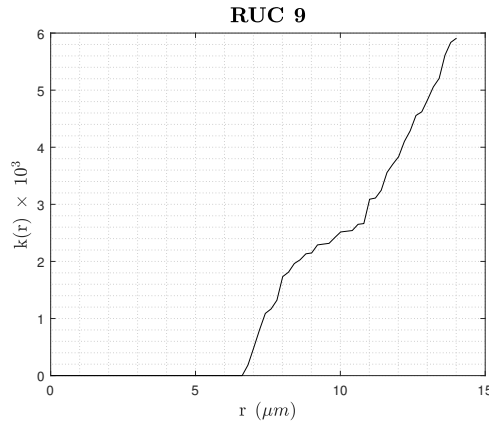


Figure 4.23: Second-order intensity function for RUC #9

The last RUC shows a trend that is characteristic for unit cells with a low number of fibers, as it is possible to see in the work of Liu and Ghoshal [19]. The function, in fact, has a high slope for short distances, which means a high degree of interactions for short-range, while tends to be horizontal for medium range, i.e. empty space in the section. Then the function increase the slope once again because of the presence of other fibers and a lower value of the correction factor w_k , since a greater fraction of the circumference used to describe the radial distribution is outside the area of observation.

Radial distribution function In the end, the second-order intensity function for the same unit cells is here represented.

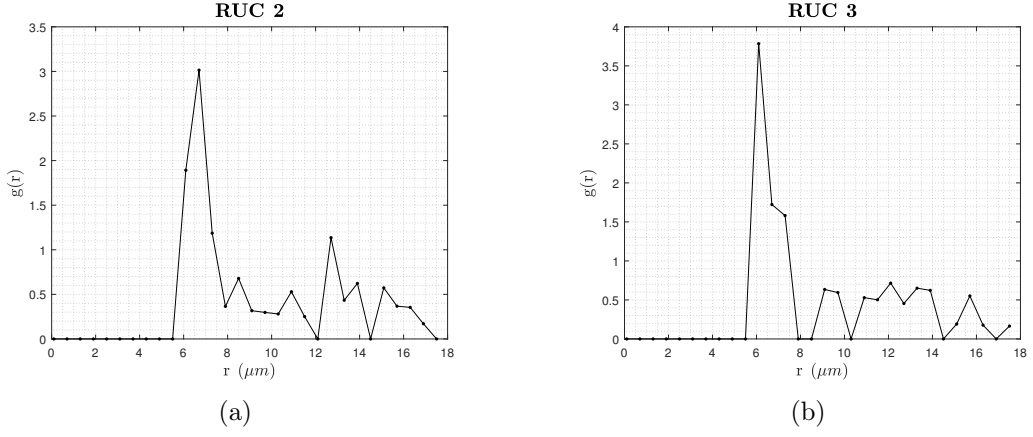


Figure 4.24: Radial distribution function for RUC #2 and RUC #3

Differently from what happened for the five-fibers RUC, there are fewer zeros throughout the entire function. Moreover, the curve begins to be different from zero even for $r < d_f$: this behavior is not due to fibers overlapping, which, as we can see from the representation of the RUC and from the other functions, does not happen but depends on the mesh of the distances into the script. By choosing a more dense mesh, as we did, the radial distribution of the cell is well characterized but the first annular region which includes a fiber center is that one after $r = 5.8 \mu m$. So, MATLAB connects with a straight line $g(r = 5.5 \mu m) = 0$ to $g(r = 6.1 \mu m) \neq 0$ (considering a $dr = 0.6$) and this results in a tract of the curve greater than zero when it is supposed to be zero. A solution can be introduced using $dr < 0.6$ but this will increase the number of zeros and the value of $g(r)$, which would be best to avoid.

That said, the results of the two functions are strictly influenced by the low number of fibers but they seem similar to that obtained from Sanei et al. [35]: the value of $g(r)$ is variable around 1 for the RUC 2, which reflects a more random arrangement and a more variable fiber's density, while the average value for the RUC 3 is smaller and more constant, which reflects a more regular pattern and a constant density.

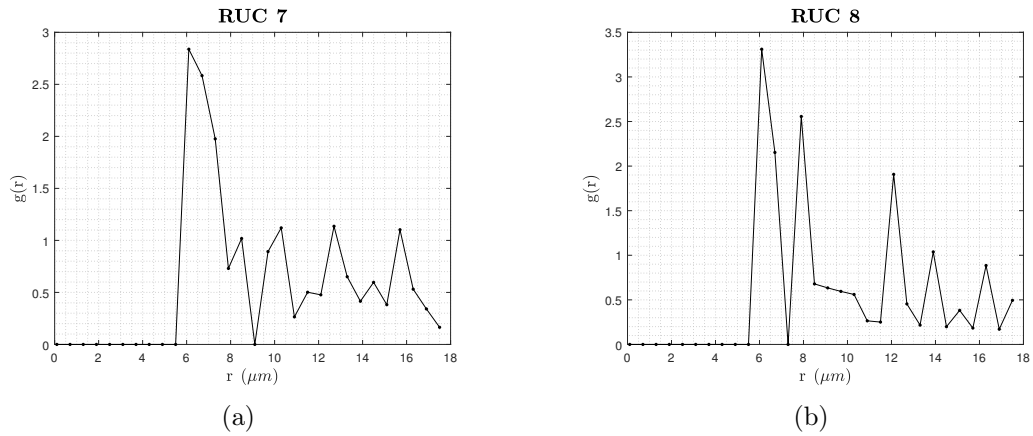


Figure 4.25: Radial distribution function for RUC #7 and RUC #8

In the same way, the behavior of the RUC 7 and 8 is different and it defines two types of unit cell. For the n^o 7, the function assumes a trend with the local maxima having the same value for high distances while the first peak is larger than usual: in fact, looking at the fiber arrangement, we can see some fibers clustered in the center of the cell and a regular pattern of the fibers on the edge of the section. The RUC 8 instead shows a set of decreasing and narrow local maxima, reflection of a lower degree of clustering and a greater average inter-fibers distance.

At last, there is the n^o 9. Repeating what was possible to say looking at the other descriptors, this RUC has a highly random fibers arrangement, because of the fibers arranged all along the edges which leaves a lot of space in the center of the cell who can be randomly occupied by the fibers.

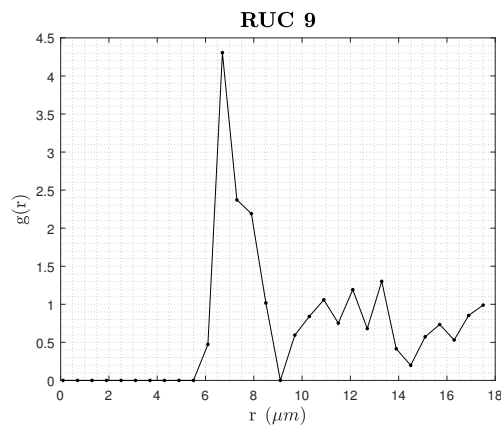


Figure 4.26: Radial distribution function for RUC #9

The result is a curve which shows an unitary asymptote: remembering the Poisson distribution, defined in Pyrz [31], who is the most random arrangement that can be obtained and who has an identically unitary value of $g(r)$, the approach of this RUC's function to the Poisson distribution is indicative of a high degree of randomness which, obviously, will affect the strength of the cell because of the stress and strain field highly variable.

4.4.3 Thirty-fibers RUCs

The last step is made by the statistical analysis of the thirty-fibers RUCs.

Nearest neighbor distribution function The first descriptor used to characterize the short-range interaction between fibers is the nearest neighbor distribution function. Five RUCs were been described in this section, in order to show as much as possible different characteristics: they are identified by the number 1, 4, 6, 9 and 10.

The first one described is the n^o 1, who contains exactly thirty points of observation. The nearest neighbor distance more frequent is the smaller one, $r = 6.5 \mu m$, that, with other two values around this one, in particular $6.6 \mu m$ and $6.7 \mu m$, monopolizes the distances evaluated. Because of the high number of fibers inside the cell, in fact, the fibers are distributed so as to be near and the result is that higher distances are less frequent.

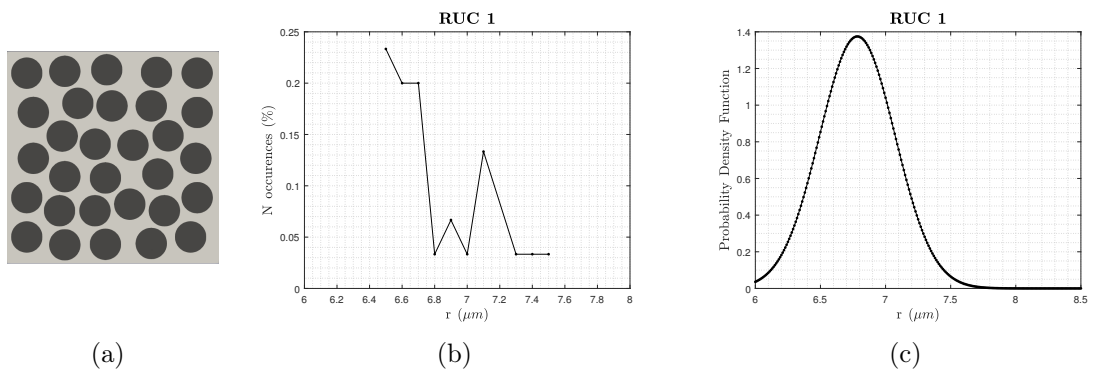


Figure 4.27: Thirty-fibers RUC #1 and relevant nearest neighbors distances and distribution function

A frequent small distance will affect the strength of the whole composite material. Since the local stress increases where there is shorter inter-fiber space, such a high number of fibers close to each others, will increase the strain and facilitate the crack initiation. The resulting probability density function exhibits a peak in correspondance of the most frequent values, approaching to zero after $7.5 \mu m$, who is the last value of the nearest neighbor distance measured.

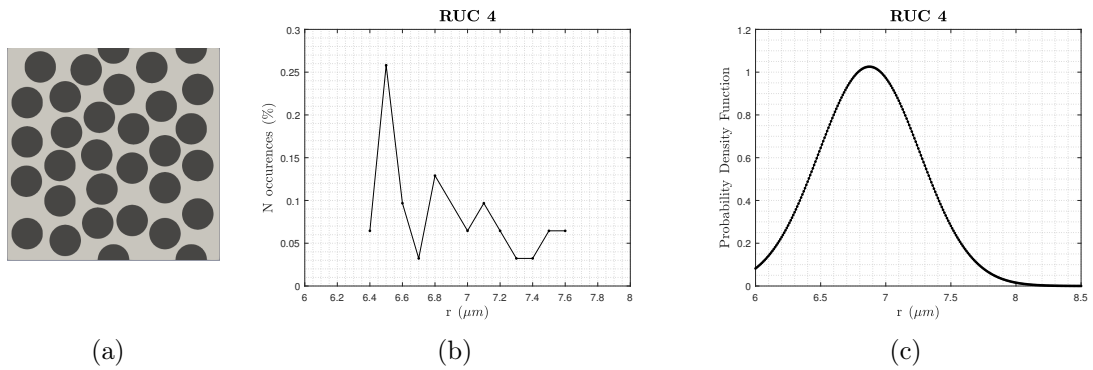


Figure 4.28: Thirty-fibers RUC #4 and relevant nearest neighbors distances and distribution function

This second case is referred to RUC 4 and, looking at the Fig.4.28(b), it is easy to understand that this unit cell has a higher degree of randomness. Even though the same distance $r = 6.5 \mu m$ is the most frequent, with 8 events out of 32 points of observation, this RUC have a wider range of values in which the number of occurrences' curve of the nearest neighbor distance distributes and, in general, everyone of this value appears a few times in respect to the total. It is possible to extrapolate the same informations looking at the probability density function who has a lower maximum and it is wider. So, the fibers are distributed more randomly than in the previous section: nevertheless, this is not sufficient to figure out wheter the strength will be greater or lower.

This third example can seem similar to the previous one, at first sight, but, actually, the maximum percentage of the number of occurrences is higher for this RUC and a lower range of distances results from the analysis. So, the probability density function is stretched around $6.7 - 6.8 \mu m$, with a maximum value higher than the previous examples.

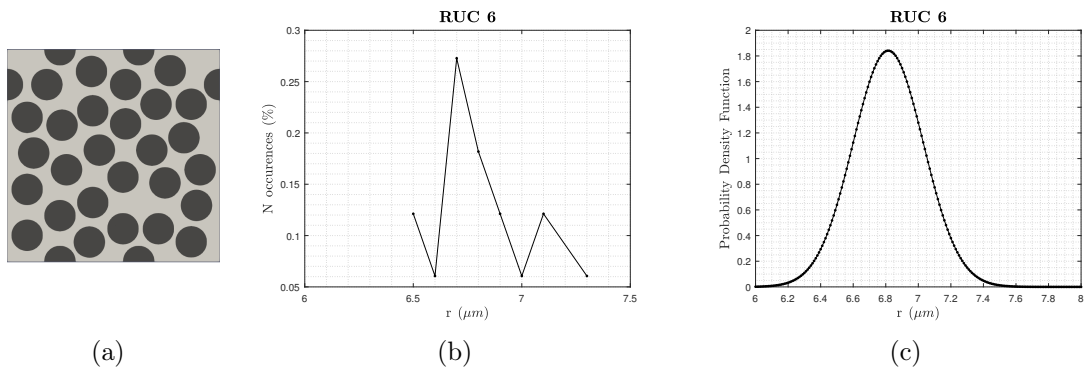


Figure 4.29: Thirty-fibers RUC #6 and relevant nearest neighbors distances and distribution function

A situation like this one is indicative of a regular inter-fibers distance distribution which does not mean that the spatial point distribution is regular, since there are no informations about the orientation of the closest neighbor.

The fourth case is the RUC 9 who contains 38 points of observation. This high number of points is the reason why the curve in Fig.4.30(b) has a maximum between 30% and 35%, which corresponds to 12 events out of 38: the RUC does not present a regular spacing for the inter-fibers distance, in fact the remaining 26 occurrences are divided in a range who varies between $6.5 \mu m$ and $8.8 \mu m$, more than any other example made until now.

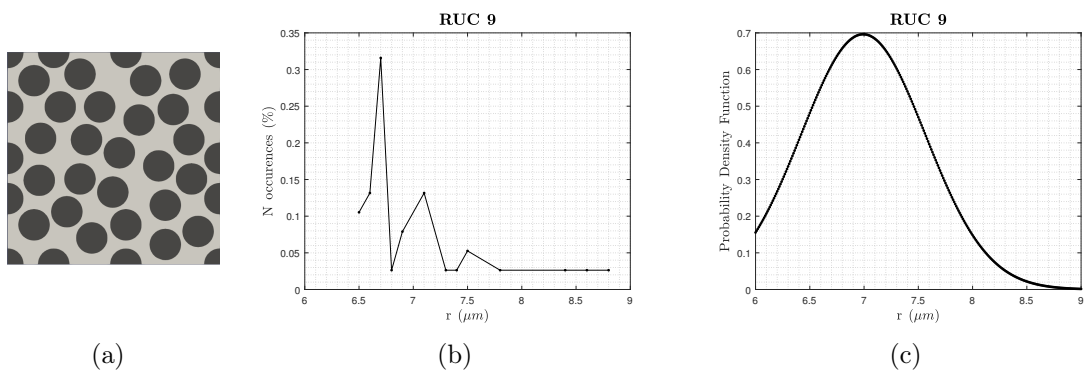


Figure 4.30: Thirty-fibers RUC #9 and relevant nearest neighbors distances and distribution function

The litmus test of this behavior is, as always, the probability density distribution function. The absolute maximum of the function is relatively and the function covers the same range of distance that we said before. So, it is clear that the inter-fibers

distance's distribution is anything but regular and, as it turns out looking at the representation of the repeating unit cell in Fig.4.30(a), in the cross-section there is a good alternation of clustered fibers and void spaces.

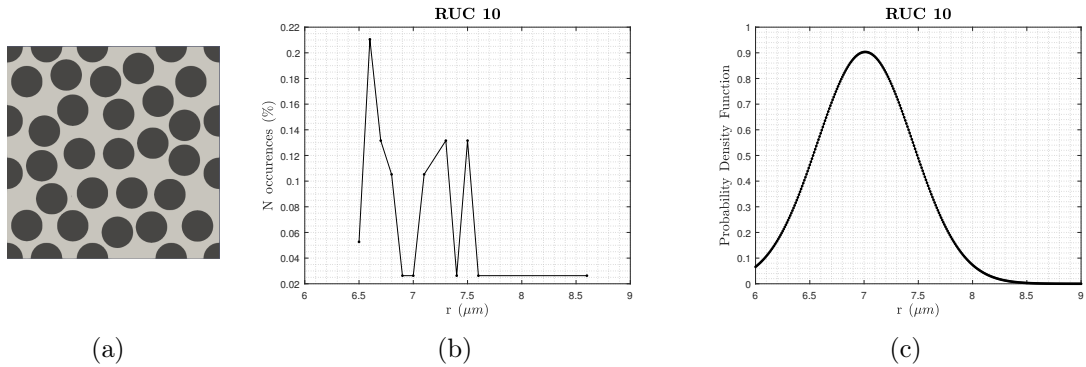


Figure 4.31: Thirty-fibers RUC #10 and relevant nearest neighbors distances and distribution function

The RUC n^o 10 is defined by the same amount of points but, however, even though the arrangement of fibers can look similar, a different behavior in terms of short-range interaction is exhibited. First of all, the distances evaluated for the nearest neighbors varies in a less wide range; then, looking at the local maxima, for this example there are many distances which occur frequently, not only the distance relative to the absolute maxima. This means that the average behavior of the fibers arrangement is more -regular than the RUC 9, even though we do not know yet how this will affect the resistance of the whole material. The resulting probability density function curve is more narrow and has a greater maximum value.

Second-order intensity function It is important to specify that the values reached by the function are rather high compared with those who results from literature: this is because of the value of w_k , the correction factor, which is low in our study because of the small dimensions of the RUC. For this reason, part of the circumference used for the analysis, as the radius become higher, quite often is outside of the cell, which means that $w_k < 1$ causes the value of $k(r)$ to increase. On the same basis, the evaluated distance is stopped to low values in order to have useful values of this factor. However what was said will not influence the general trend of the curve, which is the subjective of the study.

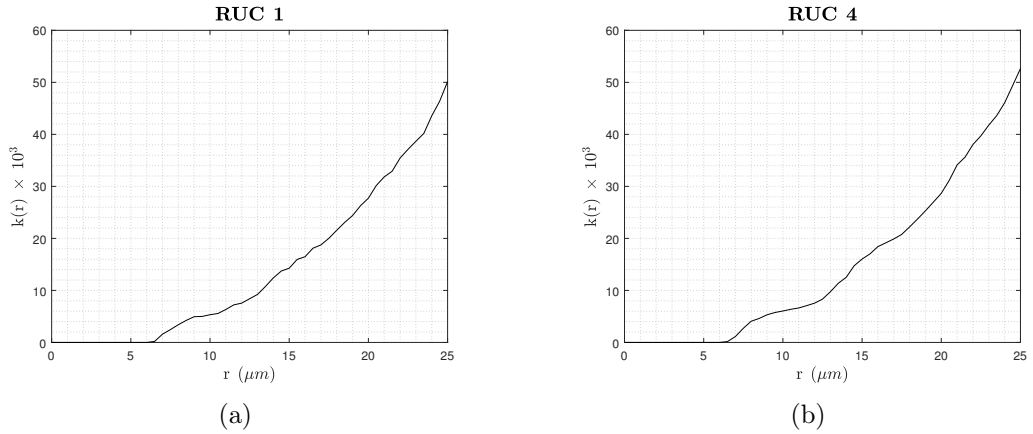


Figure 4.32: Second-order intensity function for RUC #1 and RUC #4

As we can say looking at this two figure (see Fig.4.32), since the number of the fibers contained in every RUC is increased, the shape of the curve is smoother and similar to those one in [32], concerning actual materials. The trend is the same for both the cases for short- and long-range, i.e. short and long distances, while the value of $k(r)$ seems so to be a little different in the central part of the curve: in particular, the k -function is greater for the RUC 4, which means that there is a region, in the cell, where the fibers are a little more clustered than in the RUC 1. This can modify the behavior under load of the composite material and it will be more clear after the micromechanical analysis of the structures. In the end, the different final value reached by $k(r)$ for $r = r_{max}$ substantially differs by a little amount between the two unit cells because of the greater number of points of observation contained in the second RUC.

In the following figure, Fig.4.33, is set out the second-order intensity function for the three RUCs specified. Since the trend is almost similar for the three cases, it is possible to think that, with a greater number of fibers inside every unit cell, the degree of randomness reached is sufficiently high to let us assimilate the spatial point pattern to the hard-core distribution seen in [32]. This distribution is the most random possible taking into account the finite dimension of the fibers, feature who lead to exclude every position distant less than the fiber's radius from another point already placed.

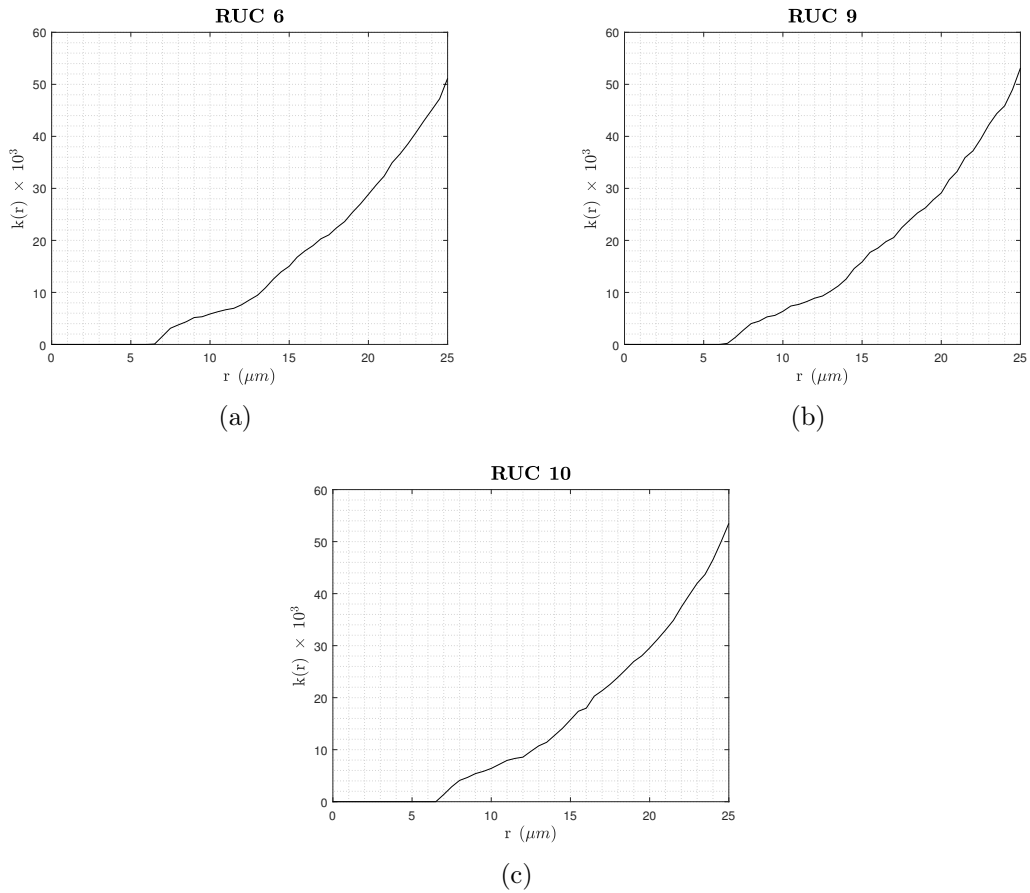


Figure 4.33: Second-order intensity function for RUC #6, RUC #9 and RUC #10

Nevertheless there are a few differences between the three curves: the first one is the maximum value who is greater for unit cells with more points of observation; moreover, looking at the curve for the RUC 10, it is possible to notice two small stairs, who define an empty region at the relevant distances from every fiber's center.

Radial distribution function Finally, the third statistical descriptor, necessary to figure out the average fiber density variation, is shown. As done with the previous unit cells with five or ten fibers, a $dr = 0.6 \mu\text{m}$ is chosen as compromise to have few zeros all along the curve and to well characterize its average behavior. As the number of fibers increases, the value of the descriptor, after the first high peak, is getting closer to the unit, as we can expect for $r \rightarrow \infty$, since $N_A = N/A$ becomes representative of the entire cell.

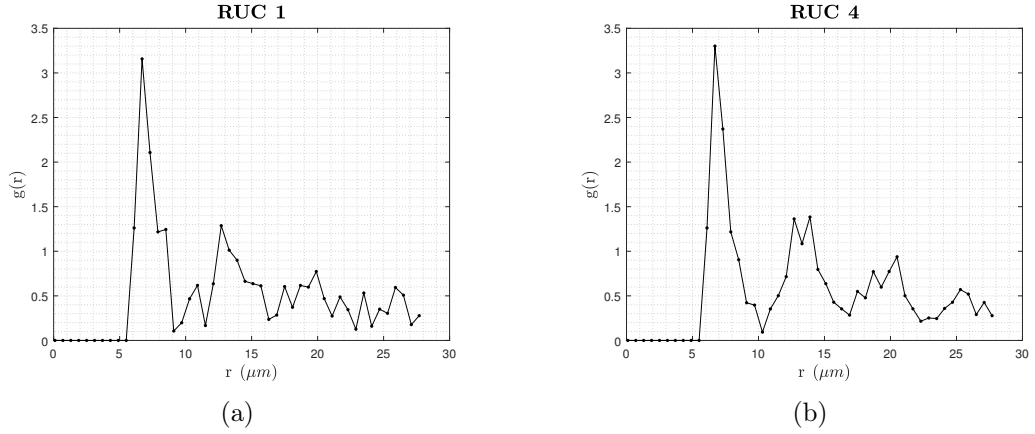


Figure 4.34: Radial distribution function for RUC #1 and RUC #4

However, when the value of $g(r)$ is greater than 1 this means that the relevant inter-fibers distance is more frequent than in case of complete randomness, i.e. the Poisson distribution.

For the RUC 1 (Fig. 4.34(a)) we can see a more regular behavior of the average fiber density, since after the first two peaks, as the radius increases, the radial distribution function shows less and less frequent events; on the contrary, for the RUC 4 (Fig. 4.34(b)) it is possible to notice that a greater number of spikes occurs, indicative of a more variable behavior and, for this, a greater degree of randomness. In the end, as always, the function approaches to zero, since the annular region will be entirely outside of the unit cell and this means that no fibers are inside of it. Then, the RUC 6, 9 and 10 (Fig. 4.35) are analyzed. The biggest difference between the first unit cell and the following two is the shape and the value of the first peak. As we could imagine from the nearest neighbor distribution function but it is clearer here, a large number of fibers are characterized by a particular distance between the fibers since the function assumes a high value in correspondance of this specific distance; on the contrary, the two spikes for the RUC 9 and 10 reach a lower value and they have a larger shape. This means that, even if in the cell there are more points of observation and in percentage the number of events is greater compared to the most frequent distance of the sixth RUC, here the average distance between the fibers assumes two specific values for every unit cell: that is why the peak is larger and smaller.

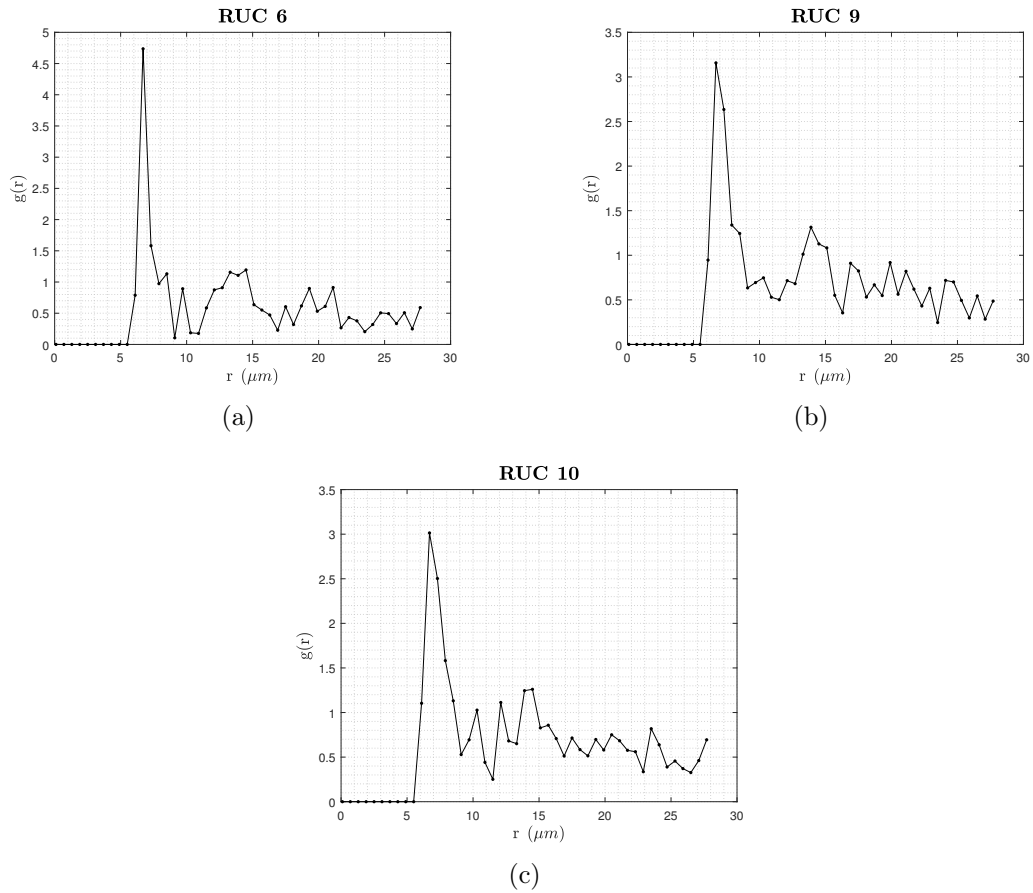


Figure 4.35: Radial distribution function for RUC #6, RUC #9 and RUC #10

The remainder of the function is similar for the three, defined by a usual fluctuation around a value a rather smaller than 1 and, in the end, for the same reason specified for the previous case (see Fig.4.34), the approach to zero as the annular region falls out of the unit cell.

What was said characterizes to a large extent the pattern of the fibers inside the RUCs described. In fact, it was possible to define, as it was repeated many times, the short-, medium- and long-range interaction between fibers and the average density of the reinforcement phase: so, the work done so far is an absolute starting point to relate the stiffness and the strength of a composite material to its microstructure, who is largely influenced by the working process.

Chapter 5

Failure Analysis of the RUCs: conclusions

The purpose of the analysis conducted so far is the evaluation of the failure, in terms of strength, of the repeating unit cells and its possible connection with the degree of randomness defined by the fiber pattern.

The computational instruments that are usually used to simulate the failure of the composite materials, requires generally a high computational cost, which translates in a high time necessary to perform the analysis. The use of the Carrera Unified Formulation, as demonstrated by de Miguel et al. [25], can reduce significantly the degrees of freedom, performing a comprehensive evaluation of mechanical problems in reduced time.

Preliminary results are obtained using the traditional finite elements method and the commercial software Abaqus has been used to carry out progressive failure analysis simulation. However, to reduce the computational cost of the analysis, the use of the Carrera Unified Formulation will be a stimulus for future works.

5.1 Failure Analysis

The failure analysis has been conducted applying a force in the direction of the x axis. The results of the application of this force is a deformation of the cell in

the same direction, which tends to stretch: this elongation causes a variation in the stress and strain fields of the model and stress increases. This phenomenon is caused by the proximity of the reinforcement phases, who is significantly more resistant compared to the matrix, and the smaller the distance, the higher the stress in the area. For this reason, in this same area, the matrix should sustain a high load and, being this phase weak, with a low critical stress σ_{cr} , i.e. the stress which causes the failure of the material, a crack begin and tends to propagate all along the dimension of the cell causing, eventually, the breaking of the material.

In the stress-strain curve, it is possible to see a peak and then a decreasing trend. If the crack propagates for the entire section and the material is no longer able to resist, the curve goes to zero, while, if conversely there is a resistant part left, the curve increases again until the crack is completed, i.e. the stress decreases to zero. The absolute *maximum* in the stress-strain curve is the strength of the material, σ_{ult} : it is the maximum value of the stress applicable to the model which causes a fracture.

5.2 Results on five fibers RUCs

The first type of RUC renditions analyzed contains five fibers as was described before. It is shown the crackpath for 8 renditions in order to differentiate the behavior of the cells.

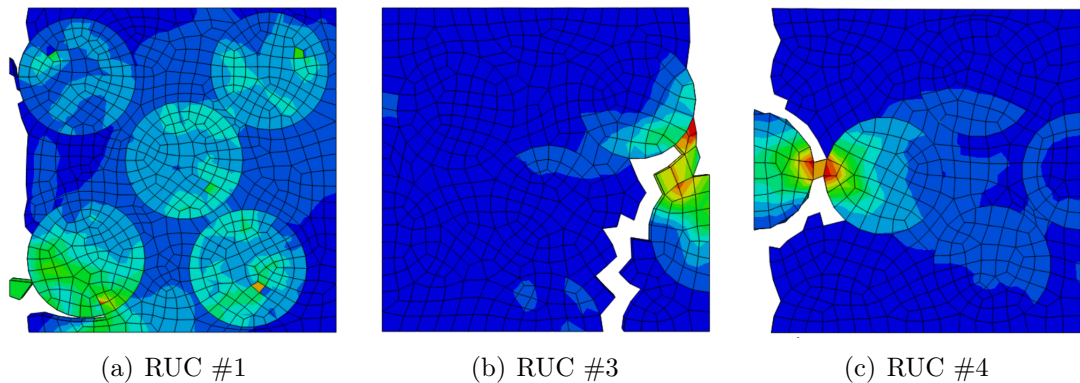


Figure 5.1: Crackpath for RUCs #1, RUC #3 and RUC #4

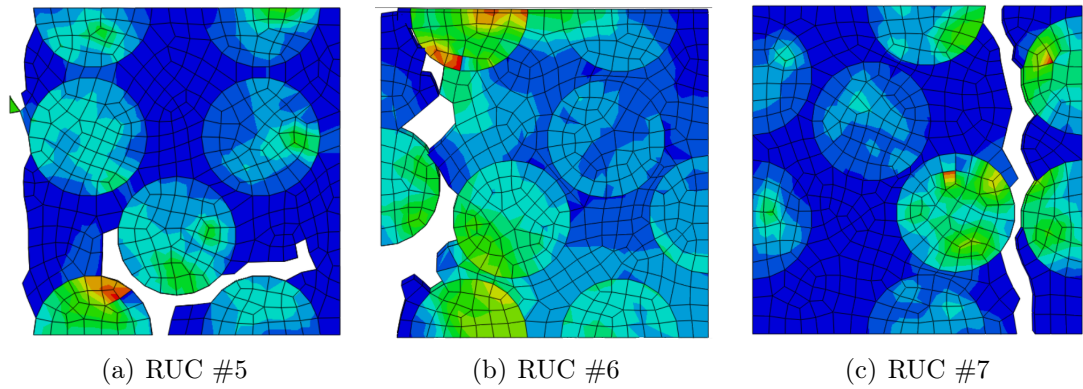


Figure 5.2: Crackpath for RUCs #5, RUC #6 and RUC #7

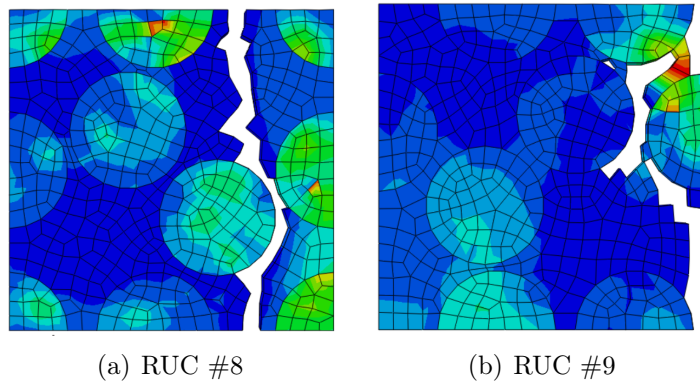


Figure 5.3: Crackpath for RUCs #8 and RUC #9

In some RUCs the failure of the cell happened in the boundary region: that ones which present a failure not influenced by the fibers' number are the RUCs 6, 7 and 8 and for this models the stress-strain curve was derived and related to the statistical analysis previously made.

First of all, the stress field is showed, to understand where the crack begin and what is the reasons for which the stress is concentrated.

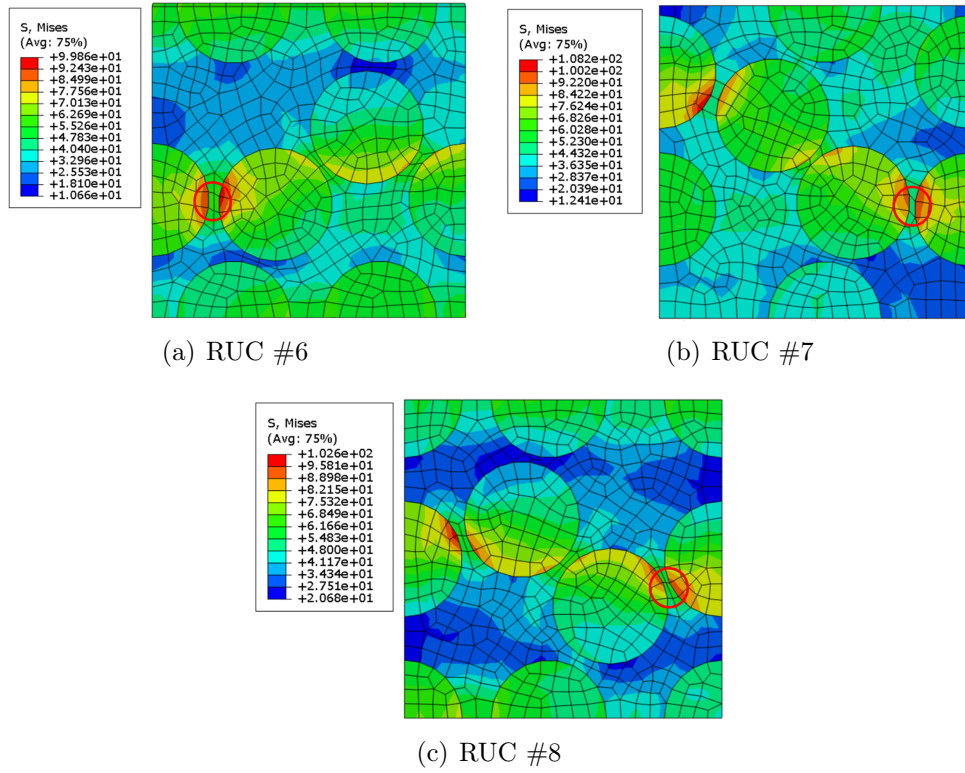


Figure 5.4: Stress field for RUCs #6, RUC #7 and RUC #8

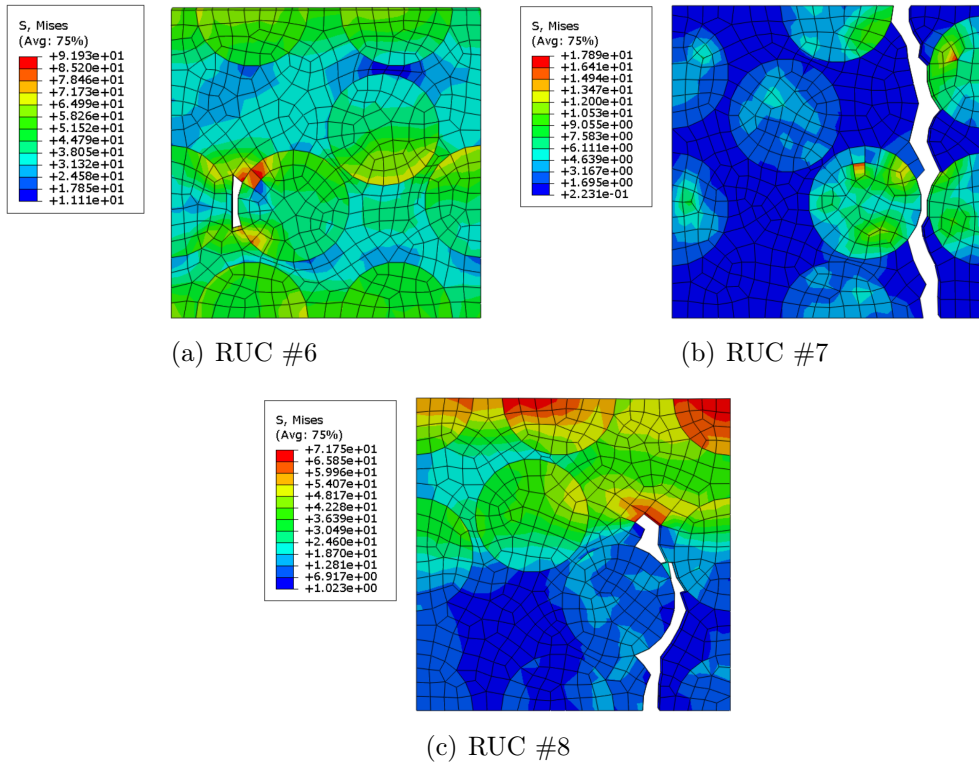


Figure 5.5: Crack initiation for RUCs #6, RUC #7 and RUC #8

In Fig.5.4 is highlighted, with a red circle, the region where the stress is higher, for both the matrix and the fibers and where the crack will begin. It is possible to notice that, as said before, the concentration of the stress happens in an interface area between matrix and fiber and, in particular, where the distance of two reinforcement phases is low. To confirm what was said, it is also shown the moment when the crack begins.

The initiation of the crack is different for the three RUCs (Fig.5.5): for the number 6 just a couple of elements fails, decreasing the resistant section of a small amount. The RUC 7 has an instantaneous growth of the fracture: for the same value of the applied load, the failure begins and run through the entire section, causing the failure. The result of this behavior will be reflected in the stress-strain curve, which will decrease suddenly to zero. Finally, the RUC 8 shows that the crack grows suddenly for a certain amount but, before the total failure, some part of the cell will continue to resist.

Appendix A

Record of the Statistical Analysis on the repeating unit cells

In this Appendix, the results of the statistical analysis on every RUC are showed. All the curves obtained are reported with the relevant fiber distribution.

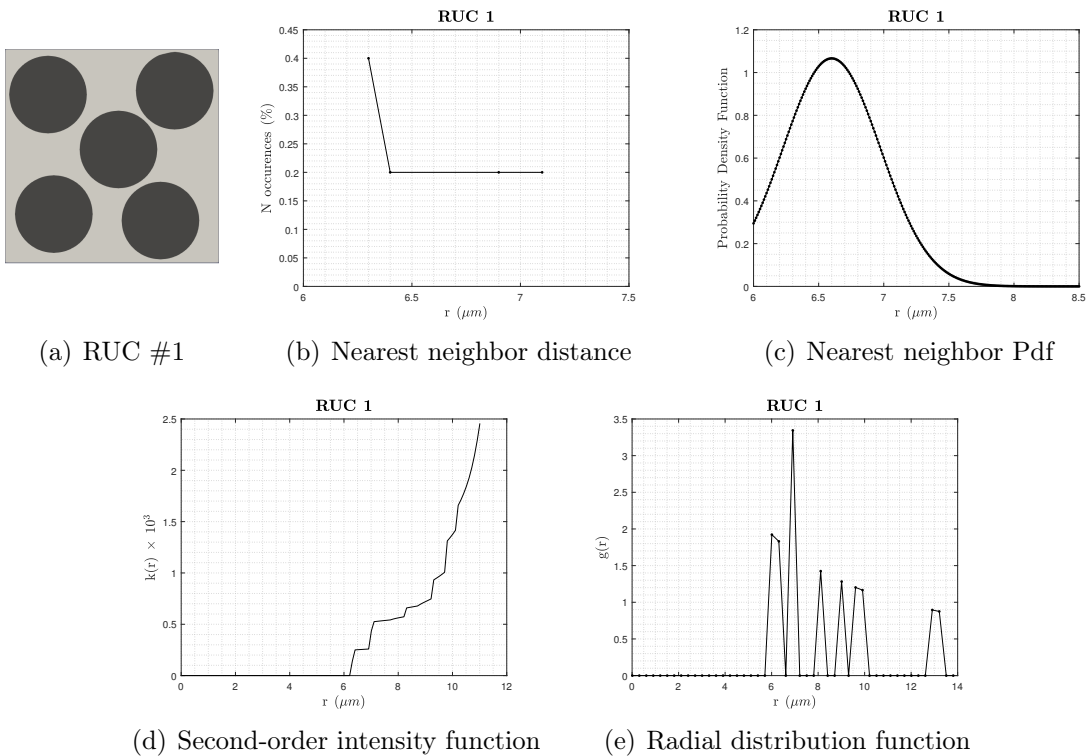
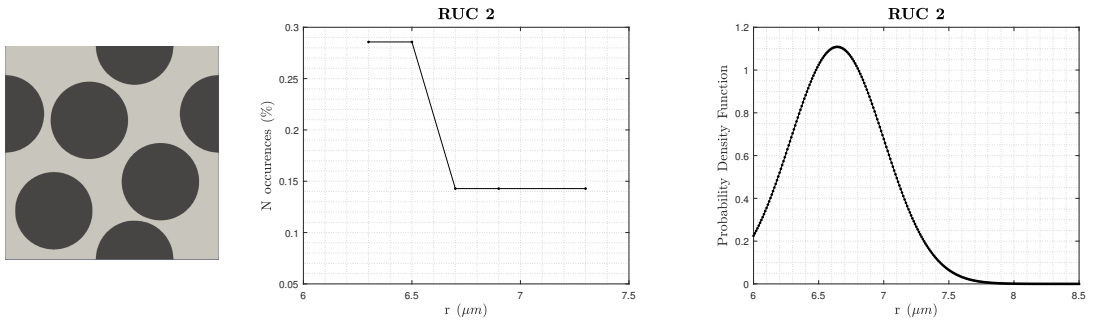
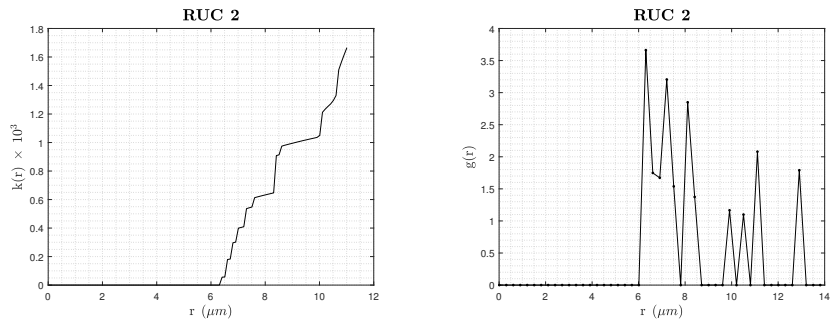


Figure A.1: Five-fibers RUC #1 and relevant statistical descriptors

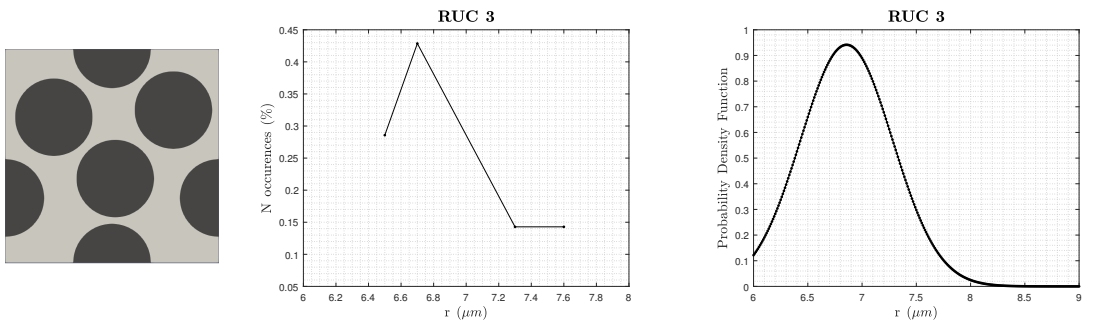


(a) RUC #2 (b) Nearest neighbor distance (c) Nearest neighbor Pdf

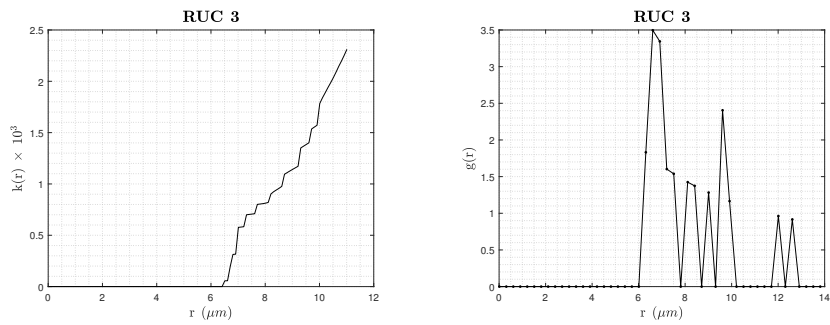


(d) Second-order intensity function (e) Radial distribution function

Figure A.2: Five-fibers RUC #2 and relevant statistical descriptors



(a) RUC #3 (b) Nearest neighbor distance (c) Nearest neighbor Pdf



(d) Second-order intensity function (e) Radial distribution function

Figure A.3: Five-fibers RUC #3 and relevant statistical descriptors

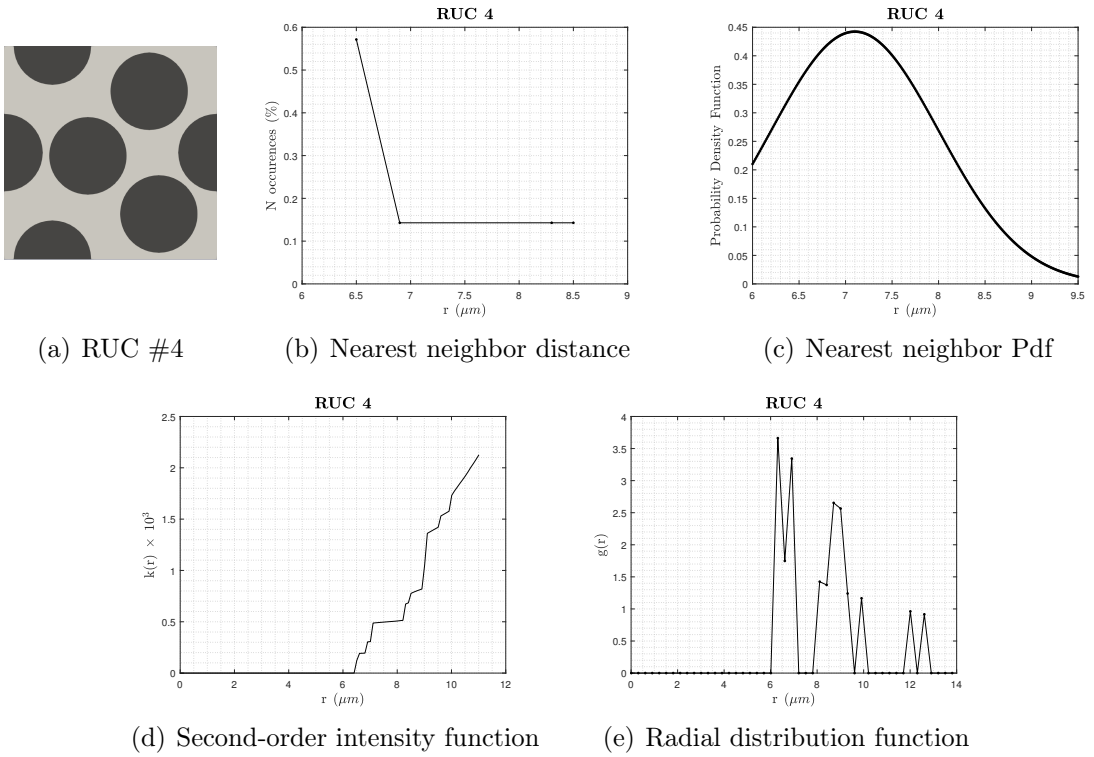


Figure A.4: Five-fibers RUC #4 and relevant statistical descriptors

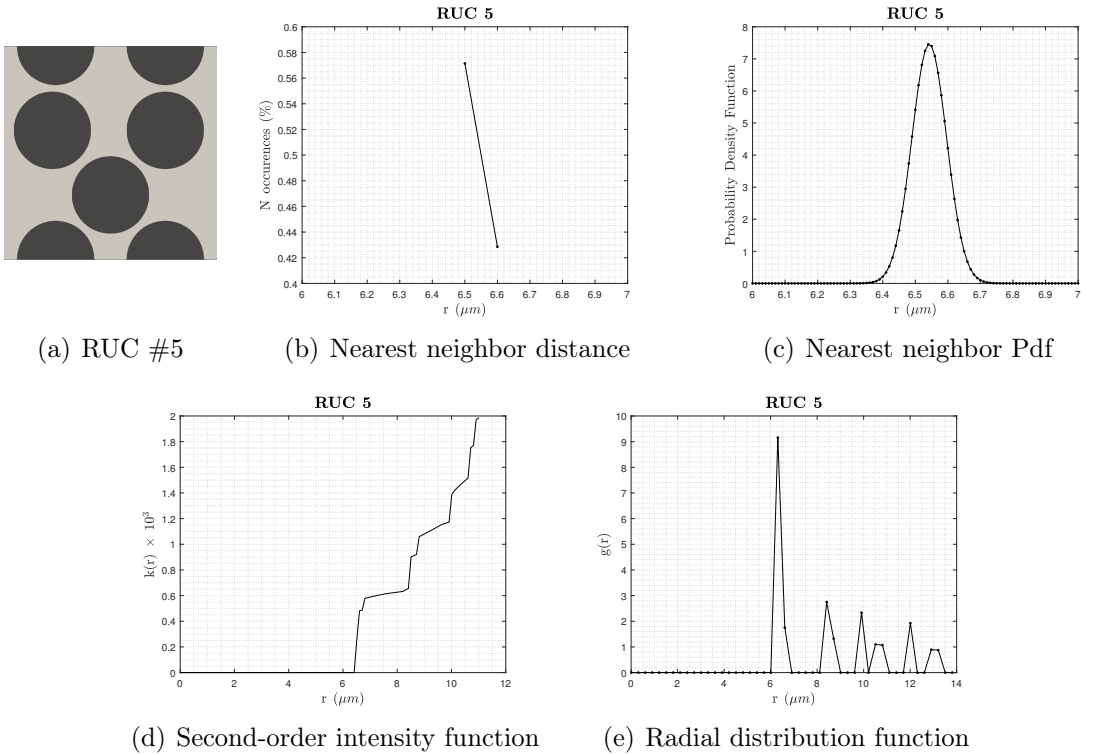


Figure A.5: Five-fibers RUC #5 and relevant statistical descriptors

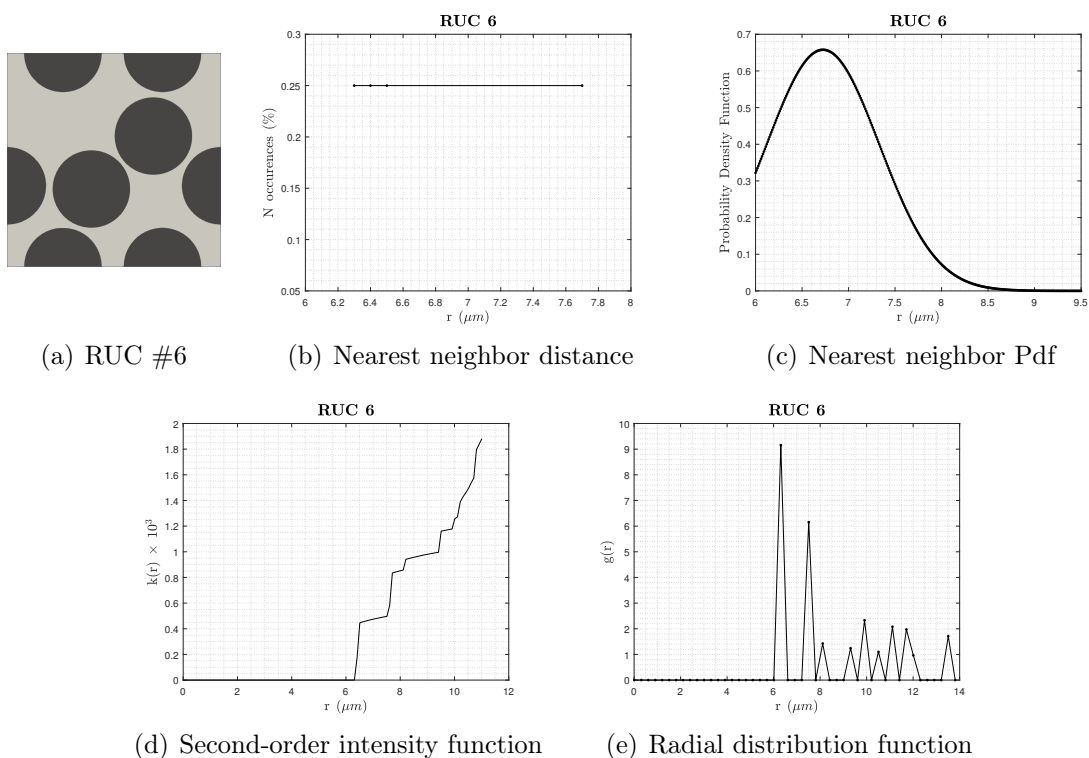


Figure A.6: Five-fibers RUC #6 and relevant statistical descriptors

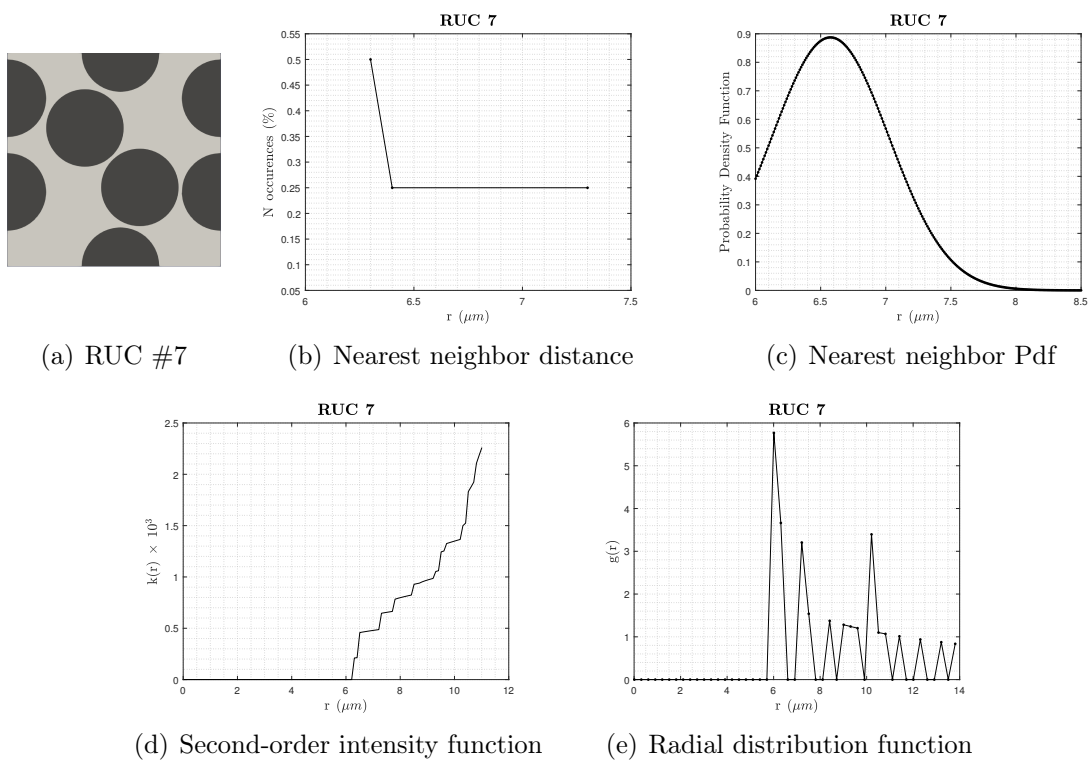


Figure A.7: Five-fibers RUC #7 and relevant statistical descriptors

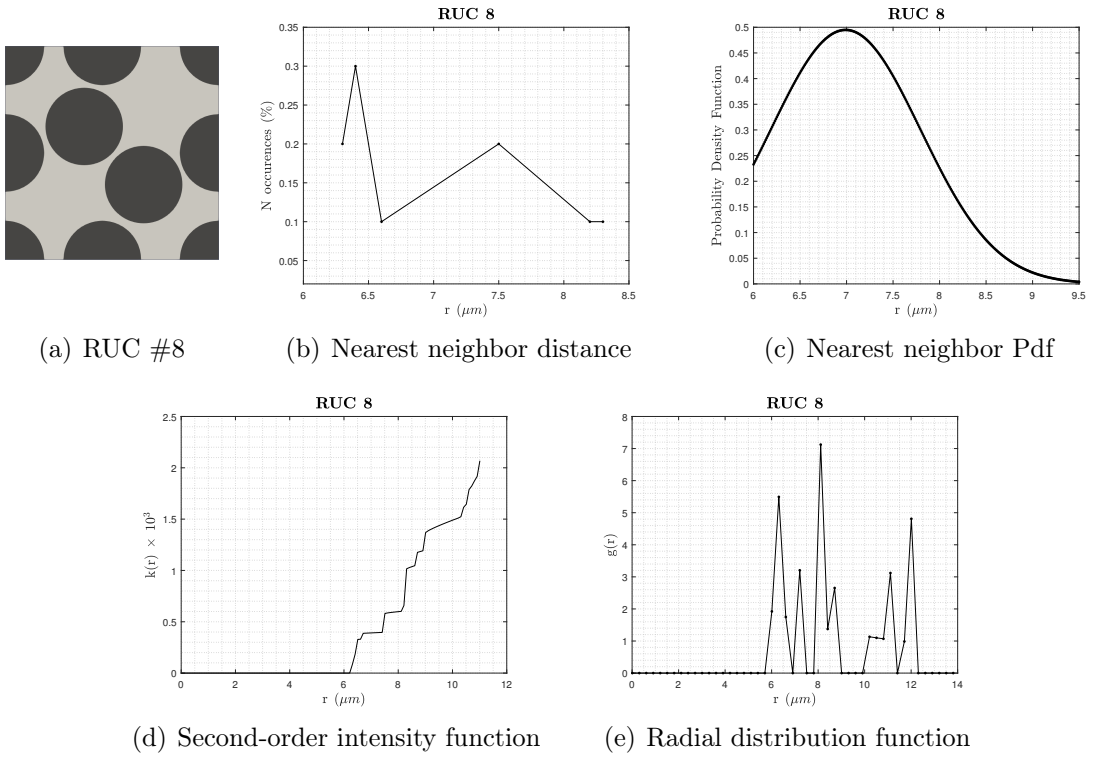


Figure A.8: Five-fibers RUC #8 and relevant statistical descriptors

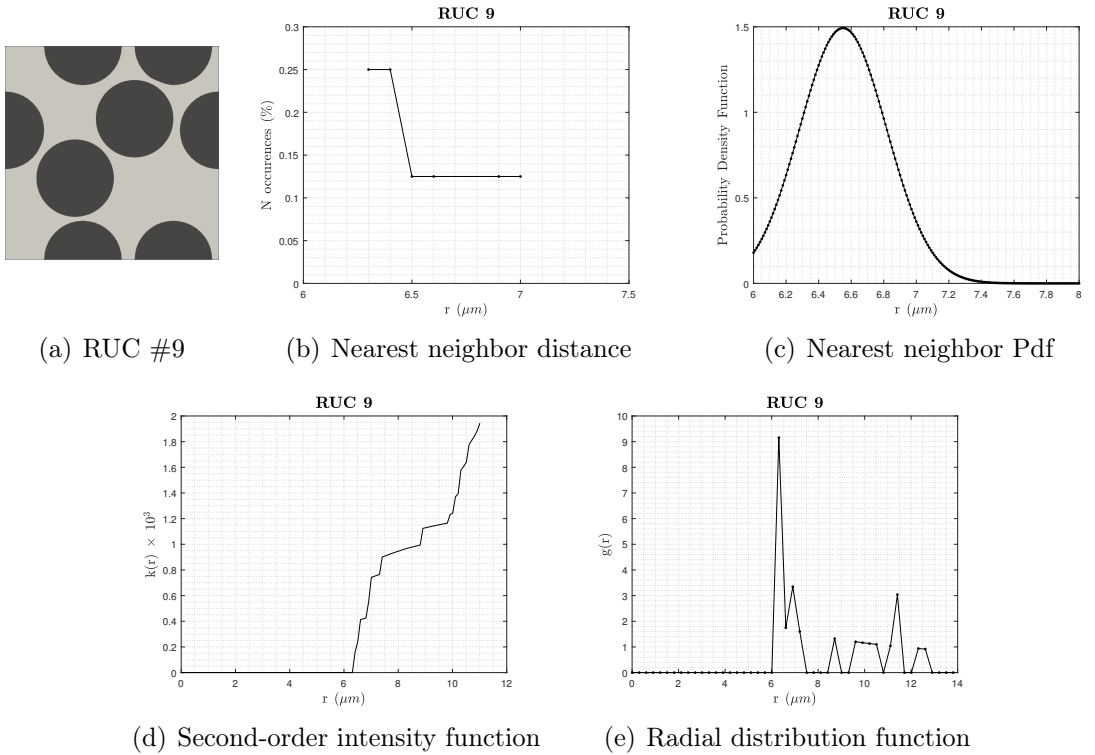


Figure A.9: Five-fibers RUC #9 and relevant statistical descriptors

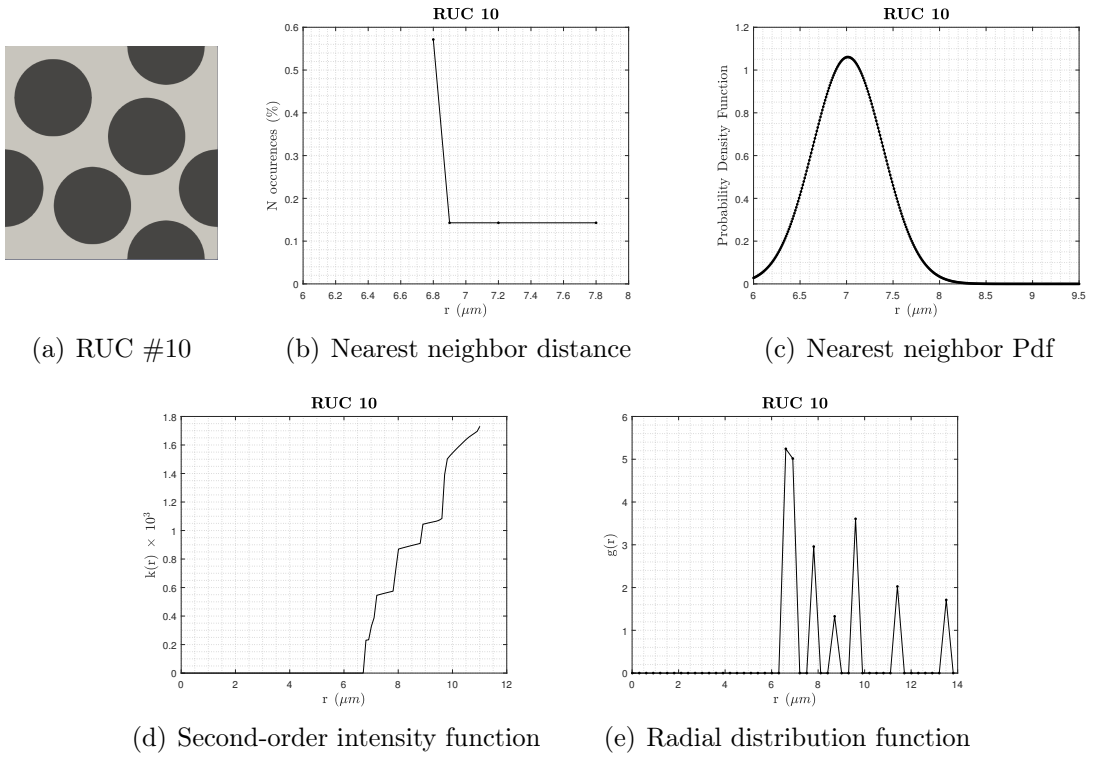


Figure A.10: Five-fibers RUC #10 and relevant statistical descriptors

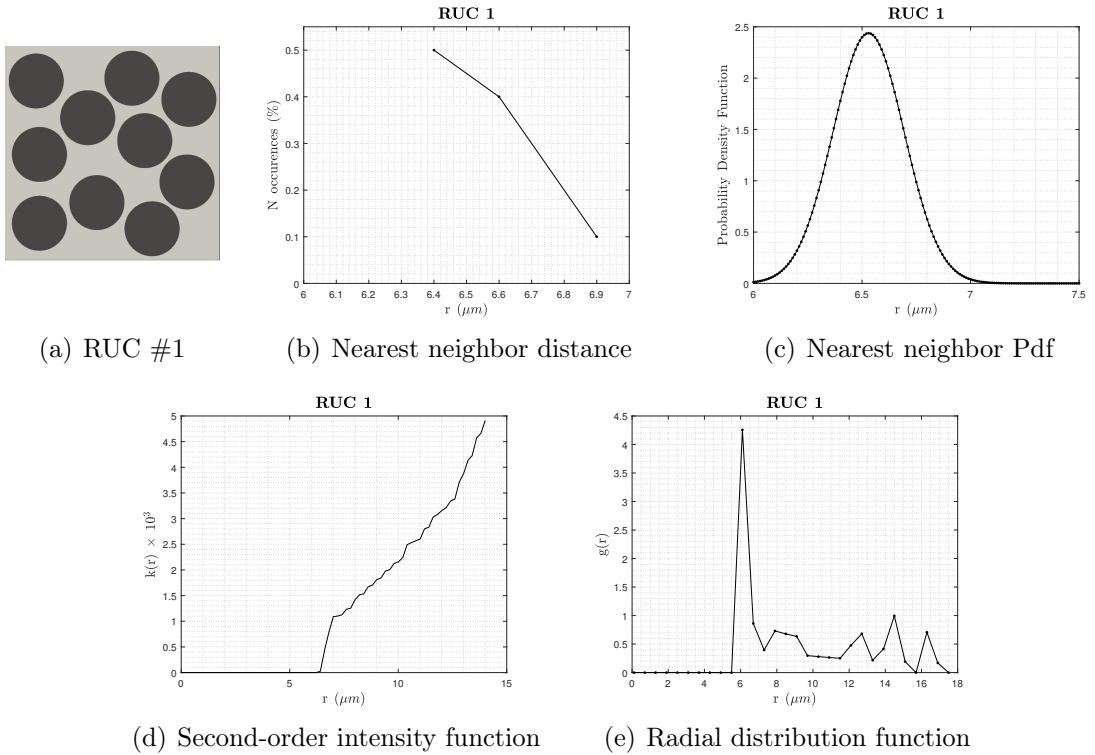


Figure A.11: Ten-fibers RUC #1 and relevant statistical descriptors

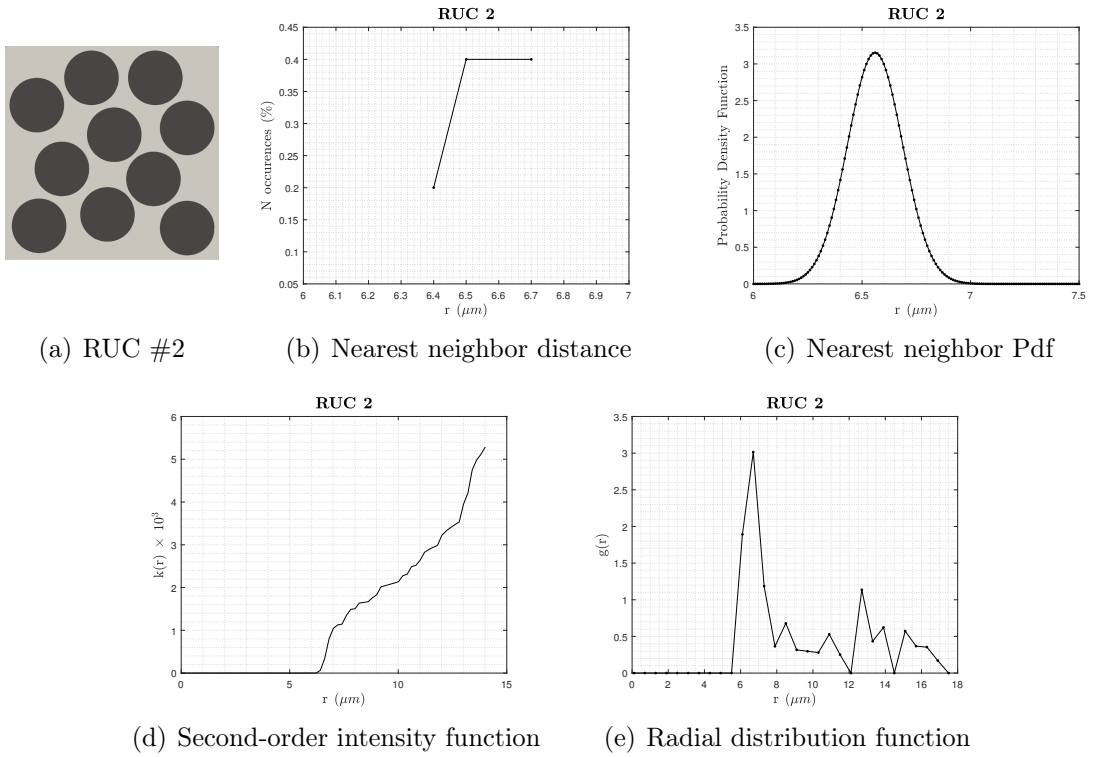


Figure A.12: Ten-fibers RUC #2 and relevant statistical descriptors

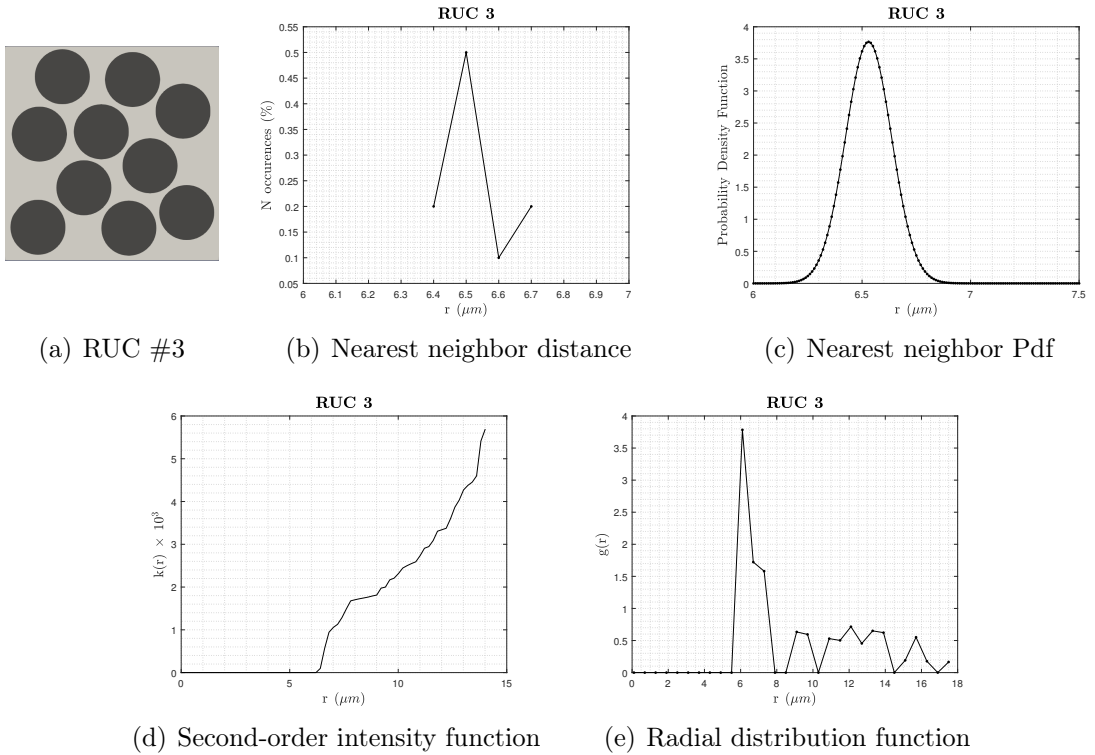


Figure A.13: Ten-fibers RUC #3 and relevant statistical descriptors

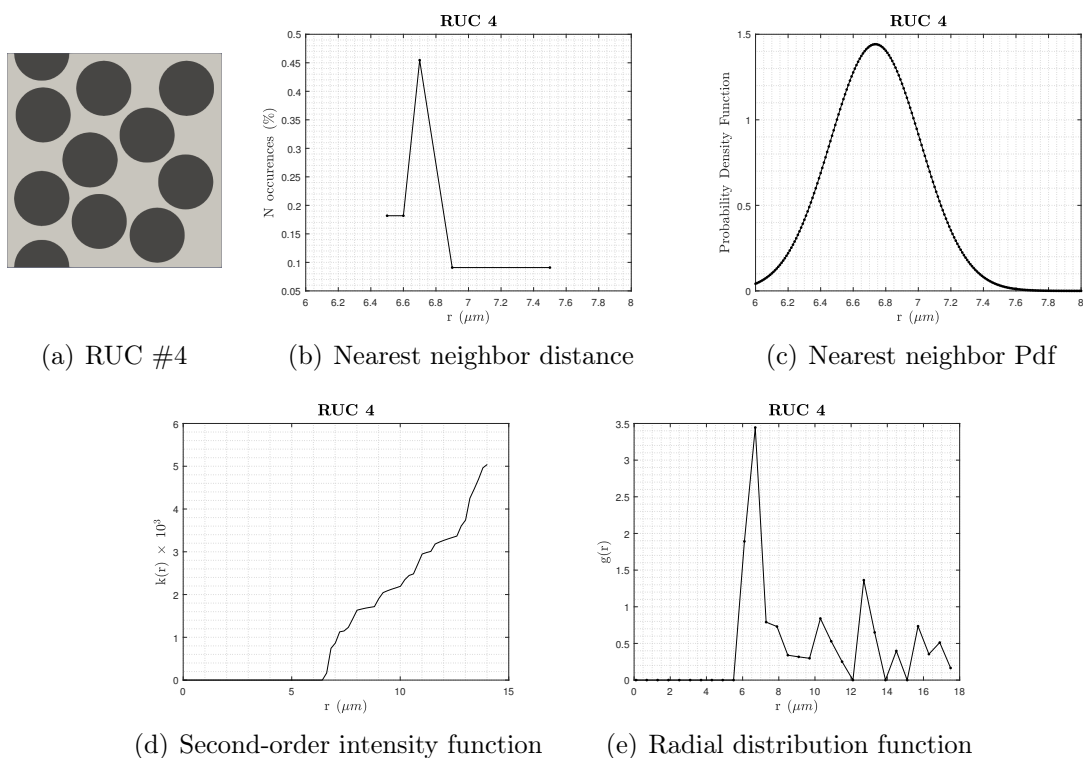


Figure A.14: Ten-fibers RUC #4 and relevant statistical descriptors

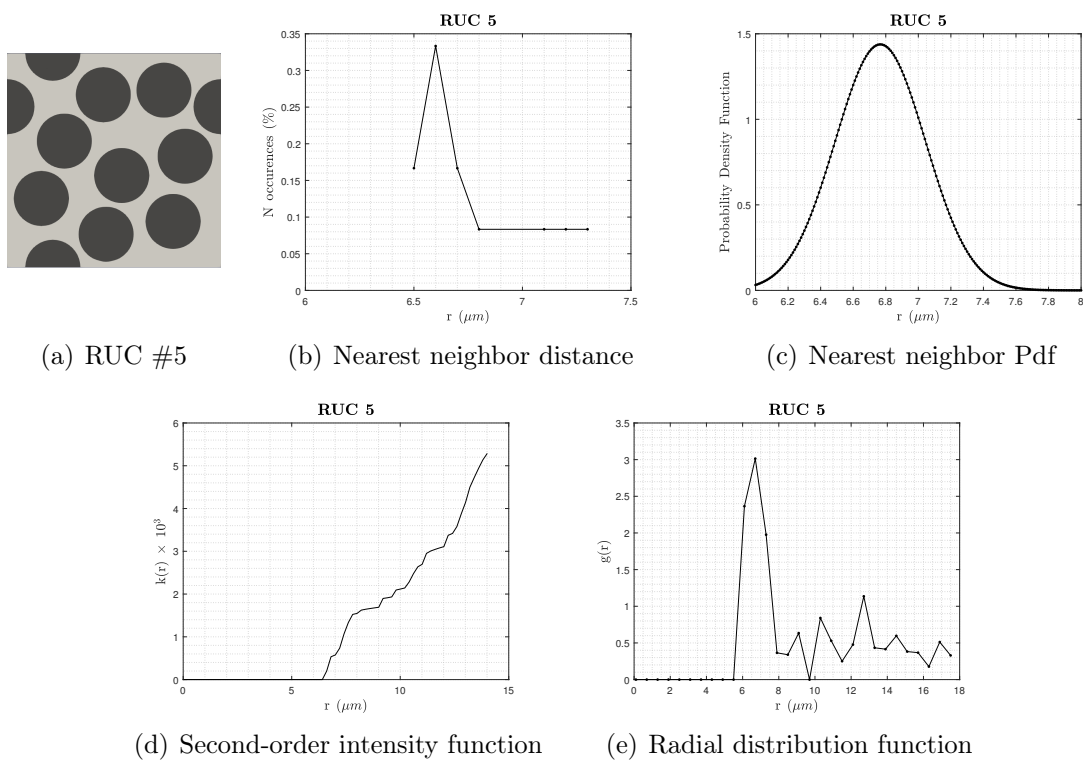


Figure A.15: Ten-fibers RUC #5 and relevant statistical descriptors

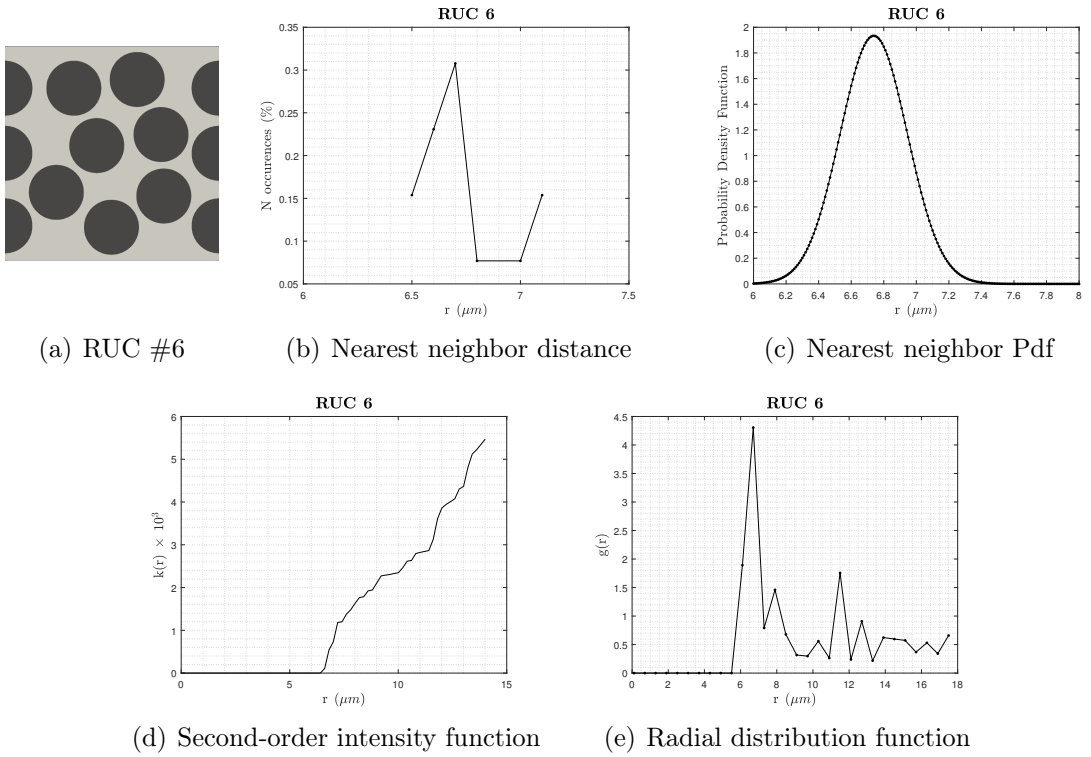


Figure A.16: Ten-fibers RUC #6 and relevant statistical descriptors

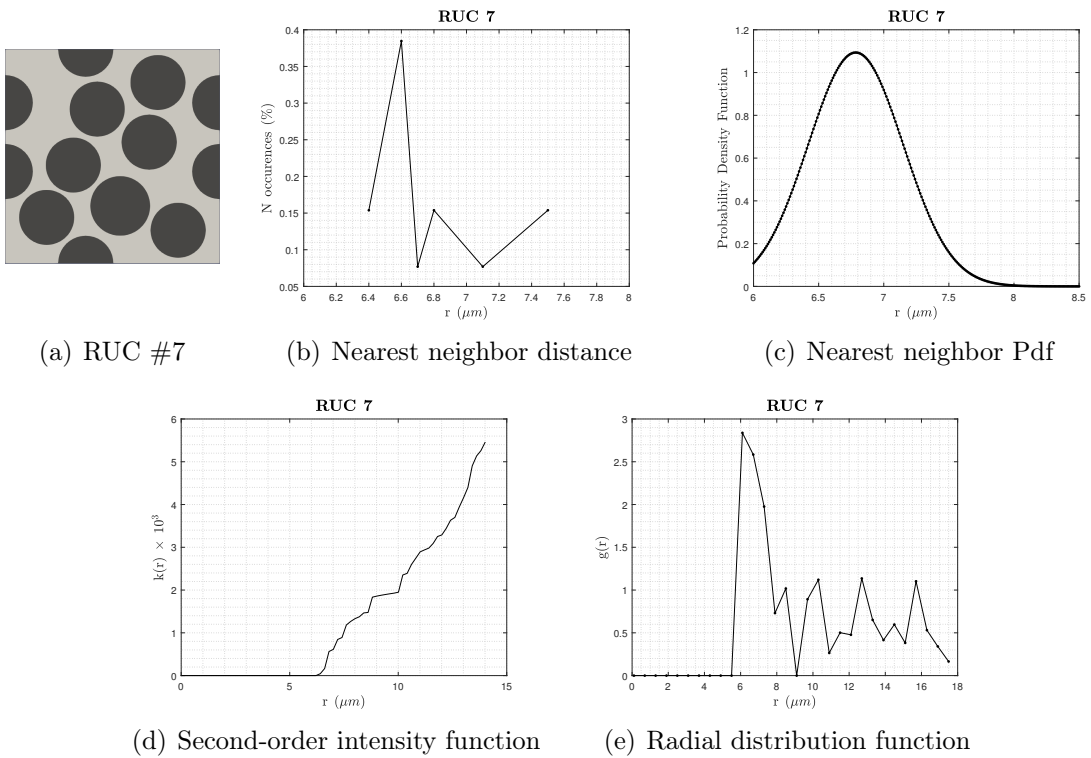
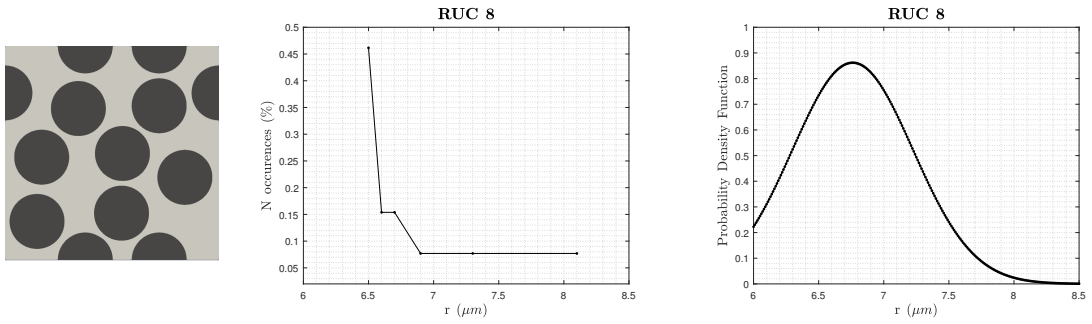
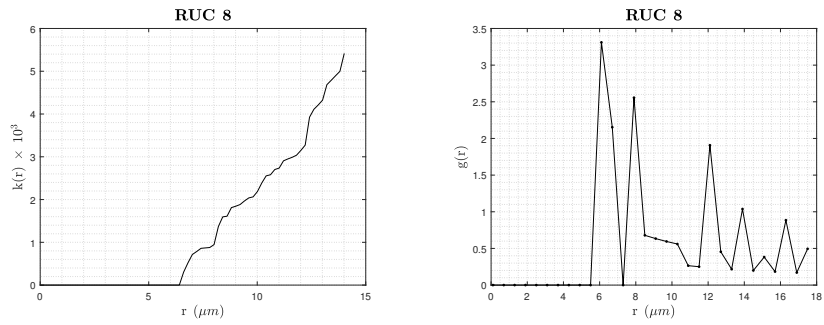


Figure A.17: Ten-fibers RUC #7 and relevant statistical descriptors

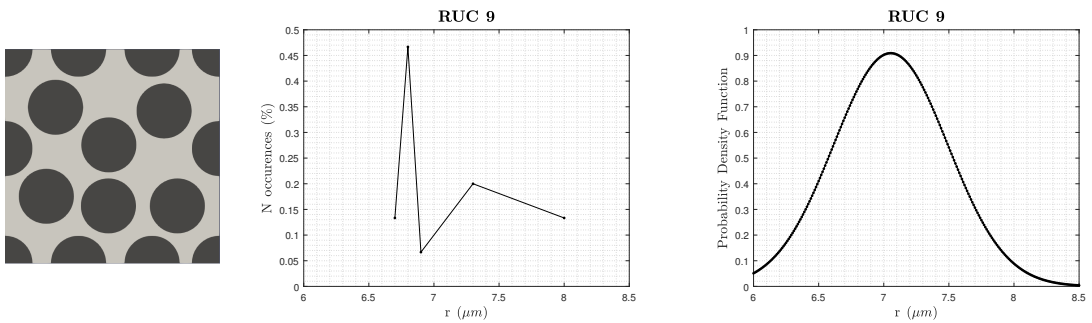


(a) RUC #8 (b) Nearest neighbor distance (c) Nearest neighbor Pdf

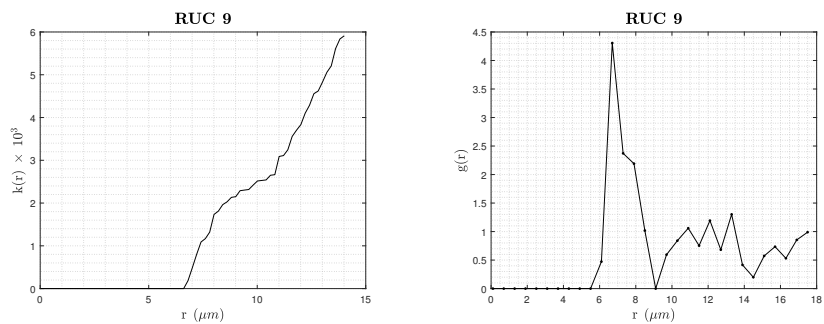


(d) Second-order intensity function (e) Radial distribution function

Figure A.18: Ten-fibers RUC #8 and relevant statistical descriptors



(a) RUC #9 (b) Nearest neighbor distance (c) Nearest neighbor Pdf



(d) Second-order intensity function (e) Radial distribution function

Figure A.19: Ten-fibers RUC #9 and relevant statistical descriptors

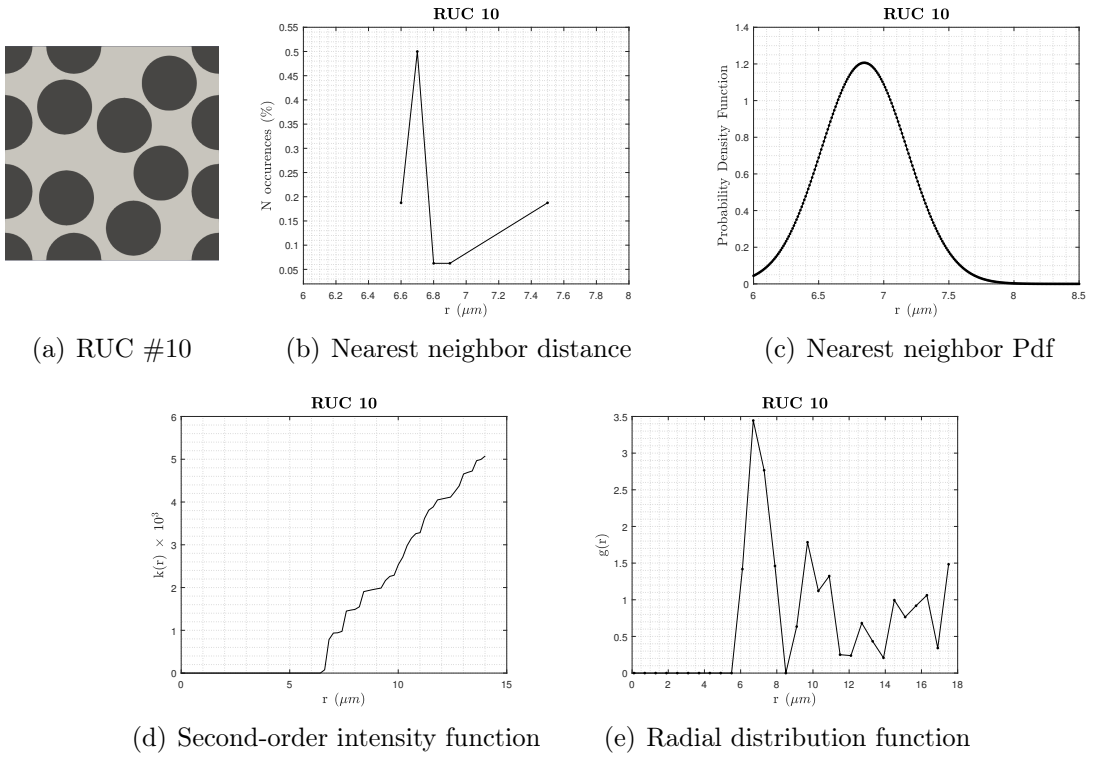


Figure A.20: Ten-fibers RUC #10 and relevant statistical descriptors

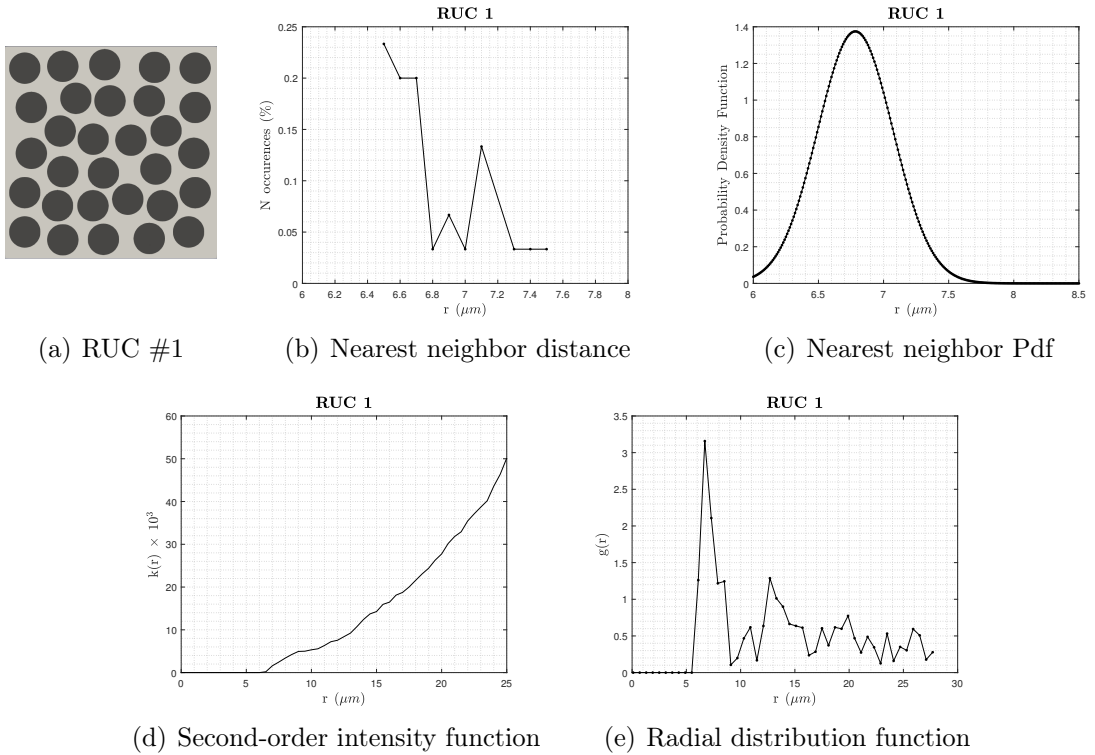


Figure A.21: Thirty-fibers RUC #1 and relevant statistical descriptors

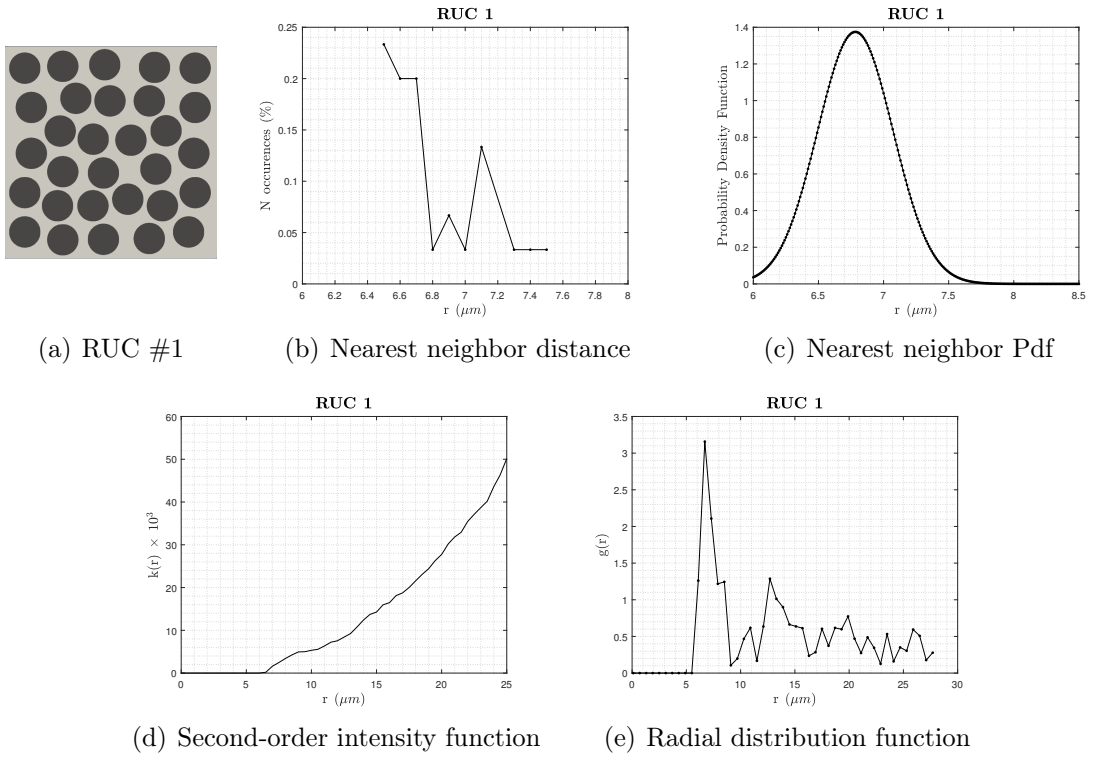


Figure A.22: Thirty-fibers RUC #1 and relevant statistical descriptors

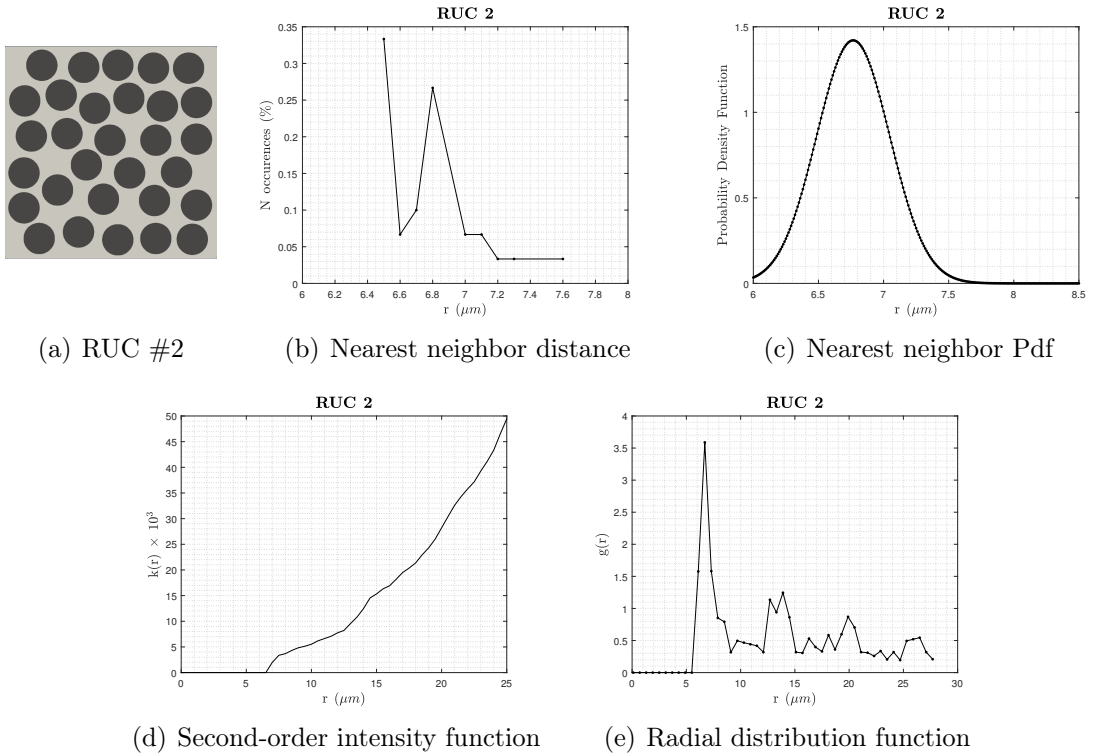


Figure A.23: Thirty-fibers RUC #2 and relevant statistical descriptors

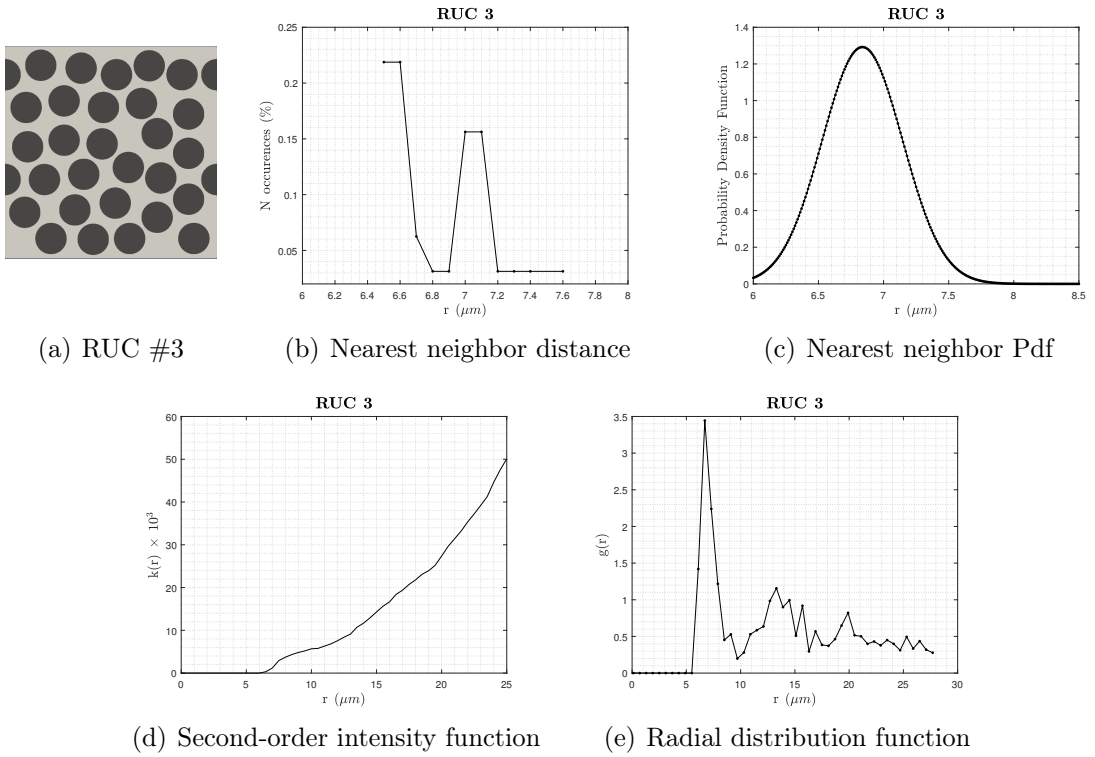


Figure A.24: Thirty-fibers RUC #3 and relevant statistical descriptors

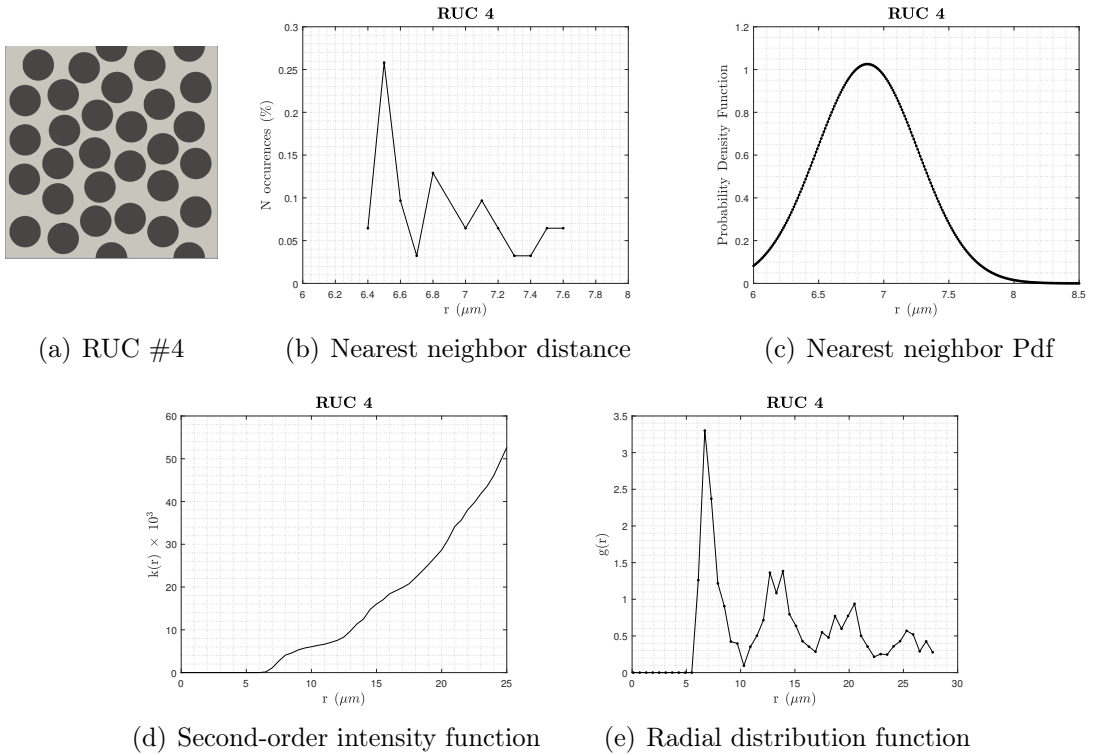


Figure A.25: Thirty-fibers RUC #4 and relevant statistical descriptors

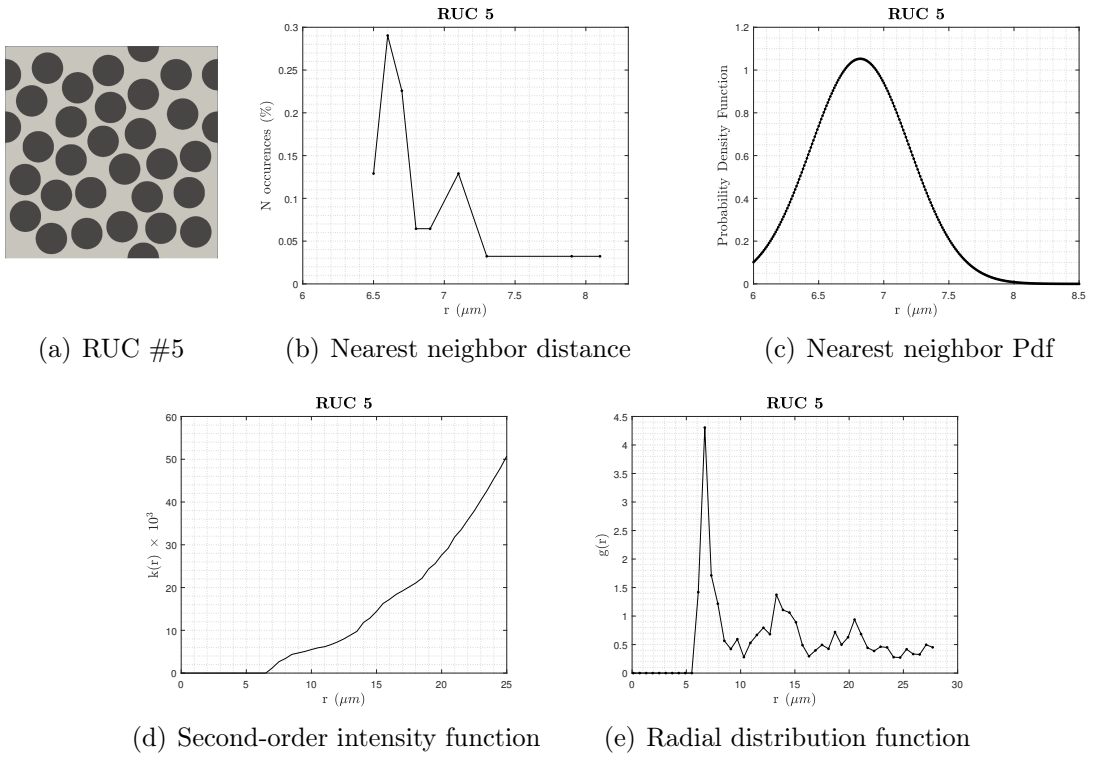


Figure A.26: Thirty-fibers RUC #5 and relevant statistical descriptors

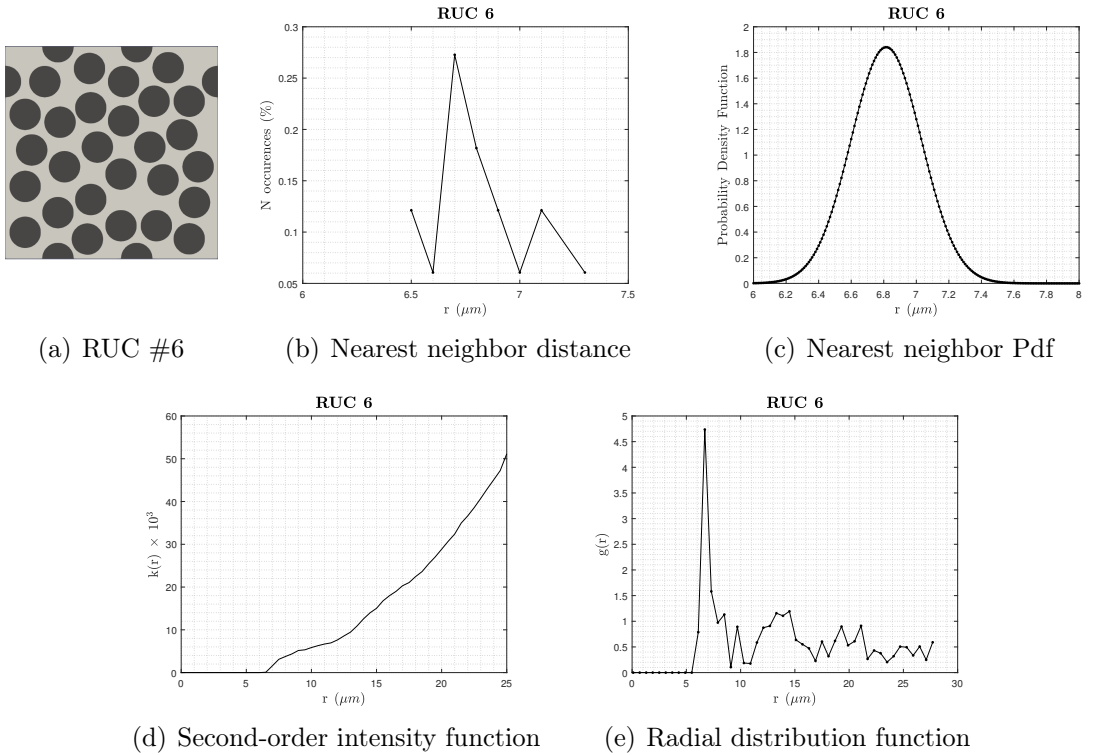


Figure A.27: Thirty-fibers RUC #6 and relevant statistical descriptors

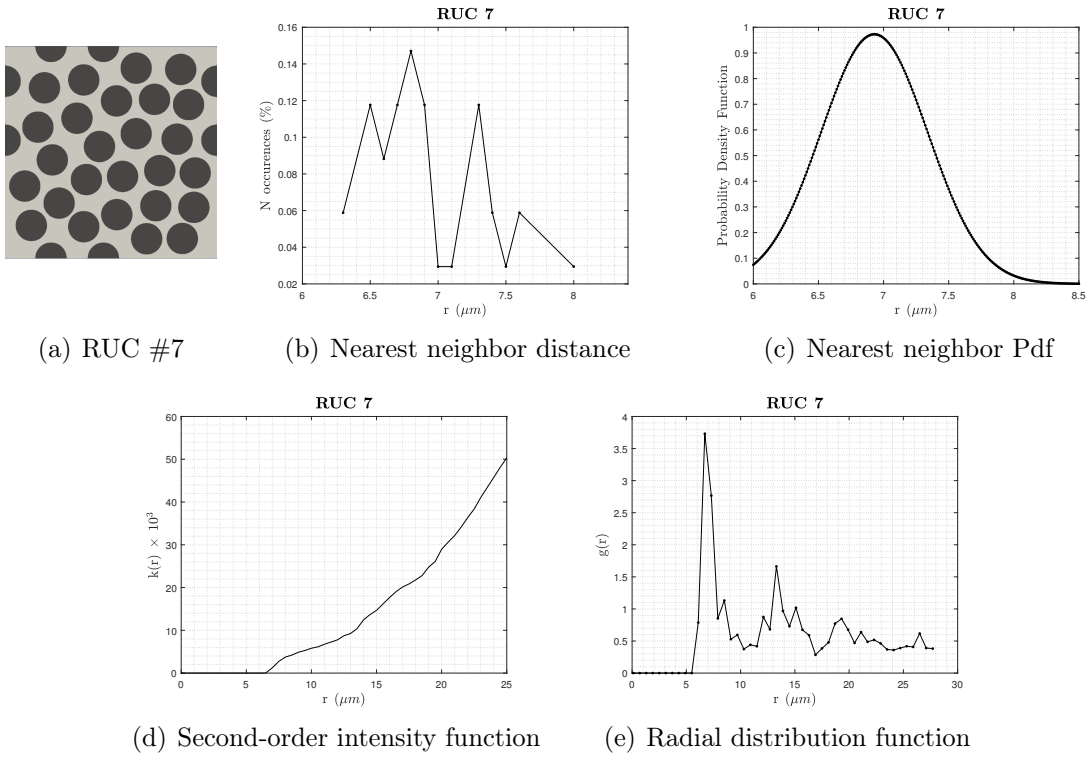


Figure A.28: Thirty-fibers RUC #7 and relevant statistical descriptors

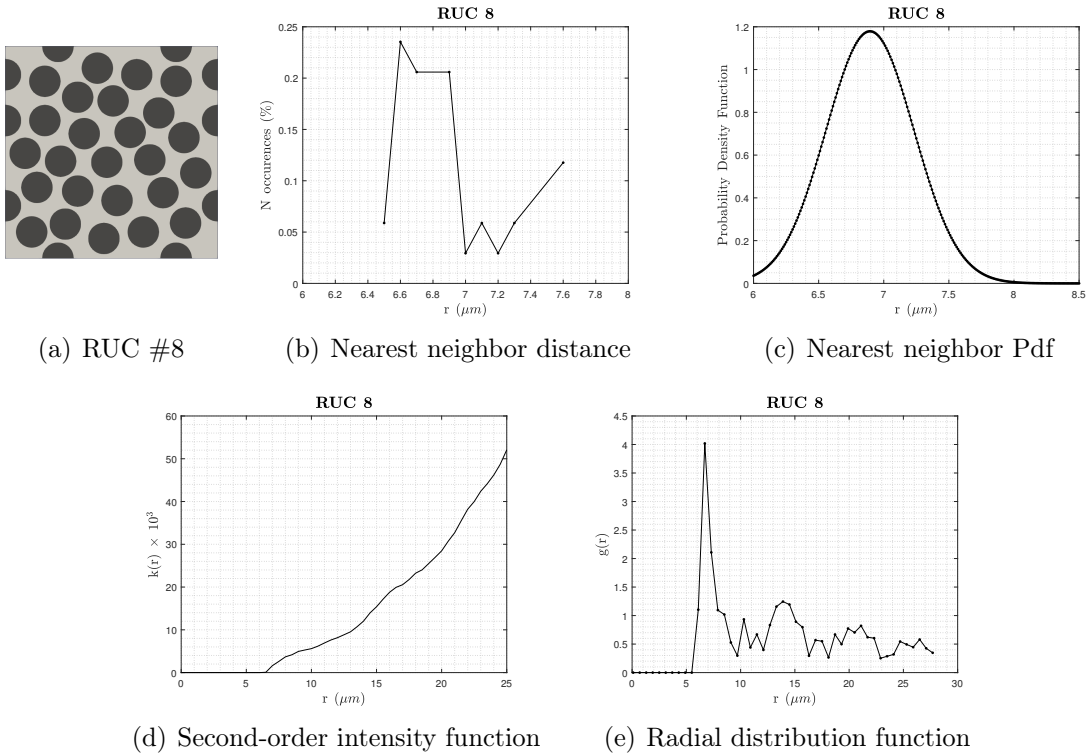


Figure A.29: Thirty-fibers RUC #8 and relevant statistical descriptors

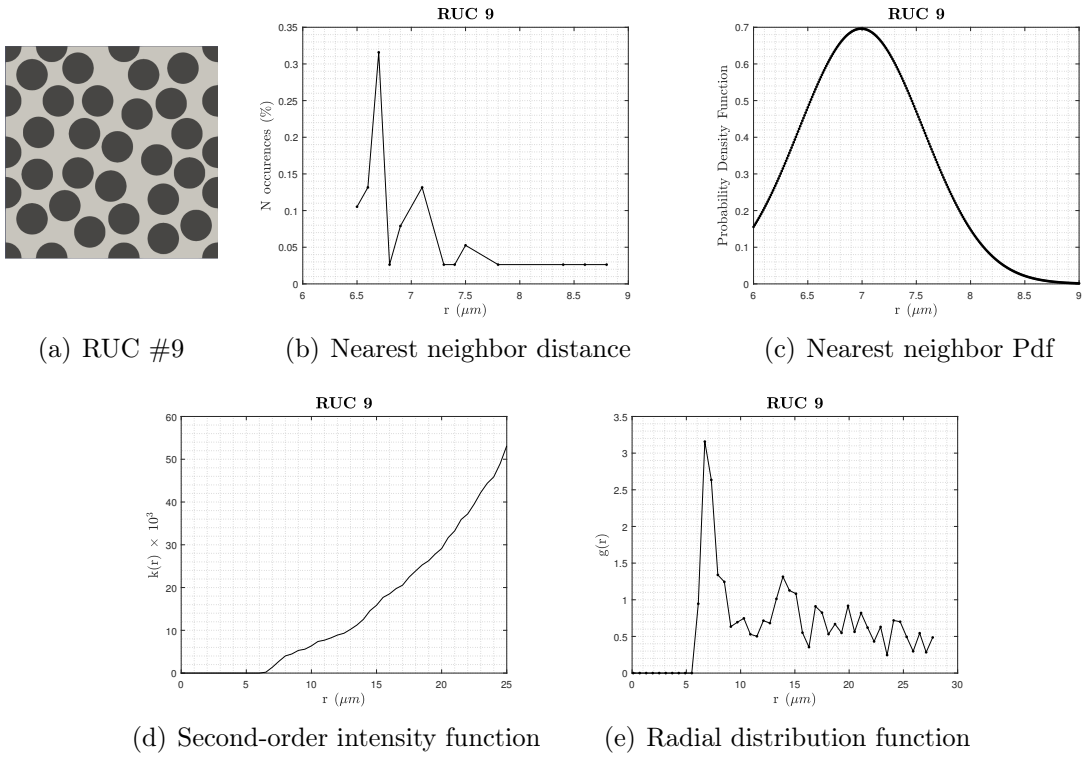


Figure A.30: Thirty-fibers RUC #9 and relevant statistical descriptors

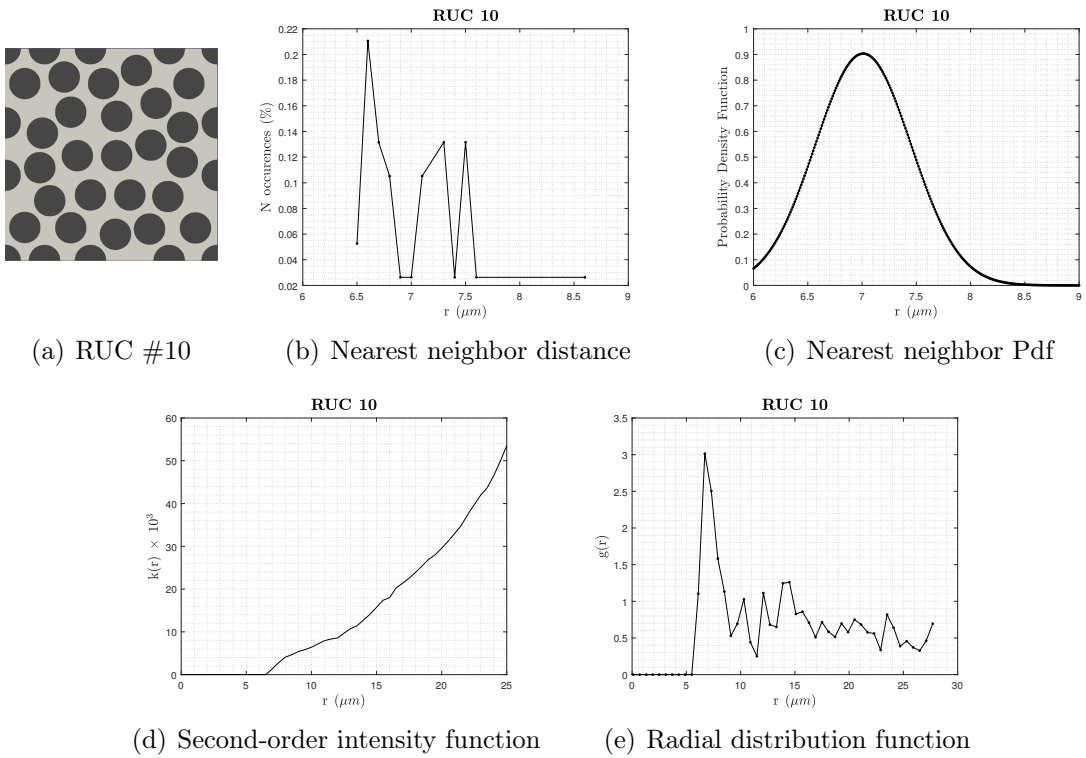


Figure A.31: Thirty-fibers RUC #10 and relevant statistical descriptors

Bibliography

- [1] S. Baragetti. *Introduzione ai Materiali Compositi*. Lecture Notes. Università degli Studi di Bergamo, 2015.
- [2] V.N. Bulsara, R. Talreja, and J. Qu. “Damage initiation under transverse loading of unidirectional composites with an arbitrarily distributed fibers”. In: *Composites Science and Technology* (1998).
- [3] E. Carrera, M. Maiarù, and M. Petrolo. “Component-wise analysis of laminated anisotropic composites”. In: *International Journal of Solids and Structures* 49 (2012).
- [4] E. Carrera, A. G. de Miguel, and A. Pagani. “Component-wise analysis of laminated structures by hierarchical refined models with mapping features and enhanced accuracy at layer to fiber- matrix scales”. In: *Mechanics of Advanced Materials and Structures* (2017).
- [5] E. Carrera and M. Petrolo. “Refined beam elements with only displacement variables and plate/shell capabilities”. In: *Meccanica* (2012).
- [6] E. Carrera et al. *Finite Element Analysis of Structures Through Unified Formulation*. 2014.
- [7] X. Chen and T.D. Papathanasiou. “Interface stress distributions in transversely loaded continuous fiber composites: parallel computation in multi-fiber RVEs using the boundary element method”. In: *Composites science and technology* (2003).
- [8] M Cinefra, E. Carrera, and P. Nali. “MITC technique extended to variable kinematic multilayered plate elements”. In: *Composite Structures* 92 (2010).

- [9] R.T. Dehoff and F.N. Rhines. *Quantitative Microscopy*. 1968.
- [10] R.B. Deo, J.H. Jr. Starnes, and R.C. Holzwarth. “Low-Cost Composite Materials and Structures for Aircraft Applications”. In: *RTO-MP-069(11)* (2003).
- [11] R.J. D’Mello, M. Maiarù, and A.M. Waas. “Virtual manufacturing of composites aerostructures”. In: *The Aeronautical Journal* (2016).
- [12] L. Euler. “De curvis elasticis”. In: *Methodus Inveniendi Lineas Curvas Maximi Minimive Proprietate Gaudentes, Sive Solutio Problematis Isoperimetrici Lattissimo Sensu Accept* (1744).
- [13] C. Gonzalez and J. Llorca. “Mechanical behavior of unidirectional fiber-reinforced polymers under transverse compression: Microscopic mechanism and modeling”. In: *Composites Science and Technology* (2007).
- [14] F. Grasso and C. Calabretta. *I materiali compositi nei mezzi di trasporto*. Lecture Notes. Università degli Studi di Catania, 2012.
- [15] M. Hojo et al. “Effect of fiber array irregularities on microscopic interfacial normal stress states of transversely loaded UD-CFRP from viewpoint of failure initiation”. In: *Composites Science and Technology* (2009).
- [16] D. Hull and T.W. Clyne. “An introduction to composite materials.” In: *Cambridge University Press* (1996).
- [17] E.M. Jensen, D.A. Leonhardt, and R.S. Fertig. “Effects of thickness and fiber volume fraction variations on strain field inhomogeneity”. In: *Composites Part A: Applied Science and Manufacturing* (2015).
- [18] I. Kaleel et al. “Computationally efficient, high-fidelity micromechanics framework using refined 1D models”. In: *Composites Structures* (2017).
- [19] K.C. Liu and A. Ghoshal. “Validity of random microstructures simulation in fiber-reinforced composite materials”. In: *Composites: Part B* (2014).
- [20] K.A. Malusare and R.S. Fertig. “Composite interaction energy and constituent average stresses for predicting composite failure”. In: *AIAA Journal* (2014).
- [21] P.D. Mangalgiri. “Composite materials for aerospace applications”. In: *Bulletin of Materials Science* (1999).

- [22] D.T. Mansilla. *Analysis and simulation of transverse random fracture of long fibre reinforced composites*. Ph.D. Thesis. Universitat de Girona, 2005.
- [23] P.R. Marur. “Estimation of effective elastic properties and interface stress concentrations in particulate composites by unit cell methods”. In: *Acta Materialia* (2004).
- [24] T. Matsuda et al. “Effects of fiber distribution on elastic-viscoplastic behavior of long fiber-reinforced laminates”. In: *International Journal of Mechanical Sciences* (2003).
- [25] A.G. de Miguel et al. “Micromechanics of periodically heterogeneous materials using higher-order beam theories and the mechanics of structure genome”. In: *Composite Structures* 180 (2017).
- [26] N.V. Nayak. “Composite Materials in Aerospace Applications”. In: *International Journal of Scientific and Research Publications* (2014).
- [27] G.P. Nikishkov. *Introduction to the Finite Element Method*. Lecture Notes. University of Aizu, 2004.
- [28] A. Pagani et al. “Analysis of laminated beams via Unified Formulation and Legendre polynomial expansions”. In: *Composite Structures* (2016).
- [29] M. Petrolo, E. Zappino, and E. Carrera. “Refined free vibration analysis of one-dimensional structures with compact and bridge-like cross-section”. In: *Thin-Walled Structures* 56 (2012).
- [30] S. Prashanth et al. “Fiber Reinforced Composites - A Review”. In: *Journal of Material Sciences & Engineering* (2017).
- [31] R. Pyrz. “Correlation of microstructure variability and local stress field in two-phase materials”. In: *Composites Science and Technology* (1993).
- [32] R. Pyrz. “Quantitative description of the microstructure of composites. Part I: morphology of unidirectional composite systems”. In: *Composites Science and Technology* (1993).
- [33] J.N. Reddy. “On locking-free shear deformable beam finite elements”. In: *Computer Methods in Applied Mechanics and Engineering* (1997).

- [34] B.D. Ripley. “The second-order analysis of stationary point processes”. In: *Journal of Applied Probability* (1976).
- [35] S.H.R. Sanei et al. “Characterization, synthetic generation, and statistical equivalence of composite microstructures”. In: *Journal of composite materials* (2016).
- [36] J. Sloan. *The fiber*. 2014. URL: <https://www.compositesworld.com/articles/the-fiber>.
- [37] D. Stoyan, W.S. Kendall, and J. Mecke. *Stochastic Geometry and its applications*. 1987.
- [38] A. Tewari and A.M. Gokhale. “Nearest neighbor distances in uniaxial fiber composites”. In: *Computation material science* (2004).
- [39] S.P. Timoshenko. “On the corrections for shear of the differential equation for transverse vibrations of prismatic bars”. In: *Philosophical Magazine* (1922).
- [40] G. Udupa, S. Shrinkantha Rao, and K.V. Gangadharan. “A review of Carbon Nanotube Reinforced Aluminium Composite and Functionally Graded composites as a Future material for Aerospace”. In: *Journal of Modern Engineering Research* (2014).
- [41] T.J. Vaughan and C.T. McCarthy. “A combined experimental-numerical approach for generating statistically equivalent fibre distributions for high strength laminated composite materials”. In: *Composites Science and Technology* (2009).
- [42] Z. Xia, Y. Zhang, and F. Ellyin. “A unified periodical boundary conditions for representative volume elements of composites and applications”. In: *International Journal of Solids and Structures* (2002).
- [43] Z. Xia et al. “On selection of repeated unit cell model and application of unified periodic boundary conditions in micro-mechanical analysis of composites”. In: *International Journal of Solids and Structures* (2006).
- [44] S. Yang, A. Tewari, and A.M. Gokhale. “Modeling of non-uniform spatial arrangement in a ceramic matrix composite”. In: *Acta Metallurgica* (1996).

- [45] J. Zeman and M. Šejnoha. “Numerical evaluation of effective elastic properties of graphite tow impregnated by polymer matrix”. In: *Journal of the Mechanics and Physics of Solid* (2000).